ORIENTATION INVARIANT CHARACTERISTICS OF DEFORMABLE BODIES IN MULTIBODY DYNAMICS

by

Adrijan-Petar Ribaric

A Dissertation Submitted to the Faculty of the

DEPARTMENT OF AEROSPACE AND MECHANICAL ENGINEERING

In Partial Fulfillment of the Requirements
For the Degree of

DOCTOR OF PHILOSOPHY
WITH MAJOR IN MECHANICAL ENGINEERING

In the Graduate College

THE UNIVERSITY OF ARIZONA

2012

ProQuest LLC.
789 East Eisenhower Parkway
P.O. Box 1346
Ann Arbor, MI 48106 - 1346

THE UNIVERSITY OF ARIZONA
GRADUATE COLLEGE

As members of the Dissertation Committee, we certify that we have read the dissertation

prepared by Adrijan-Petar Ribaric

entitled ORIENTATION INVARIANT CHARACTERISTICS OF DEFORMABLE BODIES IN MULTIBODY DYNAMICS

and recommend that it be accepted as fulfilling the dissertation requirement for the

Degree of Doctor of Philosophy

_____ Date:
Dr. Parviz E. Nikravesh

_____ Date:
Dr. Ara Arabyan

_____ Date:
Dr. Samy Missoum

_____ Date:
Dr. Robert Indik

_____ Date:
Dr. Seongho Kim

Final approval and acceptance of this dissertation is contingent upon the candidate's submission of the final copies of the dissertation to the Graduate College.

I hereby certify that I have read this dissertation prepared under my direction and recommend that it be accepted as fulfilling the dissertation requirement.

_____ Date:
Dissertation Director: Dr. Parviz E. Nikravesh

STATEMENT BY AUTHOR

This dissertation has been submitted in partial fulfillment of requirements for an advanced degree at the University of Arizona and is deposited in the University Library to be made available to borrowers under rules of the Library.

Brief quotations from this dissertation are allowable without special permission, provided that accurate acknowledgment of source is made. Requests for permission for extended quotation from or reproduction of this manuscript in whole or in part may be granted by the head of the major department or the Dean of the Graduate College when in his or her judgment the proposed use of the material is in the interests of scholarship. In all other instances, however, permission must be obtained from the author.

SIGNED: Adrijan-Petar Ribaric

ACKNOWLEDGEMENTS

This dissertation would not have been possible without the support of many people. I want to express my deepest gratitude to my Ph.D. advisor Dr. Parviz Nikravesh, who was abundantly helpful during my studies and offered invaluable assistance, strong support, and excellence guidance for this dissertation. I would also like to convey thanks to my friend Omid Kazemi, who helped me greatly with my research, and all other graduate friends from the Aerospace and Mechanical Engineering Department.

I wish to express my love and gratitude to my parents Petar and Marica Ribaric, as well as my siblings David, Larissa, and Matthias. They made me the person I am today. Finally, I want to express my gratitude to Natasa Vojvodic, who supported me and stood by me through my Ph.D. studies. I would like to thank her family as well, who accepted me completely as one of their own.

DEDICATION

To my family, who will always be close to my heart, wherever life takes me.

TABLE OF CONTENTS

TABLE OF CONTENTS - continued

TABLE OF CONTENTS - continued

LIST OF FIGURES

LIST OF FIGURES - continued

LIST OF TABLES

ABSTRACT

In multibody systems, mechanical components (bodies) can be assumed rigid (non-deformable), if their deformation is negligible. For components with non-negligible deformations several methods were developed to represent their deformation. The most widely used method is the floating frame of reference. In this formulation the deformable body is represented by a finite element model whose deformation is described with respect to a local body-fixed frame. Unfortunately, finite element models can include many degrees-of-freedom, which stand in contradiction to the requirements of multibody dynamics. System truncation is therefore inevitable to support computational efficiency.

The use of modal data in representing a deformable body is well understood in the multibody community. By truncating modes associated with higher frequencies, the total degrees-of-freedom of the deformable body can be reduced while preserving its dynamic eigen-properties. However, since the finite element model may be in contact with other moving bodies, the reduction technique needs to address the issue of moving boundary conditions. The component mode synthesis reduction methods are such techniques that describe the deflection of all the nodes as a superposition of different types of modes. However, it is limited in the fact that the nodes in contact need to remain in contact throughout a simulation. In some applications these nodes may change, i.e. a node that is in contact with another body or the ground at one instant may become free at the next instant. The present methodologies in multibody modeling of a deformable body with modal data have not yet addressed the issue of changing contact nodes.

This research highlights the usefulness of orientation invariant characteristics of some deformable bodies. It proposes to define orientation invariant degrees-of-freedom of the reduced model in Eulerian space, while the remaining degrees-of-freedom are defined in Lagrangian space. In some circumstances, this approach can resolve the issue of changing contact nodes. The combination of Eulerian and Lagrangian formulation for component mode synthesis reduced finite element models is a new concept in deformable multibody dynamics.

1. INTRODUCTION

In today's society, technology is a major part of our daily life. From home appliances to public transportation, our dependency on technological comforts is evident. In order to increase this comfort, the design process for product development is constantly evolving. Several decades ago, the industry started utilizing computers to expedite the design process and reduce development costs. Today's computer-aided analysis tools allow the engineer to create simulation models of any physical system. In mechanical engineering, a simulation model is usually an abstract model of a physical product that can mimic realistic behavior such as static deformation or dynamic motion. The simulation model can be used instead of the prototype to test a product for its behavior or study the effects of changes in material properties or geometric dimensions. In some cases, such as space technology, testing is possible solely with simulation models.

In order to create a simulation model, the engineer must know the individual components of the product. The nature of these components can be mechanical, electrical, hydraulic, etc. If the mechanical components of the product, also referred to as bodies, are allowed to move relative to one another, the product is called a multibody system (MBS) [77]. Many applications can be defined as a MBS: mechanisms, automobiles (steering systems, suspension, etc.), robots, trains, industrial machinery, space structures, satellites, the human body, and others. If the bodies of the MBS move in parallel planes, then we refer to it as planar MBS [77]. An example of a planar (two-

dimensional) MBS is the four-bar or the slider-crank mechanism. If the bodies of a system do not move in parallel planes, then we call it a spatial MBS. Examples of more advanced spatial (three-dimensional) MBS include the suspension and steering systems of an automobile, the multi degree-of-freedom robot arm of the space shuttle, or the landing gear system of an airplane.

In most MBS, the bodies are connected to each other through a set of kinematic joints and force elements. A joint connects two bodies together with the possibility of relative movement between them. This imperfect joining of two bodies permits certain relative motion, and prevents or restricts others. In planar MBS, the most used joints are pin (revolute), slider (prismatic), and gears, which allow one relative motion between the joined bodies [14]. In spatial MBS, cylindrical, spherical, universal, and helical joints are used as well. Other joints such as cam-follower (track-wheel rolling contact) are also sometimes used. Force elements are usually springs, dampers, or actuators. These elements exert forces onto the bodies to which they are connected, but do not restrict them in their motion.

In the traditional multibody dynamics (MBD), bodies were considered to be rigid (non-deformable), while the dynamics of a very simple rigid MBS, such as a pendulum, used to be solved graphically or analytically. However, MBD is a generalized mathematical method that does not make any assumptions on the overall motion of the system; e.g., it does not restrict the rotations to small angles. Because of large rotations non-linearity is a common feature in MBD. Even with the rigid-body assumption, equations of motion for larger systems can only be solved numerically. Therefore, real

interest in analyzing MBS did not start until 1965 [12], which is the same time that computational techniques found their way into the field of mechanical engineering, and computer-aided formalism for the analysis of MBS started to be employed [13]. About two decades ago, MBS received popular attention similar to that produced by the finite element method in the early nineteen-seventies for structural design [14].

Nowadays, many software packages exist that simulate MBS. These programs can be grouped into special- or general-purpose programs. A special-purpose program is coded for a specific MBS, such as a four-bar mechanism. The user can only modify a few parameters of the system, such as the mass and dimensions of the bodies. The equations of motion of the MBS are derived a priori and coded into the special-purposes program. The numerical solver of the program can then be fine-tuned to this specific MBS, which increases the computational efficiency. However, this program cannot be used for other MBS. In order to spare the engineer derivation and coding for each new MBS, general-purpose programs have been developed, such as SIMPACK, MSC ADAMS, Dassault's Dymola, etc. They require detailed information about the system under consideration, such as number of bodies, their masses and moments of inertia, and the kinematic joints and force elements between the bodies. Equations of motion are then generated by the program and solved numerically. While a general-purpose program provides great flexibility, it may not be as computational efficient as a special-purpose program.

In addition to the differentiation between special- and general-purpose codes, many MBS programs differ in their approach to describe the position, velocity, and

acceleration of a MBS. In general, there are two choices. The first choice is a system with *independent* coordinates, sometimes also referred to as *generalized* coordinates. Here, the number of coordinates coincides with the number of degrees-of-freedom of the system. This will lead by definition to a set of minimal coordinates; i.e., there cannot be any fewer coordinates in order to fully describe the system. From a computational standpoint the minimal set is the most efficient and the least sensitive to numerical errors and is therefore favored for special-purpose programs. However, the order of non-linearity and complexity of the governing equations of motion is high, which makes them less useful for general-purpose programs. The second choice is an expanded system of *dependent* coordinates, such as *relative* coordinates, *natural* or *fully Cartesian* coordinates, *reference point* or *Cartesian* coordinates. A good explanation of each set of coordinates can be found in [2, 12, 13, 14]. In the case of dependent coordinates the number of coordinates is larger than the number of degrees-of-freedom of the system. With such coordinates the system can be described much more easily, but the governing equations of motion are interrelated through so-called *constraint* equations. The number of constraints is the difference between the number of coordinates and the number of the system's degrees-of-freedom (DoF). Furthermore, constraint equations are generally non-linear. Dependent coordinates are better suited for a general-purpose program, but are computationally less efficient and more exposed to numerical errors [13]. While the issue of computational efficiency between generalized and dependent coordinates was of major concern several years ago, the computational difference became almost unimportant today thanks to the ever-increasing power of computers. Modern computers

can simulate a rigid MBS with less than hundred dependent coordinates almost in real-time.

In the past, most MBS were approximated with the rigid-body assumption. However, with the increase of operating precision and the usage of light weight materials in industrial and technological systems, the demand for considering deformation effects of system components became inevitable. These deformation effects can vary from misalignments in spinning bearings to stress peaks in meshing gears and can lead to premature failure of system components. For that reason deformable MBD evolved as a new research field in the early nineteen-seventies [1] with the basic principle that the rigid-body assumption is no longer valid for some of the bodies in a system. MBS started to be split into two sets of bodies: bulky compact solids that can be modeled as rigid, and relatively elastic bodies, such as rods, beams, plates, and shells, that may deform. An example of such a system is an automobile suspension system, as shown in Figure 1-1. While the quarter chassis and the hub can be considered to be rigid, the rods, that connect the hub to the chassis, are relatively thin and might have to be modeled as deformable. Simulating a full vehicle driving scenario over rough surface with rigid or deformable suspension rods can provide significantly different results for the handling and ride comfort of a car. Subsequent design improvements would be difficult, if the underlying vehicle model does not approximate the physical vehicle correctly.

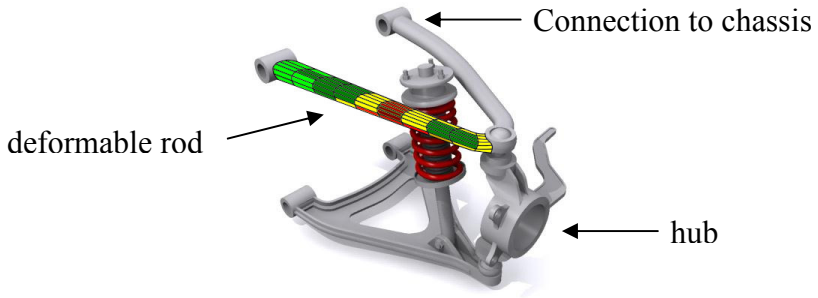

Figure 1-1: Double wishbone suspension system [73].

Many approaches have been taken by researchers to include deformable bodies into a MBS. Some approaches consider the deformable body as a collection of rigid-bodies that are interconnected through kinematic joints and spring-damper elements. Other approaches describe the body as a linear combination of rigid-body modes and some sort of deformation mode shapes, which, for example, can be derived from the Rayleigh-Ritz method [79]. Today, the most common approach to represent deformable bodies is through finite element (FE) models. The finite element method (FEM) is a well established numerical technique in the engineering field for finding approximate solutions to partial differential equations as well as integral equations. It originated from the need to solve complex structural analysis problems in civil and aeronautical engineering. The technique is based on the discretization of a continuous domain into a set of discrete sub-domains, also called elements [78]. All elements together build a mesh with nodes. The nodes represent connections between adjacent elements. In mechanics, the deformation of a body is then represented by the deflection of all the nodes. If the deformation of a structure is small, then the underlying static equations can be linearized for structural analysis and solved efficiently. However, in MBD a

deformable body usually undergoes large rigid body displacements. The dynamic equations are highly nonlinear and exhibit a strong nonlinear coupling between different modes of displacements. These equations can be numerically integrated using standard techniques such as Euler's method or Runge-Kutta.

The combination of FE models and large rotation can cause difficulties in some situations. The displacement field of some finite elements (isoparametric type), such as rectangular, triangular, solid, and tetrahedral elements, can be used to describe an arbitrary displacement, since, in general, these elements use only nodal displacements as coordinates and do not employ rotations or slopes. As such, these elements can be used in the large rotation and deformation analysis of flexible bodies. However, the displacement field of some other elements (non-isoparametric type), such as beam, plate, and shell elements, cannot be used to describe large rotation and deformations. These elements are based on nodal displacement and infinitesimal nodal rotation, which leads to a linearization of the kinematic equations of the elements. Non-isoparametric elements do not produce zero strain under an arbitrary rigid body displacement. A more detailed description about the difference between isoparametric and non-isoparametric elements can be found in [1]. In order to solve the problems of large rotation associated with these elements, several methods have been proposed in MBD. These methods are categorized into four different formulations: *floating frame of reference*, *incremental*, *large rotation vector*, and *absolute nodal coordinate* [2].

The *floating frame of reference formulation* is currently the most widely used method in the computer simulation of deformable multibody systems. It is implemented

in several commercial programs for deformable MBS. In this approach a reference frame (body frame) is assigned to each deformable body. The large translation and rotation of the body are described by the position and orientation of the body frame with respect to an inertial frame. The deformation of the body itself is expressed by nodal coordinates of the elements and measured with respect to the body frame [3]. However, this formulation is only valid if the deformation of the body is small. The *incremental* finite element approach tries to minimize the error that is caused by non-isoparametric type elements by representing a large rotation as a sequence of small rotations. This approach has been widely used in the computational mechanics community for structural analysis with large deformations [10] and is implemented in numerous general-purpose FE computer programs. However, it can be shown that the use of this method does not lead to an exact modeling of rigid-body inertia for a body in an undeformed state [1]. Furthermore, non-isoparametric elements used in the incremental methods do not lead to zero strain under an arbitrary rigid-body displacement. In the *large rotation vector formulation* the element nodal coordinates consist of displacements and finite rotations and are defined with respect to the global coordinate system. Furthermore, the rotation of the element cross-section is approximated using interpolating polynomials. The problem with this method is that finite rotation coordinates need to be interpolated. Also, this formulation leads to redundancy in describing the large rotation of the cross-section [2]. A more recent developed formulation is the *absolute nodal coordinate formulation* [2, 18, 19]. In this approach no infinitesimal or finite rotations are used as the nodal coordinates, unlike in the previous three formulations. Instead, absolute slopes and displacements at the

nodal points are used as the element nodal coordinates. The requirement for this formulation is only a consistent mass approach. The absolute nodal coordinate formulation differs from the classical FE formulations in the sense that not all of the nodal coordinates have a physical meaning. Also, unlike the floating frame of reference formulation, this formulation uses only absolute coordinates to define displacements and slopes.

Besides the problem of large rotations, FE models also introduce a second problem in MBD due to its large number of degrees-of-freedom. Without question, a direct correlation exists between the number of DoF of FE models and the required computation time. Some deformable bodies might be represented through a small number of finite elements (less than 100), such as a simple straight uniform rod or a flat uniform plate. However, most FE models are of more complex structures, such as the crankshaft of an engine, the gears of a transmission, or the housing of a gearbox. These bodies can include hundreds of finite elements, and in some cases may exceeds even 10^5 elements, such as a FE tire model. Although high-resolution FE models serve a valuable purpose in the design phase, or in understanding certain characteristics of behavior, they are not suitable for MBS purposes [81]. The reason is that due to the large number of DoF of such models, the computation time for a MBD simulation can become impractical, even on large high performance computers. Therefore, these FE models need to be reduced in the number of DoF by some kind of reduction technique.

In the last few decades several reduction techniques have been introduced in the literature. One of the simplest reduction techniques is *Guyan condensation* [4], also

known as static condensation. In this technique the number of nodes (degrees-of-freedom) of a FE model are reduced in such a way that the static properties of the model is preserved. However, this technique alters the eigen-properties of the model, which makes it useless in a transient analysis. *Modal truncation* is another well-known reduction technique. Here, the FE model is transformed from nodal to modal space. By truncating the higher modes, the DoF of the FE model can be significantly reduced. This technique provides acceptable results in a structural analysis due to the presence of fixed boundary conditions. However, if a deformable body is integrated into a MBS, most likely it will have contact with other rigid or flexible bodies, through either a joint connection or a force element. These contact points, which represent the new boundaries of the FE model, will inevitably move with the other bodies. The standard modal reduction is inadequate for moving boundary conditions. Methods known as *component mode synthesis* (CMS) address the issue of moving boundary conditions [5-8]. The main idea behind these methods is the superposition of different types of modes. One method suggests describing the deflection of all the nodes as a function of the deflection of the contact nodes and the constrained modes. It is mostly referred to as the Craig-Bampton reduction and was originally suggested for sub-structuring of large structures [7] in the classical FE method.

Most reduced FE models suitable for MBD transform the equations of motion to modal coordinates employing the Craig-Bampton reduction technique. The use of modal data in representing a deformable body is well understood in the multibody community as long as the so-called contact nodes remain as contact nodes throughout the entire period

of simulation; i.e., joint connection or force element remain unchanged to a point on the body. However, this is not the case for all MBS. In some applications the contact nodes may change; i.e., a node that is in contact with another body or the ground at one instant may become free at the next instant (or after several time steps). An example of such an application is a rotating power transmission belt, as shown in Figure 1-2 (a). In this MBS the pulleys can be considered as rigid bodies and the belt as a flexible body. The belt is represented by a FE model whose contact nodes are initially attached to the pulley. As soon as the belt rotates, the contact nodes will leave the pulley. New nodes that are about to become in contact with the pulleys need to be declared as contact nodes. This leads to a change in the boundary conditions for the deformable body. Another example is the rolling tire, as shown in Figure 1-2 (b). In any tire-ground contact scenario, some of the nodes would be in contact with the ground. A soon as the tire rolls, some nodes from the contact patch leave the ground and some other nodes enter the contact area. Contact nodes change during the entire simulation. Further examples that include changing contact nodes are the drum in a printing machine, a belt conveyor, or the chain-drive on a tank. In all these applications the deformable body cannot be truncated, since the present methodologies in multibody modeling of a deformable body with modal data have not yet addressed the issue of changing contact nodes. The main focus of this dissertation is to compensate these drawbacks by extending present methodologies with new and innovative features.

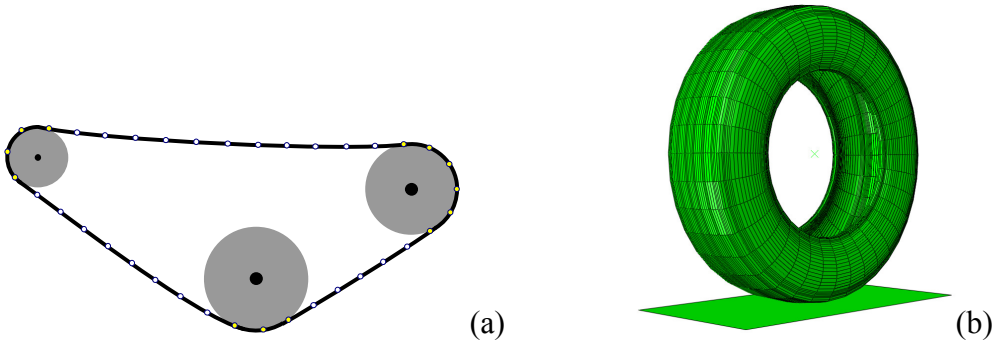

Figure 1-2: (a) Power transmission belt with contact nodes (yellow); (b) Finite element tire with contact nodes at the patch.

During the research phase of this dissertation, certain applications were found that included deformable bodies with specific orientation invariant characteristics. Two significant applications that include such a body are the power transmission belt and the rolling tire. The definition of the orientation invariant characteristic and its implication on changing contact nodes can be best explained using the example of a rolling tire. Consider a still standing tire on a road that is not numerically discretized, as shown Figure 1-3 (a). This tire has a particular continuous mass and stiffness distribution that is symmetric about the vertical axis. If the tire is now rolled over the ground, for instance for an angle of 45 degrees, then the symmetry of the mass and stiffness distribution about the vertical axis has not changed for an outside observer; i.e., the stiffness and mass is independent of the roll about the wheel axis. Discretizing the tire with finite elements before the rotation or after the rotation with the same mesh orientation will lead to the same mass and stiffness matrix, as shown in Figure 1-3 (b). This suggests that the FE mesh can become independent of the roll about the wheel axis. For a rolling tire, the FE mesh translates with the tire but does not need to roll with it. The roll can be represented

by a flow of mass points through the nodes of the mesh. A similar concept is known in the FE community as the Arbitrary-Lagrangian-Eulerian (ALE) approach.

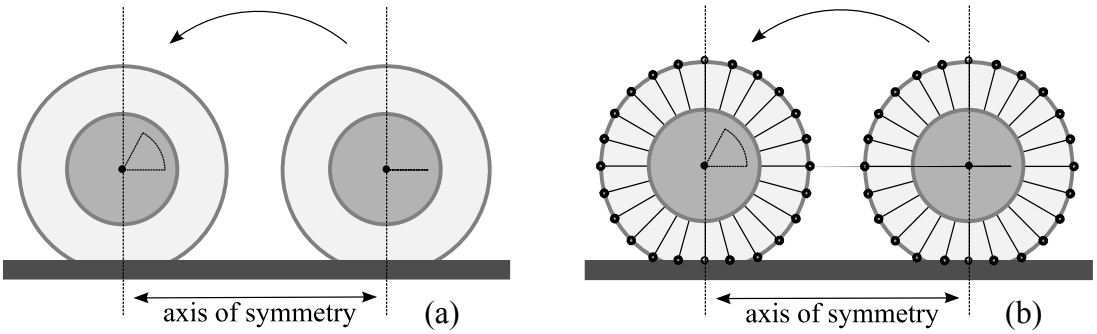

Figure 1-3: Representation of symmetry in a rolling tire.

The concept of flowing mass points applies also to a power transmission belt on an engine block, as shown in Figure 1-4. Here, it becomes unnecessary to track the travel of the belt along the pulleys. From the perspective of the engine, the mass and stiffness distribution of the traveling belt never changes. The resulting advantage of a non-rotating mesh is a fixed set of contact nodes that does not change during a simulation. On the other hand, the deflection of free nodes (nodes that never contact the ground or other bodies) can be expressed using modal data. Then, using the Craig-Bampton reduction technique, the total number of DoF of the system can be reduced by eliminating modes that do not contribute significantly to the overall dynamics of the system.

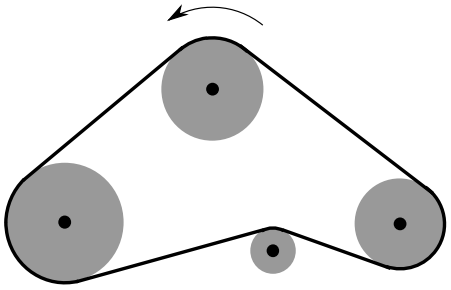

Figure 1-4: Traveling belt on an engine block.

1.1 Objective

This dissertation focuses on deformable bodies that include many degrees-of-freedom and hence, require modal truncation to conform to the requirements of multibody simulation, but at the same time have changing contact notes. While a general solution for all deformable bodies with changing contact nodes does not exist, some of these bodies reveal an orientation invariant characteristic. This characteristic shows that the mass and stiffness distribution is independent of a specific rotation. In this work a new methodology is introduced that allows the mesh of the FE model to be decoupled from that specific rotation by describing some degrees-of-freedom in Eulerian space while the remaining DoF are expressed in Lagrangian space. The new concept is referred to as the *flowing material*. In the following chapters the reader is presented with a clear picture of the essential ideas behind the new concept, such as what it requires, and how it can be implemented in a deformable MBS. The concept is first introduced on a simple moving string model with fixed boundaries whose equations of motion are well known. Then the concept is extended to a moving string model with varying boundary conditions. After that, the same concept is applied to a power transmission belt/chain and a

pneumatic tire. Here, simulations are provided to present the new methodology in real applications and to serve as a validation for the equations that are derived in this work.

1.2 Organization of the dissertation

The dissertation is separated into nine chapters, starting with the first chapter, the introduction. The second chapter covers several topics that are important for the reader to know in order to follow the concepts and derivation in the following chapters. The topics start with the dynamics of a rigid body, followed by the dynamics of a system of unconstrained and constrained rigid bodies, and then focus on the dynamics for a flexible body including reference conditions. The third chapter introduces a truncation concept for the reduction of a flexible body. The essential new contribution of this work starts from chapter four, where a non-translating string with fixed and varying boundaries is introduced. Also, in this chapter the string model is extended with the idea of *flowing material* that introduces translational motion. Here, a numerical and analytical approach is derived and compared in order to establish the validity of the new concept. The fifth chapter extends the same methodology to a power transmission belt and chain. The derivations of the equations of motion for the belt/chain are first performed in nodal coordinates, and then extended to modal form where the concept of *flowing material* is included. A validation of the new power transmission belt model is given in chapter six. A rolling tire is another application where the new concept can be applied. Chapter seven derives the formulation of a pneumatic tire in detail, where both the nodal and modal forms are presented. Chapter eight presents a detailed validation of the new tire model.

An extended discussion about the results is included well. Chapter nine summarizes and concludes the work. Mode shape derivatives are an essential part of the *flowing material* concept. Appendix A discusses their properties and offers a few suggestions on how to obtain them. Appendix B compares the difference between the Lagrangian and Eulerian formulation, which might help the reader to understand the *flowing material* concept more clearly.

1.3 Nomenclature

This work adopts the matrix notation that is used in [3]. This notation keeps the attention on concepts without losing sight of details. The reader should find the notation very effective in multibody formulations, especially when deformable bodies are involved. The following nomenclature is used:

Reference frames:

x-y-z	Inertial
$\xi - \eta - \zeta$	Body attached

Vectors and arrays:

$\mathbf{r}$, $\boldsymbol{\delta}$	Bold-face, lower-case characters

Matrices:

$\mathbf{M}$, $\boldsymbol{\Lambda}$	Bold-face, upper-case characters

Slashed (line-through) characters:

$\not{\mathbf{r}}$, $\not{\boldsymbol{\delta}}$	A vector or matrix described in body-fixed frame

Over-scores:

~	(tilde)	Transforms a 3-vector to a skew-symmetric matrix
^	(hat)	Stacks vertically 3-vectors or 3×3 skew-symmetric matrices
–	(bar)	Repeats a 3×3 matrix to form a block-diagonal matrix

The following examples should clarify the notation. Assume that $\mathbf{b}^i$ is a 3-vector and $\tilde{\mathbf{b}}^i$ is a 3×3 skew-symmetric matrix for i =1, ..., n. Let $\mathbf{I}$ be a 3×3 identity matrix and $\mathbf{A}$ be a 3×3 rotation matrix. Then the following stacked arrays and matrices can be constructed:

$$\mathbf{b}=\begin{Bmatrix}\mathbf{b}^1\\ \vdots\\ \mathbf{b}^n\end{Bmatrix},\quad \hat{\tilde{\mathbf{b}}}=\begin{bmatrix}\tilde{\mathbf{b}}^1\\ \vdots\\ \tilde{\mathbf{b}}^n\end{bmatrix},\quad \hat{\mathbf{I}}=\begin{bmatrix}\mathbf{I}\\ \vdots\\ \mathbf{I}\end{bmatrix},\quad \bar{\mathbf{I}}=\begin{bmatrix}\mathbf{I} & \cdots & \mathbf{0}\\ \vdots & \ddots & \vdots\\ \mathbf{0} & \cdots & \mathbf{I}\end{bmatrix},\quad \bar{\mathbf{A}}=\begin{bmatrix}\mathbf{A} & \cdots & \mathbf{0}\\ \vdots & \ddots & \vdots\\ \mathbf{0} & \cdots & \mathbf{A}\end{bmatrix}$$

2. DYNAMICS OF RIGID-DEFORMABLE MULTIBODY SYSTEMS

This chapter introduces to the reader the governing equations of motion for multibody systems containing rigid and deformable bodies. The chapter begins with rigid bodies and then continues to deformable bodies. Many ideas and formulations throughout this dissertation are based on the content of this chapter. It is assumed that the reader is familiar with the basic concepts of the finite element method, as found in [78].

2.1 Rigid body dynamics

The kinematics of a rigid body is determined by its position, velocity, and acceleration. There are several ways to describe these kinematic identities. In this dissertation, the reference point coordinates will be used, since they describe the position and orientation of the body directly and are the most adequate set of coordinates for a general-purpose program. In this section the governing equations of motion of a rigid body are derived using reference point coordinates. Then, the process is extended to systems of unconstrained and constrained rigid bodies.

2.1.1 Position and orientation of a rigid body

Consider a rigid body in space that has a body-fixed $\xi\eta\varsigma$ reference frame attached to it at its center of mass or centroid. The position of this body with respect to an inertial *xyz* global frame can be represented by vector $\mathbf{r}$. The orientation of the body with respect to the inertial frame can be defined by means of the orientation of the

$\xi\eta\varsigma$ body-fixed frame with respect to the inertial frame. If $\mathbf{s}'^{P}$ is a vector on the body expressed in the body-fixed frame, then it can be expressed in the inertial frame by transforming it with the rotation matrix **A**; i.e.,

$$\mathbf{s}^{P} = \mathbf{A}\mathbf{s}'^{P} \tag{2.1}$$

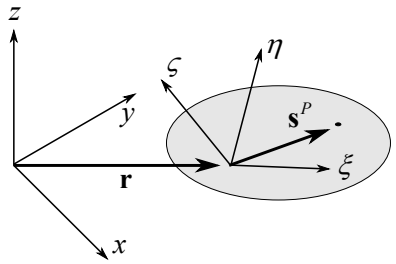

Figure 2-1: Position and orientation of a body.

2.1.2 Forces and moments

To describe the dynamics of a body, it is convenient to replace the forces that act on the body by an equivalent system of one force and one moment, as shown in Figure 2-2. The force **f** acts at the center of mass of the body and is equal to the sum of all *k* forces acting on the body; i.e.,

$$\mathbf{f} = \sum_{i=1}^{k} \mathbf{f}_i \tag{2.2}$$

The moment is the sum of all applied torques and the moments of all individual forces with respect to the centroid; i.e.,

$$\mathbf{n} = \sum_{i=1}^{m} \mathbf{n}_i + \sum_{i=1}^{k} \tilde{\mathbf{s}}_i \mathbf{f}_i \tag{2.3}$$

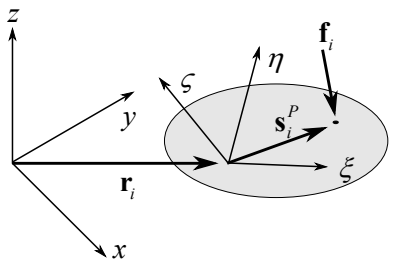

Figure 2-2: Applied forces.

2.1.3 Equations of motion of a rigid body

Consider body *i* in a multibody system that is not linked to any other bodies except through force elements, such as springs, dampers, actuator, etc. If the sum of all forces that act on this body is denoted by $\mathbf{f}_i$, and the sum of the moments of all the forces and any pure moment is denoted by $\mathbf{n}_i$, then the translational and rotational equations of motion for this body is given as

$$\begin{aligned} m_i\ddot{\mathbf{r}}_i &= \mathbf{f}_i \\ \mathbf{J}_i\dot{\boldsymbol{\omega}}_i + \tilde{\boldsymbol{\omega}}_i\mathbf{J}_i\boldsymbol{\omega}_i &= \mathbf{n}_i \end{aligned} \tag{2.4}$$

where m_i is the total mass of the body and $\mathbf{J}_i$ is the global inertial tensor. The translational acceleration of the body is denoted by $\ddot{\mathbf{r}}_i$ and the angular velocity and acceleration about the inertial *xyz* axes are $\boldsymbol{\omega}_i$ and $\dot{\boldsymbol{\omega}}_i$, respectively. Equation (2.4) is referred to as the Newton-Euler equations for an unconstrained body and is expressed in the inertial frame. Here, the inertial tensor $\mathbf{J}_i$ changes with the orientation of the body. If the rotational equations of motion are expressed in the body-fixed $\xi\eta\varsigma$ reference frame; i.e.,

$$\mathbf{J}_i\dot{\boldsymbol{\omega}}_i + \tilde{\boldsymbol{\omega}}_i\mathbf{J}_i\boldsymbol{\omega}_i = \mathbf{n}_i \tag{2.5}$$

then the inertial tensor $\mathbf{J}_i$ is constant. Equation (2.4) can be expressed in matrix form as

$$\begin{bmatrix} \mathbf{M}_i & \mathbf{0} \\ \mathbf{0} & \mathbf{J}_i \end{bmatrix} \begin{bmatrix} \ddot{\mathbf{r}}_i \\ \dot{\boldsymbol{\omega}}_i \end{bmatrix} + \begin{bmatrix} \mathbf{0} \\ \tilde{\boldsymbol{\omega}}_i \mathbf{J}_i \boldsymbol{\omega}_i \end{bmatrix} = \begin{bmatrix} \mathbf{f}_i \\ \mathbf{n}_i \end{bmatrix} \tag{2.6}$$

where

$$\mathbf{M}_i = \text{diag}(m_i, m_i, m_i) \tag{2.7}$$

2.1.4 A system of unconstrained rigid bodies

Consider *l* bodies in a multibody system that are not linked to each other except through force elements. The Newton-Euler equations of motion for each body are expressed as in Eq. (2.6). The equations of motions for all bodies can be stacked into a single matrix form as

$$\begin{bmatrix} \mathbf{M}_1 & & & & \\ & \mathbf{J}_1 & & \mathbf{0} & \\ & & \ddots & & \\ & \mathbf{0} & & \mathbf{M}_l & \\ & & & & \mathbf{J}_l \end{bmatrix} \begin{bmatrix} \ddot{\mathbf{r}}_1 \\ \dot{\boldsymbol{\omega}}_1 \\ \vdots \\ \ddot{\mathbf{r}}_l \\ \dot{\boldsymbol{\omega}}_l \end{bmatrix} = \begin{bmatrix} \mathbf{f}_1 \\ \mathbf{n}_1 - \tilde{\boldsymbol{\omega}}_1 \mathbf{J}_1 \boldsymbol{\omega}_1 \\ \vdots \\ \mathbf{f}_l \\ \mathbf{n}_l - \tilde{\boldsymbol{\omega}}_l \mathbf{J}_l \boldsymbol{\omega}_l \end{bmatrix} \tag{2.8}$$

or

$$\boldsymbol{M}\dot{\mathbf{v}} = \mathbf{g} \tag{2.9}$$

where $\mathbf{v} = \begin{bmatrix} \dot{\mathbf{r}}_1^T & \boldsymbol{\omega}_1^T & \cdots & \dot{\mathbf{r}}_l^T & \boldsymbol{\omega}_l^T \end{bmatrix}^T$. Equation (2.9) represents the governing equations of motion for an unconstrained system of bodies.

2.1.5 A system of constrained rigid bodies

Consider the same multibody system as in the previous section, but this time we assume that some of the bodies are linked together through kinematic joints. A kinematic joint links two rigid bodies together with the possibility of relative movement between

them. This imperfectly joining of two bodies permits certain relative degrees-of-freedom and prevents or restricts the others. The restriction is defined through *m* independent constraint equations. If the vector of coordinates for all the bodies is denoted by $\mathbf{q} = \begin{bmatrix} \mathbf{r}_1^T & \mathbf{e}_1^T & \cdots & \mathbf{r}_l^T & \mathbf{e}_l^T \end{bmatrix}^T$, where $\mathbf{e}_i$ are the Euler parameters (or any other set of rotational coordinates) of body *i*, the constraint equations can be denoted as

$$\boldsymbol{\Phi} \equiv \boldsymbol{\Phi}(\mathbf{q}) = \mathbf{0} \tag{2.10}$$

Note, $\dot{\mathbf{q}} \neq \mathbf{v}$, since $\mathbf{q}$ contains the orientation of a body in Euler parameters, but $\mathbf{v}$ contains the angular velocities. However, a direct relationship between $\dot{\mathbf{q}}$ and $\mathbf{v}$ can be established. The first time derivative of the constraint equations is

$$\dot{\boldsymbol{\Phi}} \equiv \frac{\partial \boldsymbol{\Phi}}{\partial \mathbf{q}} \dot{\mathbf{q}} = \mathbf{D}\mathbf{v} = \mathbf{0} \tag{2.11}$$

The matrix $\mathbf{D}$ is called the Jacobian of the constraint equation. The second derivative of the constraint equation is

$$\ddot{\boldsymbol{\Phi}} \equiv \mathbf{D}\dot{\mathbf{v}} + \dot{\mathbf{D}}\mathbf{v} = \mathbf{0} \tag{2.12}$$

Kinematic joints introduce reaction forces and/or moments between bodies. These forces/moments prevent certain degrees-of-freedom of relative motion between the bodies. Reaction forces and moments from all joints in the system can be expressed as a constraint force vector $\mathbf{g}^{(c)}$ and added to the array of forces/moment in Eq. (2.9):

$$\boldsymbol{M}\dot{\mathbf{q}} = \mathbf{g} + \mathbf{g}^{(c)} \tag{2.13}$$

It can be shown that the constraint force vector can be expressed as a linear combination of the rows of the Jacobian matrix as

$$\mathbf{g}^{(c)} = \mathbf{D}^T \boldsymbol{\lambda} \tag{2.14}$$

where $\boldsymbol{\lambda}$ is a *m*-vector of so-called *Lagrange multipliers* [13]. By substituting Eq. (2.14) into Eq. (2.13) the equations of motion for the system can be expressed as

$$\boldsymbol{M}\dot{\mathbf{v}} = \mathbf{g} + \mathbf{D}^T \boldsymbol{\lambda} \tag{2.15}$$

However, Eq. (2.15) contains $3l$ equations, but includes $3l + m$ unknowns due to the Lagrange multipliers. Additional *m* equations are required in order to solve the equations of motion of a system of constrained bodies. This can be accomplished by appending the second-time derivative of the constraint equations to Eq. (2.15); i.e.,

$$\begin{bmatrix} \boldsymbol{M} & -\mathbf{D}^T \\ \mathbf{D} & \mathbf{0} \end{bmatrix} \begin{bmatrix} \dot{\mathbf{v}} \\ \boldsymbol{\lambda} \end{bmatrix} = \begin{bmatrix} \mathbf{g} \\ \boldsymbol{\gamma} \end{bmatrix} \tag{2.16}$$

where $\boldsymbol{\gamma} = -\dot{\mathbf{D}}\mathbf{v}$. Note, Eq. (2.16) has $3l + m$ unknowns and $3l + m$ equations and is therefore solvable.

2.2 Deformable body dynamics

For a rigid body, it is assumed that the distance between two arbitrary points on a body remains constant; i.e., if a force is applied at any point on the body, the resultant stresses set every other point on the body in motion instantaneously. As it is shown in the previous sections, the force produces a linear acceleration of the body's centroid and an angular acceleration. This is significantly different for a deformable body. Here, relative motion between arbitrary points on the body exists, which has a significant effect on the body's dynamics. Unlike in rigid bodies, a force that is applied to a point on a

deformable body does not set other points in motion instantaneously. The effect of the force must first propagate through the body.

This section introduces the equations of motion of a deformable body that undergoes large translational and rotational displacements using the floating frame of reference formulation. Here, an emphasis is put on the coupling between the reference position/orientation and the elastic deformation of a body.

2.2.1 Nodal degrees-of-Freedom

If a deformable body is described by a finite element mesh, each node of this mesh can have up to six DoF, three translational and three rotational. If a flexible body is described by n nodes and the nodes are allowed to perform translational and rotational deflections, then the body has $m_{DoF} = 6 \times n$ DoF. If none of the nodes of a deformable body is constrained, six of the degrees-of-freedom of the body are called rigid-body (gross) DoF. However, in the following sections in order to simplify the form of the equations of motion, without loss of generality it is assumed that a finite element node exhibits only three translational DoF.

2.2.2 Node positions

The position of a typical node i with respect to the origin of the body frame in its undeformed state is denoted by a 3-vector $\mathbf{s}^i$, as shown in Figure 2-3. The position of the node in the deformed state is defined by $\mathbf{r}^i = \mathbf{s}^i + \boldsymbol{\delta}^i$, whereby $\boldsymbol{\delta}^i$ is the displacement of node i. These arrays are expressed in the body $\xi\eta\varsigma$ frame.

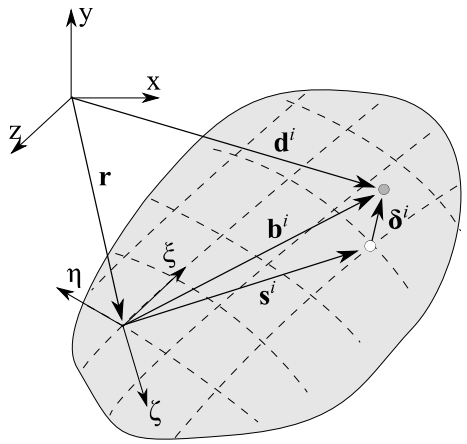

Figure 2-3: A typical node at its undeformed and deformed position.

2.2.3 Equations of motion without reference conditions

Assume a deformable body with n nodes, where each node exhibits only three translational degrees-of-freedom. The mass and stiffness matrix have size $m_{DoF} \times m_{DoF}$, where $m_{DoF} = 3 \times n$. For the moment, the body frame is not allowed to move. The equations of motion for such a body are expressed as [3]

$$\mathbf{M}\ddot{\boldsymbol{\delta}} = \mathbf{f} - \mathbf{K}\boldsymbol{\delta} \tag{2.17}$$

where $\mathbf{f}$ contains the external forces that act on the system. For readability the damping terms are disregarded, but can be easily included here and in any of the following equations. Note, that the stiffness matrix $\mathbf{K}$ has a rank deficiency of six, since no constraint conditions are imposed on the body.

Next, a fixed inertial *xyz* frame is introduced that does not coincide with the body frame, as shown in Figure 2-3. A rotation matrix **A** is defined between these two frames, which allows a vector that is expressed in the body frame to be represented in the inertial frame; e.g., $\boldsymbol{\delta}^i = \mathbf{A}\boldsymbol{\delta}'^i$. Equation (2.17) can be expressed in the inertial frame as [3]

$$\mathbf{M}\ddot{\boldsymbol{\delta}} = \mathbf{f} - \mathbf{K}\boldsymbol{\delta} \tag{2.18}$$

where

$$\mathbf{M} = \mathbf{A}\cancel{\mathbf{M}}\mathbf{A}^T, \quad \mathbf{K} = \mathbf{A}\cancel{\mathbf{K}}\mathbf{A}^T, \quad \mathbf{f} = \mathbf{A}\cancel{\mathbf{f}} \tag{2.19}$$

Now, assume that the body frame can move relative to the fixed inertial frame. The equations of motion for the deformable body change to

$$\mathbf{M}\ddot{\mathbf{d}} = \mathbf{f} - \mathbf{K}\boldsymbol{\delta} \tag{2.20}$$

where $\ddot{\mathbf{d}}$ is the absolute nodal acceleration described in the inertial frame. The absolute position for node *i* is defined as [3]

$$\mathbf{d}^i = \mathbf{r} + \mathbf{s}^i + \boldsymbol{\delta}^i = \mathbf{r} + \mathbf{b}^i \tag{2.21}$$

with $\mathbf{r}$ being the position vector of the body frame in respect to the inertial frame. The absolute velocity and acceleration of node *i* is

$$\dot{\mathbf{d}}^i = \dot{\mathbf{r}} - \tilde{\mathbf{s}}^i\boldsymbol{\omega} + \dot{\boldsymbol{\delta}}^i_{rel} - \tilde{\boldsymbol{\delta}}^i\boldsymbol{\omega} = \dot{\mathbf{r}} - \tilde{\mathbf{b}}^i\boldsymbol{\omega} + \dot{\boldsymbol{\delta}}^i_{rel} \tag{2.22}$$

$$\ddot{\mathbf{d}}^i = \ddot{\mathbf{r}} - \tilde{\mathbf{b}}^i\dot{\boldsymbol{\omega}} + \ddot{\boldsymbol{\delta}}^i_{rel} + \tilde{\boldsymbol{\omega}}\tilde{\boldsymbol{\omega}}\mathbf{b}^i + 2\tilde{\boldsymbol{\omega}}\dot{\boldsymbol{\delta}}^i_{rel} \tag{2.23}$$

where $\boldsymbol{\omega}$ and $\dot{\boldsymbol{\omega}}$ are the angular velocity and acceleration of the body frame. The position, velocity, and acceleration for all nodes can be written as

$$\mathbf{d} = \hat{\mathbf{I}}\mathbf{r} + \mathbf{b} \tag{2.24}$$

$$\dot{\mathbf{d}} = \hat{\mathbf{I}}\dot{\mathbf{r}} - \hat{\tilde{\mathbf{b}}}\boldsymbol{\omega} + \dot{\boldsymbol{\delta}}_{rel} = \begin{bmatrix} \hat{\mathbf{I}} & -\hat{\tilde{\mathbf{b}}} & \bar{\mathbf{I}} \end{bmatrix} \begin{bmatrix} \dot{\mathbf{r}} \\ \boldsymbol{\omega} \\ \dot{\boldsymbol{\delta}}_{rel} \end{bmatrix} \tag{2.25}$$

$$\ddot{\mathbf{d}} = \hat{\mathbf{I}}\ddot{\mathbf{r}} - \hat{\tilde{\mathbf{b}}}\dot{\boldsymbol{\omega}} + \ddot{\boldsymbol{\delta}}_{rel} + \mathbf{w} = \begin{bmatrix} \hat{\mathbf{I}} & -\hat{\tilde{\mathbf{b}}} & \bar{\mathbf{I}} \end{bmatrix} \begin{bmatrix} \ddot{\mathbf{r}} \\ \dot{\boldsymbol{\omega}} \\ \ddot{\boldsymbol{\delta}}_{rel} \end{bmatrix} + \mathbf{w} \tag{2.26}$$

where

$$\mathbf{w} = \bar{\tilde{\boldsymbol{\omega}}}\bar{\tilde{\boldsymbol{\omega}}}\mathbf{b} + 2\bar{\tilde{\boldsymbol{\omega}}}\dot{\boldsymbol{\delta}}_{rel} \tag{2.27}$$

Substituting Eq. (2.26) into Eq. (2.20) yields

$$\begin{bmatrix} \mathbf{M}\hat{\mathbf{I}} & -\mathbf{M}\hat{\mathbf{b}} & \mathbf{M} \end{bmatrix} \begin{bmatrix} \ddot{\mathbf{r}} \\ \dot{\boldsymbol{\omega}} \\ \ddot{\boldsymbol{\delta}}_{rel} \end{bmatrix} = \mathbf{g} \tag{2.28}$$

where

$$\mathbf{g} = \mathbf{f} - \mathbf{M}\mathbf{w} - \mathbf{K}\boldsymbol{\delta} \tag{2.29}$$

Equation (2.28) has $m_{DoF} + 6$ unknowns, but only m_{DoF} equations, and hence, cannot be solved in this form. This deficiency of equations results from the fact that the position and orientation of the body frame with respect to the deformable body is not clearly defined. The following section discusses how the body frame can be attached to the deformable body through a set of axis conditions.

2.2.4 Equations of motion with reference conditions

In order to attach a reference frame to a deformable body, six axis conditions are required. These conditions will decrease the relative degrees-of-freedom between the body and the reference frame; i.e., $m_{DoF} = 6n - 6$. Hence, if the frame is fixed to the ground, the deformable body loses its rigid-body DoF. There are three known methods to attach a frame to a body [3]. In the following all three methods will be introduced. Additionally to the three known methods, a new fourth method will be introduced as well.

2.2.5 Nodal-fixed axis conditions

The simplest and the most common method is the use of the nodal-fixed axis conditions. Here, only three nodes are required to define a reference frame. The origin of the frame is attached to node *a* that provides three conditions. Then node *b* is required to align with the ξ - axis, which includes two more conditions, and finally, a third node *c* remains on the $\xi-\eta$ plane providing the last condition. These conditions can also be written as

$$\delta\!\!\!/^{a}_{\xi} = \delta\!\!\!/^{a}_{\eta} = \delta\!\!\!/^{a}_{\varsigma} = 0, \quad \delta\!\!\!/^{b}_{\eta} = \delta\!\!\!/^{b}_{\varsigma} = 0, \quad \delta\!\!\!/^{c}_{\varsigma} = 0 \tag{2.30}$$

In order to implement these conditions, the array of nodal displacement and its corresponding acceleration array are split into two sets. The first set consists of six zeros, which corresponds to the six axis conditions from Eq. (2.30), and the second set contains the remaining deflections denoted by superscript *f* (*free*):

$$\delta\!\!\!/ = \begin{Bmatrix} \mathbf{0} \\ \delta\!\!\!/^{f} \end{Bmatrix}, \quad \ddot{\delta}\!\!\!/_{rel} = \begin{Bmatrix} \mathbf{0} \\ \ddot{\delta}\!\!\!/^{f}_{rel} \end{Bmatrix} \tag{2.31}$$

With the reference conditions of Eq. (2.30) and the partitioning of Eq. (2.31), Eq. (2.28) becomes

$$\begin{bmatrix} \mathbf{M}\hat{\mathbf{I}} & -\mathbf{M}\hat{\tilde{\mathbf{b}}} & \bar{\mathbf{A}}M\!\!\!/^{f} \end{bmatrix} \begin{bmatrix} \ddot{\mathbf{r}} \\ \dot{\boldsymbol{\omega}} \\ \ddot{\delta}\!\!\!/^{f}_{rel} \end{bmatrix} = \mathbf{g} \tag{2.32}$$

where $M\!\!\!/^{f}$ is the mass matrix whose columns, that are associated with the six conditions, are eliminated. Equation (2.32) has m_{DoF} unknowns and m_{DoF} equations.

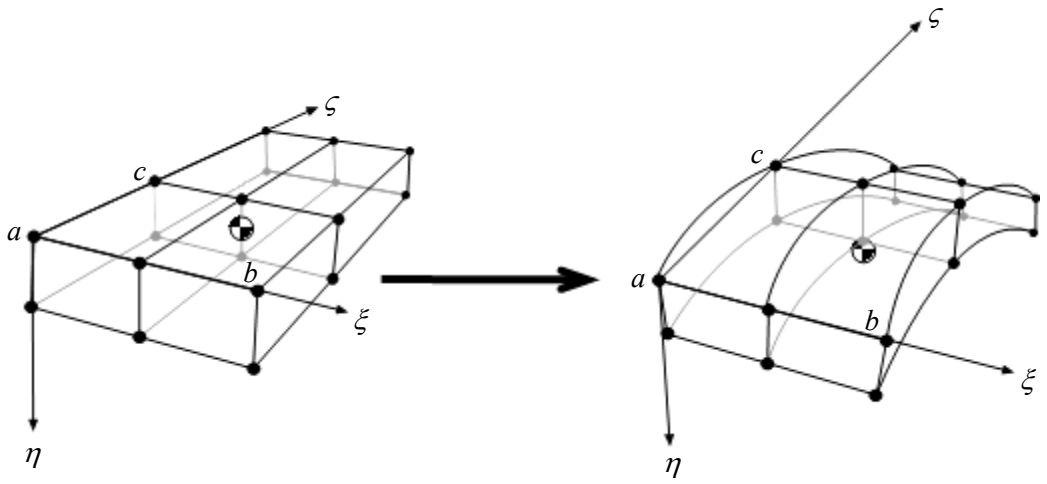

Figure 2-4: Reference axes attached on nodes (Nodal fixed axis conditions).

2.2.6 Mean axis conditions

Mean axis conditions [1,3,74,76] can be established by minimizing the kinetic energy associated with deformation only. If the kinetic energy is written as

$$T = \frac{1}{2}\dot{\boldsymbol{\delta}}_{rel}^{T}\mathbf{M}\dot{\boldsymbol{\delta}}_{rel} = \frac{1}{2}\left(\dot{\mathbf{d}} - \hat{\mathbf{I}}\dot{\mathbf{r}} + \hat{\tilde{\mathbf{b}}}\boldsymbol{\omega}\right)^{T}\mathbf{M}\left(\dot{\mathbf{d}} - \hat{\mathbf{I}}\dot{\mathbf{r}} + \hat{\tilde{\mathbf{b}}}\boldsymbol{\omega}\right) \tag{2.33}$$

then the partial derivatives of the kinetic energy with respect to translational and rotational velocity vectors of the reference frame are

$$\begin{aligned} T_{\dot{\mathbf{r}}} &= -\left(\dot{\mathbf{d}} - \hat{\mathbf{I}}\dot{\mathbf{r}} + \hat{\tilde{\mathbf{b}}}\boldsymbol{\omega}\right)^{T}\mathbf{M}\hat{\mathbf{I}} = -\dot{\boldsymbol{\delta}}_{rel}^{T}\mathbf{M}\hat{\mathbf{I}} \\ T_{\boldsymbol{\omega}} &= \left(\dot{\mathbf{d}} - \hat{\mathbf{I}}\dot{\mathbf{r}} + \hat{\tilde{\mathbf{b}}}\boldsymbol{\omega}\right)^{T}\mathbf{M}\hat{\tilde{\mathbf{b}}} = \dot{\boldsymbol{\delta}}_{rel}^{T}\mathbf{M}\hat{\tilde{\mathbf{b}}} \end{aligned} \tag{2.34}$$

The mean axis conditions can be obtained by setting these partial derivatives to zero; i.e., $T_{\dot{\mathbf{r}}} = T_{\boldsymbol{\omega}} = 0$. By applying the time derivative to these conditions and after some simplifications, the following conditions can be obtained

$$\hat{\mathbf{I}}^{T}\mathbf{M}\ddot{\boldsymbol{\delta}}_{rel} = \mathbf{0} \tag{2.35}$$

$$\hat{\tilde{\mathbf{b}}}^T \mathbf{M} \ddot{\boldsymbol{\delta}}_{rel} = \mathbf{0} \tag{2.36}$$

If the origin of the reference frame, in the undeformed state of the body, is positioned at the mass center; i.e., $\hat{\mathbf{I}}^T \mathbf{M} \mathbf{s} = 0$, then it will remain at the instantaneous mass center as the body deforms. Equations (2.35) and (2.36) can be appended to Eq. (2.28) to form the equations of motion with the mean-axis conditions

$$\begin{bmatrix} \mathbf{M}\hat{\mathbf{I}} & -\mathbf{M}\hat{\tilde{\mathbf{b}}} & \mathbf{M} \\ \mathbf{0} & \mathbf{0} & \hat{\mathbf{I}}^T \mathbf{M} \\ \mathbf{0} & \mathbf{0} & \hat{\tilde{\mathbf{b}}}^T \mathbf{M} \end{bmatrix} \begin{bmatrix} \ddot{\mathbf{r}} \\ \dot{\boldsymbol{\omega}} \\ \ddot{\boldsymbol{\delta}}_{rel} \end{bmatrix} = \begin{bmatrix} \mathbf{g} \\ \mathbf{0} \\ \mathbf{0} \end{bmatrix} \tag{2.37}$$

Another form of the equations of motion can be constructed if Eq. (2.28) is premultiplied by the transpose of the coefficient matrix of Eq. (2.26):

$$\begin{bmatrix} \hat{\mathbf{I}}^T \mathbf{M} \hat{\mathbf{I}} & -\hat{\mathbf{I}}^T \mathbf{M} \hat{\tilde{\mathbf{b}}} & \hat{\mathbf{I}}^T \mathbf{M} \\ -\hat{\tilde{\mathbf{b}}}^T \mathbf{M} \hat{\mathbf{I}} & \hat{\tilde{\mathbf{b}}}^T \mathbf{M} \hat{\tilde{\mathbf{b}}} & -\hat{\tilde{\mathbf{b}}}^T \mathbf{M} \\ \mathbf{M}\hat{\mathbf{I}} & -\mathbf{M}\hat{\tilde{\mathbf{b}}} & \mathbf{M} \end{bmatrix} \begin{Bmatrix} \ddot{\mathbf{r}} \\ \dot{\boldsymbol{\omega}} \\ \ddot{\boldsymbol{\delta}}_{rel} \end{Bmatrix} = \begin{Bmatrix} \hat{\mathbf{I}}^T \mathbf{g} \\ -\hat{\tilde{\mathbf{b}}}^T \mathbf{g} \\ \mathbf{g} \end{Bmatrix} \tag{2.38}$$

If the mass matrix is properly constructed; i.e., it is constructed directly by a finite element program and has not been condensed to a smaller size, it can be shown that [3]

$$\hat{\mathbf{I}}^T \mathbf{M} \hat{\tilde{\mathbf{b}}} = \hat{\tilde{\mathbf{b}}}^T \mathbf{M} \hat{\mathbf{I}} = \mathbf{0} \tag{2.39}$$

Substituting Eqs. (2.35), (2.36), and (2.39) into Eq. (2.38) yields [74]:

$$\begin{bmatrix} m\mathbf{I} & \mathbf{0} & \mathbf{0} \\ \mathbf{0} & \mathbf{J} & \mathbf{0} \\ \mathbf{M}\hat{\mathbf{I}} & -\mathbf{M}\hat{\tilde{\mathbf{b}}} & \mathbf{M} \end{bmatrix} \begin{Bmatrix} \ddot{\mathbf{r}} \\ \dot{\boldsymbol{\omega}} \\ \ddot{\boldsymbol{\delta}}_{rel} \end{Bmatrix} = \begin{Bmatrix} \hat{\mathbf{I}}^T \mathbf{g} \\ -\hat{\tilde{\mathbf{b}}}^T \mathbf{g} \\ \mathbf{g} \end{Bmatrix} \tag{2.40}$$

where $\hat{\mathbf{I}}^T\mathbf{M}\hat{\mathbf{I}} = m\mathbf{I}$ and $\hat{\tilde{\mathbf{b}}}^T\mathbf{M}\hat{\tilde{\mathbf{b}}} = \mathbf{J}$ has been used. Here, m is the total mass of the deformable body and $\mathbf{J}$ the body's inertial matrix. It should be mentioned that on the right hand side of Eq. (2.40) the following simplifications can be made:

$$\hat{\mathbf{I}}^T\mathbf{K}\boldsymbol{\delta} = 0, \quad \hat{\tilde{\mathbf{b}}}^T\mathbf{K}\boldsymbol{\delta} = 0 \tag{2.41}$$

which states that the sum of internal forces and moments are zero [3].

2.2.7 Principal axis conditions

Another set of conditions can be obtained by the principal axis conditions [3,75]. Here, the body frame is required to coincide with the principal axes as the body deforms. Furthermore, the origin of the body must be kept at the instantaneous center, which is similar to the translational mean axis conditions. Therefore, the same set of equations (Eqs. (2.35), (2.36), and (2.39)) can be used here. For nodes with translational degrees-of-freedom, the rotational conditions are defined as

$$\begin{aligned}
\cancel{\mathbf{b}}^T\cancel{\mathbf{M}}_{\xi\eta}\ddot{\cancel{\boldsymbol{\delta}}}_{rel} &= -\dot{\cancel{\boldsymbol{\delta}}}_{rel}{}^T\cancel{\mathbf{M}}_{\xi\eta}\dot{\cancel{\boldsymbol{\delta}}}_{rel} \\
\cancel{\mathbf{b}}^T\cancel{\mathbf{M}}_{\xi\varsigma}\ddot{\cancel{\boldsymbol{\delta}}}_{rel} &= -\dot{\cancel{\boldsymbol{\delta}}}_{rel}{}^T\cancel{\mathbf{M}}_{\xi\varsigma}\dot{\cancel{\boldsymbol{\delta}}}_{rel} \\
\cancel{\mathbf{b}}^T\cancel{\mathbf{M}}_{\eta\varsigma}\ddot{\cancel{\boldsymbol{\delta}}}_{rel} &= -\dot{\cancel{\boldsymbol{\delta}}}_{rel}{}^T\cancel{\mathbf{M}}_{\eta\varsigma}\dot{\cancel{\boldsymbol{\delta}}}_{rel}
\end{aligned} \tag{2.42}$$

where

$$\begin{aligned}
\cancel{\mathbf{M}}_{\xi\eta} &= \cancel{\mathbf{N}}_{\xi\eta}^T + \cancel{\mathbf{N}}_{\xi\eta}, \quad \cancel{\mathbf{N}}_{\xi\eta} = \bar{\mathbf{C}}_\xi^T\mathbf{M}\bar{\mathbf{C}}_\eta \\
\cancel{\mathbf{M}}_{\xi\varsigma} &= \cancel{\mathbf{N}}_{\xi\varsigma}^T + \cancel{\mathbf{N}}_{\xi\varsigma}, \quad \cancel{\mathbf{N}}_{\xi\varsigma} = \bar{\mathbf{C}}_\xi^T\mathbf{M}\bar{\mathbf{C}}_\varsigma \\
\cancel{\mathbf{M}}_{\eta\varsigma} &= \cancel{\mathbf{N}}_{\eta\varsigma}^T + \cancel{\mathbf{N}}_{\eta\varsigma}, \quad \cancel{\mathbf{N}}_{\eta\varsigma} = \bar{\mathbf{C}}_\eta^T\mathbf{M}\bar{\mathbf{C}}_\varsigma
\end{aligned} \tag{2.43}$$

and

$$\mathbf{C}_\xi \equiv \begin{bmatrix} 0 & 0 & 0 \\ 0 & 0 & 1 \\ 0 & -1 & 0 \end{bmatrix}, \quad \mathbf{C}_\eta \equiv \begin{bmatrix} 0 & 0 & -1 \\ 0 & 0 & 0 \\ 1 & 0 & 0 \end{bmatrix}, \quad \mathbf{C}_\varsigma \equiv \begin{bmatrix} 0 & 1 & 0 \\ -1 & 0 & 0 \\ 0 & 0 & 0 \end{bmatrix} \tag{2.44}$$

which are called *selector* matrices.

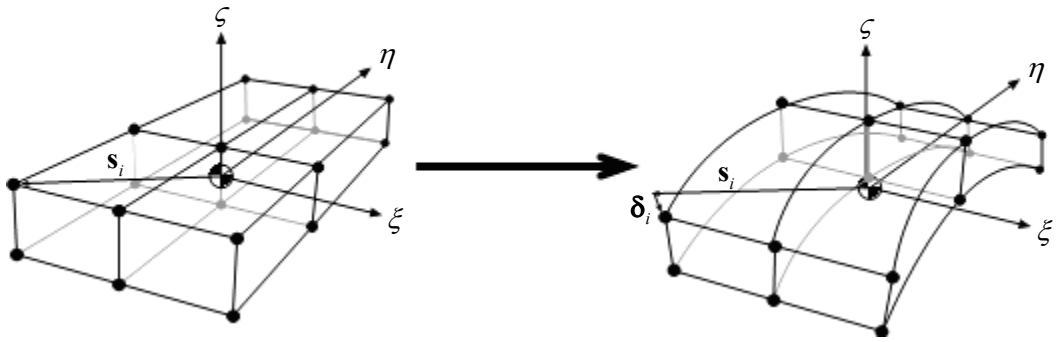

Figure 2-5: Reference axes on the instantaneous center of mass (Mean axis and principle axis conditions).

2.2.8 Rigid-deformable body axis conditions

Some systems consist of a rigid body and a deformable body that are mutually fixed to each other on their contacting surface. This bond allows the rigid and deformable body to share the same body-fixed reference frame. Although the body frame can be attached to the deformable body, many simplifications can be obtained if the reference frame is fixed to the center of mass of the rigid body. An example of such a system is the wheel-tire. The wheel's material is usually based on steel or aluminum alloy and, due to their high modulus of elasticity, the wheel can be considered to be rigid. The tire on the other hand consists of rubber like material and, hence, is of deformable nature. Even though tire and wheel are separate bodies, they share a contact area along the inner rim of the tire and the outer rim of the wheel. Once the tire is properly inflated, separation and relative slip at this surface is very unlikely.

The equations of motion for the rigid body, as shown in Figure 2-6, are represented by Eq. (2.6). The equations of motions for the deformable body undergoing large motion are expressed in Eq. (2.20).

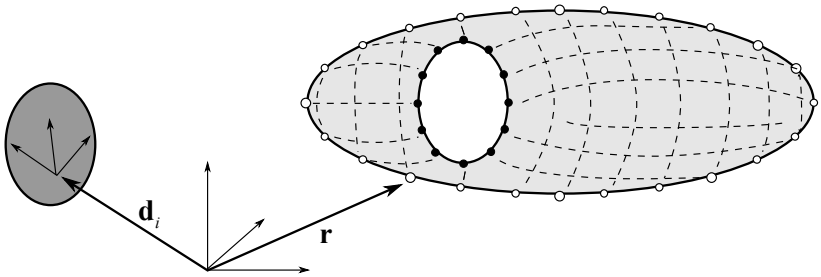

Figure 2-6: Rigid and deformable body detached.

In the deformable body, the nodes are split into two groups: the nodes that are and remain in contact to the rigid body, denoted by the super-script "*w*"; and the free (remaining) nodes, denoted by the super-script "*f*". Therefore, the nodal matrices and arrays can be partitioned as $\mathbf{M}=\begin{bmatrix}\mathbf{M}^w & \mathbf{0}\\ \mathbf{0} & \mathbf{M}^f\end{bmatrix}$, $\mathbf{K}=\begin{bmatrix}\mathbf{K}^{ww} & \mathbf{K}^{wf}\\ \mathbf{K}^{fw} & \mathbf{K}^{ff}\end{bmatrix}$, $\ddot{\mathbf{d}}=\begin{Bmatrix}\ddot{\mathbf{d}}^w\\ \ddot{\mathbf{d}}^f\end{Bmatrix}$, and $\boldsymbol{\delta}=\begin{Bmatrix}\mathbf{0}\\ \boldsymbol{\delta}^f\end{Bmatrix}$. The deflections of the *w* nodes are zero, since they are constrained to the rigid body. The equations of motion for a rigid-deformable combination are constructed by combining Eq. (2.6) and Eq. (2.20). The combined equations of motion is expressed as

$$\begin{bmatrix} m^o\mathbf{I} & \mathbf{0} & \mathbf{0} & \mathbf{0}\\ \mathbf{0} & \mathbf{J}^o & \mathbf{0} & \mathbf{0}\\ \mathbf{0} & \mathbf{0} & \mathbf{M}^w & \mathbf{0}\\ \mathbf{0} & \mathbf{0} & \mathbf{0} & \mathbf{M}^f \end{bmatrix}\begin{Bmatrix}\ddot{\mathbf{r}}\\ \dot{\boldsymbol{\omega}}\\ \ddot{\mathbf{d}}^w\\ \ddot{\mathbf{d}}^f\end{Bmatrix}=\begin{Bmatrix}\mathbf{f}^o\\ \mathbf{n}^o-\tilde{\boldsymbol{\omega}}\mathbf{J}^o\boldsymbol{\omega}\\ \mathbf{f}^w-\mathbf{K}^{wf}\boldsymbol{\delta}^f\\ \mathbf{f}^f-\mathbf{K}^{ff}\boldsymbol{\delta}^f\end{Bmatrix}+\mathbf{D}^T\boldsymbol{\lambda} \tag{2.45}$$

where the superscript "*o*" denotes the rigid body. The matrix **D** is the Jacobian matrix of the constraints between the *w* nodes and the rigid body, and $\boldsymbol{\lambda}$ is an array of Lagrange multipliers. There is no need to determine the detailed elements of the Jacobin matrix

since it will be eliminated from the equations of motion in the following step. If the FE model of the deformable body shares the same moving frame as the frame that is positioned at the mass center of the rigid body, a typical w node can be positioned as $\mathbf{d}_i^w = \mathbf{r} + \mathbf{s}_i^w$ as shown in Figure 2-7. This leads to the following velocity and acceleration equations:

$$\begin{aligned} \dot{\mathbf{d}}_i^w &= \dot{\mathbf{r}} - \tilde{\mathbf{s}}_i^w \boldsymbol{\omega} \\ \ddot{\mathbf{d}}_i^w &= \ddot{\mathbf{r}} - \tilde{\mathbf{s}}_i^w \dot{\boldsymbol{\omega}} + \tilde{\boldsymbol{\omega}}\tilde{\boldsymbol{\omega}}\mathbf{s}_i^w \end{aligned} \tag{2.46}$$

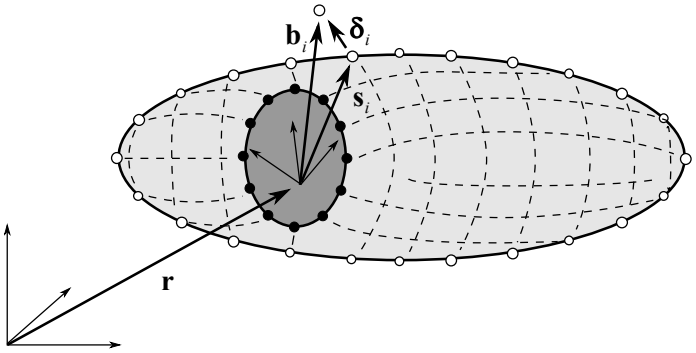

Figure 2-7: Rigid and deformable body linked.

If the acceleration equations are stacked for all of the w nodes, the following acceleration transformation is found:

$$\begin{Bmatrix} \ddot{\mathbf{r}} \\ \dot{\boldsymbol{\omega}} \\ \ddot{\mathbf{d}}^w \\ \ddot{\mathbf{d}}^f \end{Bmatrix} = \begin{bmatrix} \mathbf{I} & \mathbf{0} & \mathbf{0} \\ \mathbf{0} & \mathbf{I} & \mathbf{0} \\ \hat{\mathbf{I}}^w & -\hat{\tilde{\mathbf{s}}}^w & \mathbf{0} \\ \mathbf{0} & \mathbf{0} & \bar{\mathbf{I}} \end{bmatrix} \begin{Bmatrix} \ddot{\mathbf{r}} \\ \dot{\boldsymbol{\omega}} \\ \ddot{\mathbf{d}}^f \end{Bmatrix} + \begin{Bmatrix} \mathbf{0} \\ \mathbf{0} \\ \bar{\tilde{\boldsymbol{\omega}}}\bar{\tilde{\boldsymbol{\omega}}}\mathbf{s}^w \\ \mathbf{0} \end{Bmatrix} \tag{2.47}$$

This transformation equation is substituted in Eq.(2.45) and the resultant is pre-multiplied by the transpose of the transformation matrix to find the new form of the equations of motion as:

$$\begin{bmatrix} m^o\mathbf{I}+\hat{\mathbf{I}}^{wT}\mathbf{M}^w\hat{\mathbf{I}}^w & -\hat{\mathbf{I}}^{wT}\mathbf{M}^w\hat{\tilde{\mathbf{s}}}^w & \mathbf{0} \\ -\hat{\tilde{\mathbf{s}}}^{wT}\mathbf{M}^w\hat{\mathbf{I}}^w & \mathbf{J}^o+\hat{\tilde{\mathbf{s}}}^{wT}\mathbf{M}^w\hat{\tilde{\mathbf{s}}}^w & \mathbf{0} \\ \mathbf{0} & \mathbf{0} & \mathbf{M}^f \end{bmatrix} \begin{Bmatrix} \ddot{\mathbf{r}} \\ \dot{\boldsymbol{\omega}} \\ \ddot{\mathbf{d}}^f \end{Bmatrix} = \begin{Bmatrix} \mathbf{f}^o+\hat{\mathbf{I}}^{wT}\left(\mathbf{f}^w-\mathbf{K}^{wf}\boldsymbol{\delta}^f+\mathbf{M}^w\bar{\tilde{\boldsymbol{\omega}}}\bar{\tilde{\boldsymbol{\omega}}}\mathbf{s}^w\right) \\ \mathbf{n}^o-\tilde{\boldsymbol{\omega}}\mathbf{J}^o\boldsymbol{\omega}-\hat{\tilde{\mathbf{s}}}^{wT}\left(\mathbf{f}^w-\mathbf{K}^{wf}\boldsymbol{\delta}^f+\mathbf{M}^w\bar{\tilde{\boldsymbol{\omega}}}\bar{\tilde{\boldsymbol{\omega}}}\mathbf{s}^w\right) \\ \mathbf{f}^f-\mathbf{K}^{ff}\boldsymbol{\delta}^f \end{Bmatrix} \quad (2.48)$$

Since the rigid and deformable body share the same reference frame, Eq. (2.26) can be rewritten as

$$\begin{Bmatrix} \ddot{\mathbf{r}} \\ \dot{\boldsymbol{\omega}} \\ \ddot{\mathbf{d}}^f \end{Bmatrix} = \begin{bmatrix} \mathbf{I} & \mathbf{0} & \mathbf{0} \\ \mathbf{0} & \mathbf{I} & \mathbf{0} \\ \hat{\mathbf{I}}^f & -\hat{\tilde{\mathbf{b}}}^f & \bar{\mathbf{I}}^f \end{bmatrix} \begin{Bmatrix} \ddot{\mathbf{r}} \\ \dot{\boldsymbol{\omega}} \\ \ddot{\boldsymbol{\delta}}^f_{rel} \end{Bmatrix} + \begin{Bmatrix} \mathbf{0} \\ \mathbf{0} \\ \mathbf{w}^f \end{Bmatrix} \quad (2.49)$$

Substituting Eq. (2.49) into Eq. (2.48) results in another form of the equations of motion:

$$\begin{bmatrix} m^o\mathbf{I}+\hat{\mathbf{I}}^{wT}\mathbf{M}^w\hat{\mathbf{I}}^w & -\hat{\mathbf{I}}^{wT}\mathbf{M}^w\hat{\tilde{\mathbf{s}}}^w & \mathbf{0} \\ -\hat{\tilde{\mathbf{s}}}^{wT}\mathbf{M}^w\hat{\mathbf{I}}^w & \mathbf{J}^o+\hat{\tilde{\mathbf{s}}}^{wT}\mathbf{M}^w\hat{\tilde{\mathbf{s}}}^w & \mathbf{0} \\ \mathbf{M}^f\hat{\mathbf{I}}^f & -\mathbf{M}^f\hat{\tilde{\mathbf{b}}}^f & \mathbf{M}^f \end{bmatrix} \begin{Bmatrix} \ddot{\mathbf{r}} \\ \dot{\boldsymbol{\omega}} \\ \ddot{\boldsymbol{\delta}}^f_{rel} \end{Bmatrix} = \begin{Bmatrix} \mathbf{f}^o+\hat{\mathbf{I}}^{wT}\left(\mathbf{f}^w-\mathbf{K}^{wf}\boldsymbol{\delta}^f+\mathbf{M}^w\bar{\tilde{\boldsymbol{\omega}}}\bar{\tilde{\boldsymbol{\omega}}}\mathbf{s}^w\right) \\ \mathbf{n}^o-\tilde{\boldsymbol{\omega}}\mathbf{J}^o\boldsymbol{\omega}-\hat{\tilde{\mathbf{s}}}^{wT}\left(\mathbf{f}^w-\mathbf{K}^{wf}\boldsymbol{\delta}^f+\mathbf{M}^w\bar{\tilde{\boldsymbol{\omega}}}\bar{\tilde{\boldsymbol{\omega}}}\mathbf{s}^w\right) \\ \mathbf{f}^f-\mathbf{K}^{ff}\boldsymbol{\delta}^f-\mathbf{M}^f\mathbf{w}^f \end{Bmatrix} \quad (2.50)$$

This form of the equations of motion for the rigid-deformable system has a very useful characteristic; the rigid body portion is uncoupled from the nodal deformations in the mass matrix. This allows us to solve the rigid body part first, and then the deformation portion; i.e.,

$$\begin{bmatrix} m^o\mathbf{I}+\hat{\mathbf{I}}^{wT}\mathbf{M}^w\hat{\mathbf{I}}^w & -\hat{\mathbf{I}}^{wT}\mathbf{M}^w\hat{\tilde{\mathbf{s}}}^w \\ -\hat{\tilde{\mathbf{s}}}^{wT}\mathbf{M}^w\hat{\mathbf{I}}^w & \mathbf{J}^o+\hat{\tilde{\mathbf{s}}}^{wT}\mathbf{M}^w\hat{\tilde{\mathbf{s}}}^w \end{bmatrix} \begin{Bmatrix} \ddot{\mathbf{r}} \\ \dot{\boldsymbol{\omega}} \end{Bmatrix} = \begin{Bmatrix} \mathbf{f}^o+\hat{\mathbf{I}}^{wT}\left(\mathbf{f}^w-\mathbf{K}^{wf}\boldsymbol{\delta}^f+\mathbf{M}^w\bar{\tilde{\boldsymbol{\omega}}}\bar{\tilde{\boldsymbol{\omega}}}\mathbf{s}^w\right) \\ \mathbf{n}^o-\tilde{\boldsymbol{\omega}}\mathbf{J}^o\boldsymbol{\omega}-\hat{\tilde{\mathbf{s}}}^{wT}\left(\mathbf{f}^w-\mathbf{K}^{wf}\boldsymbol{\delta}^f+\mathbf{M}^w\bar{\tilde{\boldsymbol{\omega}}}\bar{\tilde{\boldsymbol{\omega}}}\mathbf{s}^w\right) \end{Bmatrix} \quad (2.51)$$

$$\mathbf{M}^f\ddot{\boldsymbol{\delta}}^f_{rel} = \mathbf{f}^f-\mathbf{K}^{ff}\boldsymbol{\delta}^f-\mathbf{M}^f\mathbf{w}^f-\begin{bmatrix} \mathbf{M}^f\hat{\mathbf{I}}^f & -\mathbf{M}^f\hat{\tilde{\mathbf{b}}}^f \end{bmatrix}\begin{bmatrix} \ddot{\mathbf{r}} \\ \dot{\boldsymbol{\omega}} \end{bmatrix} \quad (2.52)$$

This characteristic remains true even when the rigid body is attached to other bodies.

2.3 Discussion

The governing equations of motion for a multibody system with rigid and deformable bodies have been introduced in this chapter. In these equations, a deformable body is represented by a FE model. Due to the inability of some elements (non-isoparametric type) of the deformable body, such as beam, plate, and shell elements, to describe large rotations and deformations, the *floating frame of reference* formulation has been introduced. In this approach a reference frame (*body* frame) is assigned to the deformable body through six axis conditions (e.g. nodal fixed axis, mean axis, principal axis, and rigid-deformable body axis conditions). Then, the large translation and rotation of the body are described by the position and orientation of the body frame with respect to an inertial frame. The deformation of the body itself is expressed by nodal coordinates of the elements and measured with respect to the body frame.

While the *floating frame of reference formulation* solves the problem of large rotation for deformable bodies, the problem of large number of degrees-of-freedom of these bodies still persists. The next chapter introduces truncation techniques that can reduce the number of degrees-of-freedom of deformable bodies so that they become adequate for multibody simulations.

3. REDUCTION METHODS FOR DEFORMABLE BODIES

In multibody dynamics, some deformable bodies can be represented through simple finite elements, such as simple rods. However, some bodies have more complex structures, such as the crankshaft of an engine, that require representation using a fine meshed finite element model. These models contain many degrees-of-freedom which leads to computational operation on large matrices. Because of the size of the matrices involved, a direct transient analysis using all of the coordinates may exceed the size limitation of the computer's memory and/or may lead to long computer run times. In order to overcome these limitations, reduction techniques have been developed that reduce the degrees-of freedom of the deformable bodies. Most of the known model reduction techniques have been borrowed from structural analysis. The most well-known methods are static condensation and modal truncation. However, such methods may not be suitable for multibody dynamics. Static condensation does not preserve the eigen-properties of the original model, which leads to significant errors in dynamic problems. Model truncation on the other hand preserves the eigen-properties, but it requires so-called fixed (non-moving) boundary conditions. Unlike in structural analysis, in a multibody system, some of the nodes of the structure might be linked to other moving bodies that lead to moving boundary conditions. Methods known as component mode synthesis (CMS) address the issue of eigen-property preservation and moving boundary conditions [5-7]. The main idea behind these methods is the superposition of different types of modes. The initial purpose of CMS in FEM was the improvement of eigenvalue

solution of large models [20]. However, today it finds its application in several areas including deformable multibody dynamics. Mode condensation [40, 42] is a more recently developed method that extends modal truncation with the assumption that the potential energy with respect to deleted modes is minimal. While this approach is derived differently, it turns out to be equivalent to the Craig-Bampton reduction [7] that is one method of the CMS family.

This chapter introduces four reduction methods for deformable bodies: static condensation, modal truncation, Craig-Bampton reduction (CMS family), and mode condensation.

3.1 Equations of motion for a deformable body

According to the finite element method, a structure is represented by a mass, a stiffness and a damping matrix. For the purpose of readability, damping will be neglected in this chapter; however, it can easily be included in the forthcoming equations. The equations of motion for a deformable body without constraints can be written as

$$\mathbf{M}\ddot{\boldsymbol{\delta}} + \mathbf{K}\boldsymbol{\delta} = \mathbf{f} \tag{3.1}$$

where the mass matrix **M** is considered to be lumped. For the sake of simplicity, the *body* frame of the deformable body coincides with the inertial frame and is fixed in the inertial system. Therefore, no axis conditions between the *body* frame and the deformable body needs to be defined. Since the body might be linked to other moving bodies or ground, the nodes are partitioned into two groups: those that are free, designated as *f*-nodes; and those that are in contact with other moving bodies or ground,

designated as *c*-nodes or contact nodes. If the rows and columns of Eq. (3.1) are reordered such that the free nodes are first, followed by the contact nodes, then

$$\begin{bmatrix} \mathbf{M}^{ff} & \mathbf{0} \\ \mathbf{0} & \mathbf{M}^{cc} \end{bmatrix} \begin{Bmatrix} \ddot{\boldsymbol{\delta}}^{f} \\ \ddot{\boldsymbol{\delta}}^{c} \end{Bmatrix} + \begin{bmatrix} \mathbf{K}^{ff} & \mathbf{K}^{fc} \\ \mathbf{K}^{cf} & \mathbf{K}^{cc} \end{bmatrix} \begin{Bmatrix} \boldsymbol{\delta}^{f} \\ \boldsymbol{\delta}^{c} \end{Bmatrix} = \begin{Bmatrix} \mathbf{f}^{f} \\ \mathbf{f}^{c} \end{Bmatrix} \tag{3.2}$$

The details about how the body is connected to its surrounding are not considered in Eq. (3.2). Since the total degrees-of-freedom for a full model can be large, it is desirable to reduce the problem size by transforming the coordinates into a much smaller set of coordinates. In the following sections different reduction methods will be reviewed.

3.2 Static condensation

The Static or Guyan condensation is built on the assumption that not all nodes of a structure are of equal interest. If, for instance, a fine meshed model is required for static analysis, but too expensive for eigen-analysis, then we may wish to observe only a subset of the nodes. For that purpose, some nodes are kept while others are deleted [4]. In this case, assume the *c*-nodes are kept and the *f*-nodes are deleted. To do so, the inertia of the *f*-nodes is shifted to the *c*-nodes. Furthermore, the external forces that act on the free nodes are properly distributed on the contact nodes. Equation (3.2) is revised to

$$\begin{bmatrix} \mathbf{0} & \mathbf{0} \\ \mathbf{0} & \mathbf{M}_r \end{bmatrix} \begin{Bmatrix} \ddot{\boldsymbol{\delta}}^{f} \\ \ddot{\boldsymbol{\delta}}^{c} \end{Bmatrix} + \begin{bmatrix} \mathbf{K}^{ff} & \mathbf{K}^{fc} \\ \mathbf{K}^{cf} & \mathbf{K}^{cc} \end{bmatrix} \begin{Bmatrix} \boldsymbol{\delta}^{f} \\ \boldsymbol{\delta}^{c} \end{Bmatrix} = \begin{Bmatrix} \mathbf{0} \\ \mathbf{f}_r \end{Bmatrix} \tag{3.3}$$

where $\mathbf{M}_r$ contains the entire inertia of the body and $\mathbf{f}_r$ includes all external forces. The first row of Eq. (3.3) yields

$$\boldsymbol{\delta}^{f} = \boldsymbol{\Psi}_s \boldsymbol{\delta}^{c} \tag{3.4}$$

where

$$\boldsymbol{\Psi}_s = -\left(\mathbf{K}^{ff}\right)^{-1}\mathbf{K}^{fc} \tag{3.5}$$

is the static condensation matrix, whose columns represent the static modes. The column dimension of $\boldsymbol{\Psi}_s$ is equal to the degrees-of-freedom of the contact nodes. The transformation for reduction is

$$\begin{Bmatrix}\boldsymbol{\delta}^f \\ \boldsymbol{\delta}^c\end{Bmatrix} = \begin{bmatrix}\boldsymbol{\Psi}_s \\ \mathbf{I}\end{bmatrix}\boldsymbol{\delta}^c \tag{3.6}$$

Substituting Eq. (3.6) into Eq. (3.2) and pre-multiplying the resulting equation with the transpose of the transformation matrix from Eq. (3.6) yields

$$\mathbf{M}_r\ddot{\boldsymbol{\delta}}^c + \mathbf{K}_r\boldsymbol{\delta}^c = \mathbf{f}_r \tag{3.7}$$

where

$$\begin{aligned}\mathbf{M}_r &= \mathbf{M}^{cc} + \boldsymbol{\Psi}_s^T\mathbf{M}^{ff}\boldsymbol{\Psi}_s \\ \mathbf{K}_r &= \mathbf{K}^{cc} + \mathbf{K}^{cf}\boldsymbol{\Psi}_s + \boldsymbol{\Psi}_s^T\mathbf{K}^{fc} + \boldsymbol{\Psi}_s^T\mathbf{K}^{ff}\boldsymbol{\Psi}_s \\ \mathbf{f}_r &= \boldsymbol{\Psi}_s^T\mathbf{f}^f + \mathbf{f}^c\end{aligned} \tag{3.8}$$

Equation (3.7) represents the reduced equations of motion with $\mathbf{K}_r$ being the reduced stiffness matrix. Once $\boldsymbol{\delta}^c$ is determined, $\boldsymbol{\delta}^f$ can be restored by using Eq. (3.6). Although static condensation can provide exact solutions for static problems, it does not preserve the eigen-properties of the original system and therefore produces significant errors in dynamic problems. It can be shown that a static condensed model has higher (corresponding) natural frequencies than the original model [82].

3.3 Modal truncation

Modal truncation is another conventional approach for model reduction. This method keeps the boundary DoF (DoF of contact nodes) in nodal space and transfers the remaining DoF into modal space:

$$\begin{Bmatrix} \boldsymbol{\delta}^f \\ \boldsymbol{\delta}^c \end{Bmatrix} = \begin{bmatrix} \boldsymbol{\Psi} & \mathbf{0} \\ \mathbf{0} & \mathbf{I} \end{bmatrix} \begin{Bmatrix} \mathbf{z} \\ \boldsymbol{\delta}^c \end{Bmatrix} \tag{3.9}$$

where $\mathbf{z}$ is a set of generalized coordinates. The matrix $\boldsymbol{\Psi}$ can be obtained by holding the contact nodes fixed and disregarding the external forces on the free nodes; i.e.,

$$\mathbf{M}^{ff}\ddot{\boldsymbol{\delta}}^f + \mathbf{K}^{ff}\boldsymbol{\delta}^f = \mathbf{0} \tag{3.10}$$

With the proper modal transformation, Eq. (3.10) can be expressed as a generalized eigen-value problem:

$$\mathbf{K}^{ff}\boldsymbol{\Psi} = \mathbf{M}^{ff}\boldsymbol{\Psi}\boldsymbol{\Lambda} \tag{3.11}$$

The matrix $\boldsymbol{\Psi}$ contains the eigenvectors (also called fixed eigen-modes or fixed normal modes) of the clamped substructure, and are normalized to $\mathbf{M}^{ff}$; i.e., $\boldsymbol{\Psi}^T\mathbf{M}^{ff}\boldsymbol{\Psi} = \mathbf{I}$. The matrix $\boldsymbol{\Lambda}$ contains the squares of the component's eigen-frequencies on its diagonal. Substituting Eq. (3.9) into Eq. (3.2) and pre-multiplying the resulting equation by the transpose of the transformation matrix from Eq. (3.9) yields

$$\begin{bmatrix} \mathbf{I} & \mathbf{0} \\ \mathbf{0} & \mathbf{M}^{cc} \end{bmatrix} \begin{Bmatrix} \ddot{\mathbf{z}} \\ \ddot{\boldsymbol{\delta}}^c \end{Bmatrix} + \begin{bmatrix} \boldsymbol{\Lambda} & \boldsymbol{\Psi}^T\mathbf{K}^{fc} \\ \mathbf{K}^{cf}\boldsymbol{\Psi} & \mathbf{K}^{cc} \end{bmatrix} \begin{Bmatrix} \mathbf{z} \\ \boldsymbol{\delta}^c \end{Bmatrix} = \begin{Bmatrix} \boldsymbol{\Psi}^T\mathbf{f}^f \\ \mathbf{f}^c \end{Bmatrix} \tag{3.12}$$

If the normal modes are split into a *k*ept and a *d*eleted set, then Eq. (3.12) can be rewritten as

$$\begin{bmatrix} \mathbf{I} & \mathbf{0} & \mathbf{0} \\ \mathbf{0} & \mathbf{I} & \mathbf{0} \\ \mathbf{0} & \mathbf{0} & \mathbf{M}^{cc} \end{bmatrix} \begin{Bmatrix} \ddot{\mathbf{z}}^{d} \\ \ddot{\mathbf{z}}^{k} \\ \ddot{\boldsymbol{\delta}}^{c} \end{Bmatrix} + \begin{bmatrix} \boldsymbol{\Lambda}^{d} & \mathbf{0} & \boldsymbol{\Psi}^{d^T}\mathbf{K}^{fc} \\ \mathbf{0} & \boldsymbol{\Lambda}^{k} & \boldsymbol{\Psi}^{k^T}\mathbf{K}^{fc} \\ \mathbf{K}^{cf}\boldsymbol{\Psi}^{d} & \mathbf{K}^{cf}\boldsymbol{\Psi}^{k} & \mathbf{K}^{cc} \end{bmatrix} \begin{Bmatrix} \mathbf{z}^{d} \\ \mathbf{z}^{k} \\ \boldsymbol{\delta}^{c} \end{Bmatrix} = \begin{Bmatrix} \boldsymbol{\Psi}^{d^T}\mathbf{f}^{f} \\ \boldsymbol{\Psi}^{k^T}\mathbf{f}^{f} \\ \mathbf{f}^{c} \end{Bmatrix} \tag{3.13}$$

The size of the problem can be reduced by eliminating the rows and columns associated with the deleted modes:

$$\begin{bmatrix} \mathbf{I} & \mathbf{0} \\ \mathbf{0} & \mathbf{M}^{cc} \end{bmatrix} \begin{Bmatrix} \ddot{\mathbf{z}}^{k} \\ \ddot{\boldsymbol{\delta}}^{c} \end{Bmatrix} + \begin{bmatrix} \boldsymbol{\Lambda}^{k} & \boldsymbol{\Psi}^{k^T}\mathbf{K}^{fc} \\ \mathbf{K}^{cf}\boldsymbol{\Psi}^{k} & \mathbf{K}^{cc} \end{bmatrix} \begin{Bmatrix} \mathbf{z}^{k} \\ \boldsymbol{\delta}^{c} \end{Bmatrix} = \begin{Bmatrix} \boldsymbol{\Psi}^{k^T}\mathbf{f}^{f} \\ \mathbf{f}^{c} \end{Bmatrix} \tag{3.14}$$

The condensed model in Eq. (3.14) provides good results as long as the contact nodes do not deflect; i.e. $\boldsymbol{\delta}^{c} = \mathbf{0}$. However, in a multibody setting, contact nodes can generally move. It can be shown that for moving contact nodes Eq. (3.14) will lead to large errors [82].

3.4 Component mode synthesis

The basic idea of the component mode synthesis method lies in the superposition of different types of modes in order to reduce the truncation error. Hurty [41] proposed to compose nodal displacement from three sets of modes:

1) Rigid body modes: For a body in three-space there are up to six modes if no external constraint exists.
2) Constraint modes: These modes are defined by the displacement of the connection points (contact nodes) in addition to displacements from the rigid body motion. For the contact nodes, there exist as many modes as degrees-of-freedom.

3) Fixed normal modes: These are normal vibration modes of the component with its boundaries (contact nodes) fixed. In general, there are a large number of these modes. Some of these modes can be eliminated in order to truncate the system.

Craig and Bampton [7] combined the rigid-body modes with the constraint modes, producing only two types of modes:

1) Constraint modes: These modes are defined by the total displacement of the connection points (contact nodes).
2) Fixed normal modes: These modes are the same as the normal modes in Hurty [41].

The latter method is usually referred to as the Craig-Bampton reduction method and is usually employed for reduced finite element models in multibody dynamics. Its essential idea is visualized in Figure 3-1 for a two-dimensional beam. The remaining of this section constructs the transformation matrix of reduction for the Craig-Bampton method and applies it to Eq. (3.2).

The fixed normal modes $\boldsymbol{\Psi}$ are obtained by solving the generalized eigen-value problem represented by Eq. (3.11). The constrained modes are the same as the static modes in the static condensation; i.e. $\boldsymbol{\Psi}_s$. By superimposing these two sets of modes, the nodal to modal transformation for all nodes can be obtained by

$$\begin{Bmatrix} \boldsymbol{\delta}^f \\ \boldsymbol{\delta}^c \end{Bmatrix} = \begin{bmatrix} \boldsymbol{\Psi} & \boldsymbol{\Psi}_s \\ \mathbf{0} & \mathbf{I} \end{bmatrix} \begin{Bmatrix} \mathbf{z} \\ \boldsymbol{\delta}^c \end{Bmatrix} \tag{3.15}$$

where $\mathbf{z}$ is a set of generalized coordinates that are related to the mode shapes. One can interpret these generalized coordinates as the mode shape amplification factors.

Applying the transformations defined by Eq. (3.15) to Eq. (3.2) and pre-multiplying the resulting equation by the transpose of the transformation matrix from Eq. (3.15) yields

$$\begin{bmatrix} \mathbf{I} & \boldsymbol{\Psi}^{kT}\mathbf{M}^{ff}\boldsymbol{\Psi}_s \\ \boldsymbol{\Psi}_s{}^{T}\mathbf{M}^{ff}\boldsymbol{\Psi}^{k} & \mathbf{M}^{cc}+\boldsymbol{\Psi}_s{}^{T}\mathbf{M}^{ff}\boldsymbol{\Psi}_s \end{bmatrix}\begin{Bmatrix} \ddot{\mathbf{z}}^{k} \\ \ddot{\boldsymbol{\delta}}^{c} \end{Bmatrix}+\begin{bmatrix} \boldsymbol{\Lambda} & \mathbf{0} \\ \mathbf{0} & \mathbf{K}^{cc}+\mathbf{K}^{cf}\boldsymbol{\Psi}_s \end{bmatrix}\begin{Bmatrix} \mathbf{z}^{k} \\ \boldsymbol{\delta}^{c} \end{Bmatrix}=\begin{Bmatrix} \boldsymbol{\Psi}^{kT}\mathbf{f}^{f} \\ \mathbf{f}^{c}+\boldsymbol{\Psi}_s{}^{T}\mathbf{f}^{f} \end{Bmatrix} \quad (3.16)$$

where the normal modes are split into a *k*ept-set and a *d*eleted-set, and the rows and columns associated with the deleted modes are eliminated. It should be noted that no modification has been made to the contact nodes. Therefore these nodes remain compatible with all other bodies in the system. Furthermore, the generalized coordinates describing the interior modes of the structure are unique to this structure and, hence, do not require compatibility with other components in a multibody set.

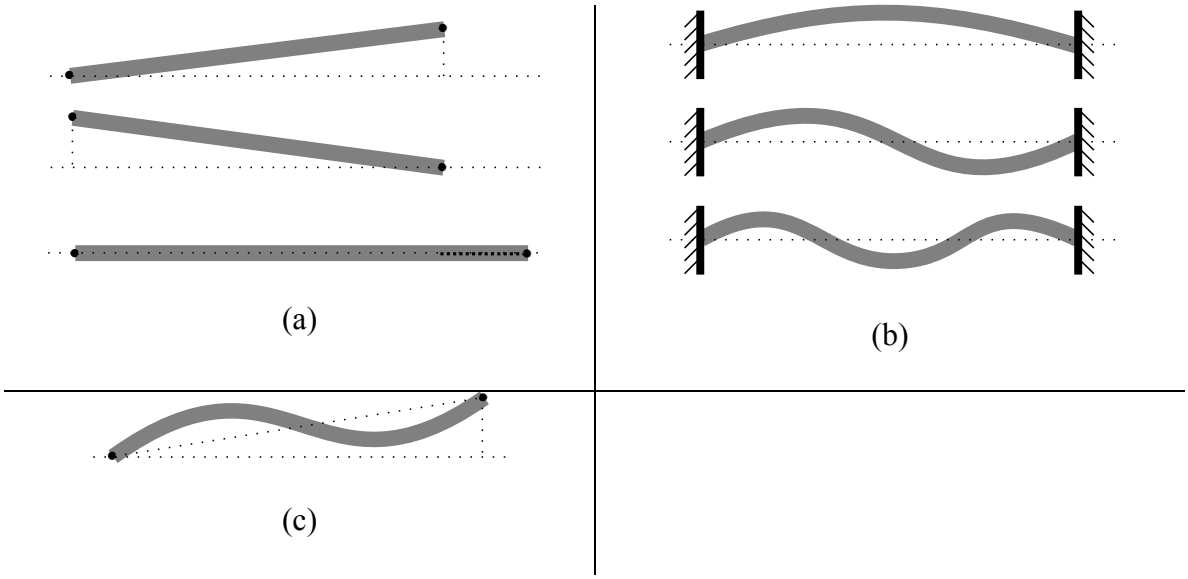

Figure 3-1: A two dimensional beam is represented with: (a) first three functions of the deflection of the boundary nodes (constraint modes); (b) first three fixed normal mode shapes; (c) superposition of first mode from (a) and second mode from (b) (CMS).

3.5 Mode condensation

In component mode synthesis the transformation matrix of reduction is intuitively created by superimposing different types of modes in order to improve the quality of modal reduction. While these reduction methods provide decent results, no physical explanations were given that justify the various combinations. For that reason, Nikravesh [40] developed a separate reduction method to properly condense a deformable body that is restrained by joints and forces. His approach is referred to as *mode condensation* and starts with the classical modal reduction from Section 3.3. He assumes that the inertia and external forces associated with the deleted modes are relocated to the boundary nodes, which is similar to a statement for static condensation. Alternatively, it can be assumed that the potential energy with respect to the deleted modes is minimal [42]. In this section, the conclusion of the second assumption is presented.

The potential (strain) energy of the body can be expressed as

$$PE = \frac{1}{2}\boldsymbol{\delta}^T \mathbf{K} \boldsymbol{\delta} = \frac{1}{2} \begin{Bmatrix} \mathbf{z}^d \\ \mathbf{z}^k \\ \boldsymbol{\delta}^c \end{Bmatrix}^T \begin{bmatrix} \boldsymbol{\Lambda}^d & \mathbf{0} & \boldsymbol{\Psi}^{dT} \mathbf{K}^{fc} \\ \mathbf{0} & \boldsymbol{\Lambda}^k & \boldsymbol{\Psi}^{kT} \mathbf{K}^{fc} \\ \mathbf{K}^{cf} \boldsymbol{\Psi}^d & \mathbf{K}^{cf} \boldsymbol{\Psi}^k & \mathbf{K}^{cc} \end{bmatrix} \begin{Bmatrix} \mathbf{z}^d \\ \mathbf{z}^k \\ \boldsymbol{\delta}^c \end{Bmatrix} \tag{3.17}$$

for which Eq. (3.9) has been used. Setting the partial derivatives of *PE* with respect to $\mathbf{z}^d$ to zero yields

$$\frac{\partial PE}{\partial \mathbf{z}^d} = \begin{Bmatrix} \mathbf{z}^d \\ \boldsymbol{\delta}^c \end{Bmatrix}^T \begin{bmatrix} \boldsymbol{\Lambda}^d \\ \mathbf{K}^{cf} \boldsymbol{\Psi}^d \end{bmatrix} = \mathbf{z}^{dT} \boldsymbol{\Lambda}^d + \boldsymbol{\delta}^{cT} \mathbf{K}^{cf} \boldsymbol{\Psi}^d = \mathbf{0} \tag{3.18}$$

or

$$\mathbf{z}^d = \left(-\boldsymbol{\Lambda}^{d^{-1}} \boldsymbol{\Psi}^{dT} \mathbf{K}^{fc} \right) \boldsymbol{\delta}^c = \boldsymbol{\Theta} \boldsymbol{\delta}^c \tag{3.19}$$

where

$$\boldsymbol{\Theta} = \left(-\boldsymbol{\Lambda}^{d^{-1}} \boldsymbol{\Psi}^{d^T} \mathbf{K}^{fc} \right) \tag{3.20}$$

The following transformation can be established

$$\begin{Bmatrix} \mathbf{z}^d \\ \mathbf{z}^k \\ \boldsymbol{\delta}^c \end{Bmatrix} = \begin{bmatrix} \mathbf{0} & \boldsymbol{\Theta} \\ \mathbf{I} & \mathbf{0} \\ \mathbf{0} & \mathbf{I} \end{bmatrix} \begin{Bmatrix} \mathbf{z}^k \\ \boldsymbol{\delta}^c \end{Bmatrix} \tag{3.21}$$

Substituting Eq. (3.21) into Eq. (3.13) and pre-multiplying the resulting equation with the transpose of the transformation matrix yields

$$\begin{bmatrix} \mathbf{I} & \mathbf{0} \\ \mathbf{0} & \mathbf{M}_m \end{bmatrix} \begin{Bmatrix} \ddot{\mathbf{z}}^k \\ \ddot{\boldsymbol{\delta}}^c \end{Bmatrix} + \begin{bmatrix} \boldsymbol{\Lambda}^k & \boldsymbol{\Psi}^{k^T} \mathbf{K}^{fc} \\ \mathbf{K}^{cf} \boldsymbol{\Psi}^k & \mathbf{K}_m \end{bmatrix} \begin{Bmatrix} \mathbf{z}^k \\ \boldsymbol{\delta}^c \end{Bmatrix} = \begin{Bmatrix} \boldsymbol{\Psi}^{k^T} \mathbf{f}^f \\ \mathbf{f}^c + \boldsymbol{\Theta}^T \boldsymbol{\Psi}^{d^T} \mathbf{f}^f \end{Bmatrix} \tag{3.22}$$

where

$$\begin{aligned} \mathbf{M}_m &= \mathbf{M}^{cc} + \boldsymbol{\Theta}^T \boldsymbol{\Theta} \\ \mathbf{K}_m &= \mathbf{K}^{cc} + \mathbf{K}^{cf} \boldsymbol{\Psi}^d \end{aligned} \tag{3.23}$$

with $\boldsymbol{\Theta}^T \boldsymbol{\Lambda}^d \boldsymbol{\Theta} = -\boldsymbol{\Theta}^T \boldsymbol{\Psi}^{d^T} \mathbf{K}^{fc}$. It turns out, that this method provides results that are equivalent to the one from the Craig-Bampton reduction. Furthermore, it should be noted that in Eq. (3.22) the coupling between the generalized coordinate $\mathbf{z}^k$ and the deflections of the contact nodes $\boldsymbol{\delta}^c$ occurs in the stiffness matrix, in contrast to Eq. (3.16), where the coupling occurs in the mass matrix. This characteristic can provide a numerical advantage; however, it is only true if the original mass matrix is lumped.

3.6 Discussion

Several reduction methods were presented in this chapter that can reduce the number of degrees-of-freedom of a deformable body. While static condensation and

modal truncation are well known condensation methods, they are not suitable for multibody purposes. In static condensation the eigen-properties of the system are altered, and modal truncation is only valid for so called fixed boundary conditions. Methods known as component mode synthesis address these issues by superimposing different types of modes. While these methods are intuitively developed, they are adequate for multibody purposes. One of these methods is the Craig-Bampton reduction method, which is usually employed in deformable multibody dynamics. Mode condensation is a more recently developed method for condensing deformable bodies that are constrained by joints and forces. In contrast to CMS, it derives the condensation formula directly from the equations of motion.

The following remarks are valid for all reduction methods that are presented in this chapter: If the stiffness matrix of the original structure has a rank deficiency of six due to rigid-body DoF, then this rank deficiency is carried over to the new modified stiffness matrix. The rigid body DoF can easily be eliminated from the condensed stiffness matrix, if it is desired; i.e., the whole structure can be constrained to the ground at its contact nodes.

Up to this point, we have focused on two problems that are frequently associated with deformable bodies: large rigid-body rotation, and large number of degrees-of-freedom. Both problems were addressed extensively in the past and well documented in many publications. A short summary of the most popular outcomes were presented in this and the previous chapter. However, previous work has not addressed the issue of

changing contact nodes for deformable bodies. This gap will be filled in the following chapters.

4. TRAVELING AND VARIABLE SIZE CONTACT AREA

In the previous chapter, different truncation methods for deformable bodies that are represented by finite element models were discussed. The adequacy of a truncation technique depends on the boundary conditions of the deformable body. The two boundary conditions that are discussed in the previous chapter are fixed and moving boundaries. In both cases it is assumed that the boundaries do not change in their contact size or travel over the surface of the deformable body; i.e., the set of nodes in contact is fixed. This chapter introduces two other types of boundary condition. In the first condition the size of the contact area, and in turn the number of contact nodes, is allowed to change. An example for this boundary condition can be found in a belt drive, where the belt can lift off partially from the pulleys due to vibration. In the second condition the contact area travels along the surface of a deformable body; i.e., any node on the surface can potentially become in contact with another body. While, this problem can easily be dealt with in a full finite element model, other problems arise if the finite element model is condensed. For example, if a belt rotates around two pulleys, then all nodes of the belt have to be considered as contact nodes, since each node is a potential candidate to become in contact with the pulleys. However, selecting all nodes as contact nodes prevents the belt model to be truncated at all. Therefore, other procedures have to be found to deal with this problem.

This chapter focuses on the problem of variable size contact area first, and shows how this problem can be addressed. Then, it introduces the concept of *flowing material*

that solves the issue of traveling contact area. The concept is based on an orientation invariant characteristic that might be present in some specific deformable bodies. Even though a general discussion for both types of boundary condition can be given, a belt drive example is discussed instead in order to provide the reader with a better insight into the complexity of the problems.

4.1 A slow rotating belt drive

Belt drives have always been of major interest to mechanical engineers. Their simple structure has allowed them to be used in a broad range of applications, such as home appliances, car engines, and conveyor systems. However, their disadvantage lies in their strong exposure to drive-train vibration and resonance. Therefore, researches have been investigating belt vibration for many years [46]. In the early studies of belt drive vibration, belt drive models were highly simplified due to the lack of computer aided calculations. The belt was not investigated as a whole, but instead only the transversal vibrations between the pulleys were investigated [44, 46]. In this case, the belt was modeled as a string or beam depending on the particular combination of parameters such as bending rigidity, initial tension and span length [46]. Furthermore, if the rotational speed of the belt drive was slow compared to the belt rigidity, such as in some conveyor belt systems, then the belt was represented by a stationary (non-moving) string or beam. Even though these models have become out-dated, they still serve as a good basis for understanding the problem of resizable boundary conditions.

Let us consider a belt drive that consists of two pulleys and a tightly stretched belt, as shown in Figure 4-1. For the sake of simplicity, it is assumed that the belt drive does not rotate. If the belt vibrates due to external forces, then the belt can partially lift off the pulleys (see image enlargement in Figure 4-1). That leads to a change in the effective length of the free vibrating belt section. In this case, representing the belt as a string or beam with fixed boundaries is no longer adequate. Instead, the belt must be represented by a string or beam that is partially wrapped around the pulleys. The difficulty here lies in the contact area between the string/beam and the pulleys that changes in size as the string/beam vibrates.

The following sub-sections introduce a belt model that is represented as a string with resizable contact area. In doing so, the equations of motions for a string are derived first. Then these equations are extended with three different boundary conditions: fixed boundaries, moving boundaries, and boundaries with variable size contact area, also referred to as variable size boundaries. Fixed boundaries correspond to the case where the belt is fixed to the pulleys; i.e., the effective length of the belt is kept constant. Moving boundaries cannot be related to the belt system in our example, but are important for the derivation of the variable size boundary conditions. The variable size boundaries correspond to the case, where the belt can partially lift off from the pulleys.

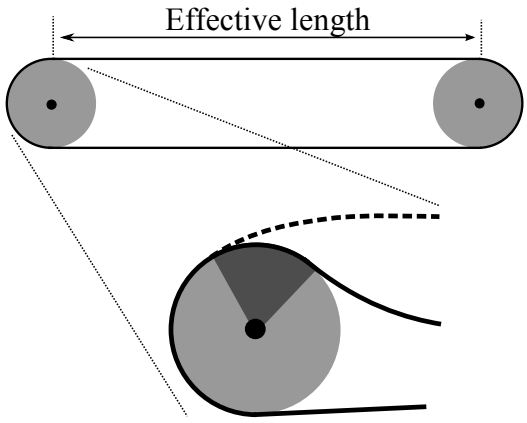

Figure 4-1: A belt drive with variable size contact area (dark gray).

4.1.1 Equations of motion for a string

Consider a thin string that is horizontally stretched. For small vibration amplitudes of the string, the motion can be approximated to be entirely vertical; i.e., the deflection is defined as $u = u(x,t)$ with x defining the position along the string and t being the time, as shown in Figure 4-2. Furthermore, the string is considered to have uniform density ρ_0 and cross-sectional area A_0. Also, the string is perfectly flexible; i.e., it offers no resistance to bending. For small vibration amplitudes, the stretching of the string is nearly the same as for the unperturbed highly stretched horizontal string. Thus, the tension in the string may be approximated by a constant T_0. The string is assumed to be divided into several finite elements, where each element consists of two nodes. Without loss of generality, only 1 deflection degree-of-freedom for each node, in vertical direction, is considered. The mass and stiffness matrices for the string are defined as

$$\mathbf{M} = \frac{\rho_0 A_0 L}{(n+1)}\mathbf{I}, \quad \mathbf{K} = \frac{T_0(n+1)}{L}\begin{bmatrix} 1 & -1 & 0 & \cdot \\ -1 & 2 & -1 & \cdot \\ 0 & -1 & 2 & \cdot \\ \cdot & \cdot & \cdot & \cdot \end{bmatrix} \tag{4.1}$$

where L is the length of the string between the boundaries, and $\mathbf{M}$ is diagonal. To include boundary conditions, the nodes that describe the string are partitioned into two groups: those that are free, designated as f-nodes (colored in black in Figure 4-2 - Figure 4-4); and those that are in contact, designated as c-nodes (colored in gray). If the vertical deflections of the nodes are defined by an array $\mathbf{u}$, the finite element equations of motion for the string can be written as

$$\begin{bmatrix} \mathbf{M}^{ff} & \mathbf{0} \\ \mathbf{0} & \mathbf{M}^{cc} \end{bmatrix} \begin{Bmatrix} \ddot{\mathbf{u}}^{f} \\ \ddot{\mathbf{u}}^{c} \end{Bmatrix} = \begin{Bmatrix} \mathbf{g}^{f} \\ \mathbf{g}^{c} \end{Bmatrix} \tag{4.2}$$

where

$$\begin{Bmatrix} \mathbf{g}^{f} \\ \mathbf{g}^{c} \end{Bmatrix} = \begin{Bmatrix} \mathbf{f}^{f} \\ \mathbf{f}^{c} \end{Bmatrix} - \begin{Bmatrix} \mathbf{K}^{ff} & \mathbf{K}^{fc} \\ \mathbf{K}^{cf} & \mathbf{K}^{cc} \end{Bmatrix} \begin{Bmatrix} \mathbf{u}^{f} \\ \mathbf{u}^{c} \end{Bmatrix} \tag{4.3}$$

The array $\mathbf{f}$ contains the external forces that may act on the system. For reasons of clarity and readability, damping terms are excluded from the equations, but can be easily included in all equations. In the following section Eq.(4.3) will be used to describe the motion of a string in three different scenarios.

4.1.2 Fixed, moving, and variable size boundaries

In the first scenario the string is clamped at both ends, as shown in Figure 4-2. Once the system is excited, it performs an oscillatory motion about its equilibrium between the boundaries. Since the contact nodes are at the fixed boundaries, they do not move; i.e., $\mathbf{u}^{c} = \mathbf{0}$. The equations of motions can be simplified to

$$\mathbf{M}^{ff}\ddot{\mathbf{u}}^{f} + \mathbf{K}^{ff}\mathbf{u}^{f} = \mathbf{f}^{f} \tag{4.4}$$

A transformation from nodal to modal coordinates can be obtained by using

$$\mathbf{u}^f = \boldsymbol{\Psi}\mathbf{z} \tag{4.5}$$

where $\boldsymbol{\Psi}$ is the matrix of normal deformation mode shapes normalized to $\mathbf{M}^{ff}$, and $\mathbf{z}$ is a set of generalized coordinates. Then, the equations of motion for the string take the form

$$\mathbf{M}^{ff}\boldsymbol{\Psi}\ddot{\mathbf{z}} + \mathbf{K}^{ff}\boldsymbol{\Psi}\mathbf{z} = \mathbf{f}^f \tag{4.6}$$

Pre-multiplying these equations by $\boldsymbol{\Psi}^T$ leads to

$$\ddot{\mathbf{z}} + \boldsymbol{\Lambda}\mathbf{z} = \boldsymbol{\Psi}^T\mathbf{f}^f \tag{4.7}$$

with $\boldsymbol{\Psi}^T\mathbf{M}^{ff}\boldsymbol{\Psi} = \mathbf{I}$ and $\boldsymbol{\Psi}^T\mathbf{K}^{ff}\boldsymbol{\Psi} = \boldsymbol{\Lambda}$, where $\boldsymbol{\Lambda}$ is a diagonal matrix that includes the squares of the systems natural frequencies. Note that Eq. (4.7) represents a system of decoupled equations. This offers the opportunity to reduce the system in its DoF by eliminating the equations associated with the higher frequencies.

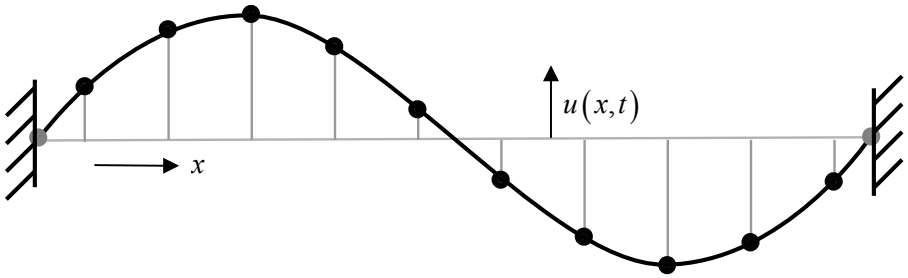

Figure 4-2: String clamped at both ends.

In the second scenario the boundaries of the string are allowed to move; i.e., $\mathbf{u}^c \neq \mathbf{0}$, as shown in Figure 4-3. In this case the transformation from nodal to modal coordinates is expressed as

$$\begin{Bmatrix} \mathbf{u}^f \\ \mathbf{u}^c \end{Bmatrix} = \begin{bmatrix} \boldsymbol{\Psi} & \boldsymbol{\Psi}_s \\ \mathbf{0} & \mathbf{I} \end{bmatrix} \begin{Bmatrix} \mathbf{z} \\ \mathbf{u}^c \end{Bmatrix} \tag{4.8}$$

where Ψ_s is the matrix of static mode shapes. The transformation matrix in Eq.(4.8) is based on the Craig-Bampton reduction method. Substituting Eq. (4.8) in Eq. (4.2) and pre-multiplying the first row with the transpose of Ψ yields

$$\begin{bmatrix} \mathbf{I} & \Psi^T \mathbf{M}^{ff} \Psi_s \\ \mathbf{0} & \mathbf{M}^{cc} \end{bmatrix} \begin{Bmatrix} \ddot{\mathbf{z}}^f \\ \ddot{\mathbf{u}}^c \end{Bmatrix} = \begin{Bmatrix} \Psi^T \mathbf{g}^f \\ \mathbf{g}^c \end{Bmatrix} \tag{4.9}$$

In this form the string model can be truncated by eliminating some columns of Ψ.

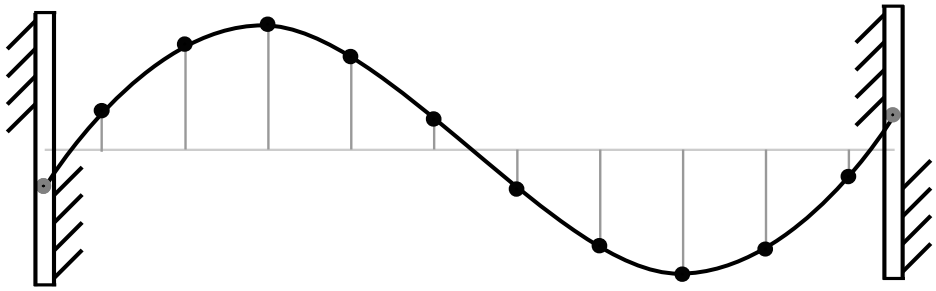

Figure 4-3: A string with moving ends

In the third scenario the string is partially wrapped over two pulleys, as shown in Figure 4-4. In contrast to the preceding cases, the size of the contact area changes here; i.e., more than two nodes can be in contact. The effective undeformed length of the portion that is free and the portions in contact with the pulleys are not constant. If the string lifts off partially from the pulley due to vibration, the length of the free portion increases and that of the constrained portion decreases. Therefore, the sets of contact nodes and free nodes need to be redefined as the string lifts off from and reattaches to the pulleys. In order to circumvent the difficulties associated with readjusting the number of nodes that are free or in contact, we consider the number of contact nodes and free nodes to remain constant. The number of nodes that we consider as contact or "c" nodes would represent the maximum number of nodes that could become in contact; i.e., some of the

"c" nodes may not be actually in contact at a given instant. The equations of motion for the string in the third scenario can be obtained by extending Eq. (4.2) with the additional contact conditions:

$$\begin{bmatrix} \mathbf{M}^{ff} & \mathbf{0} & \mathbf{0} \\ \mathbf{0} & \mathbf{M}^{cc} & -\mathbf{D}^T \\ \mathbf{0} & \mathbf{D} & \mathbf{0} \end{bmatrix} \begin{Bmatrix} \ddot{\mathbf{u}}^f \\ \ddot{\mathbf{u}}^c \\ \boldsymbol{\lambda} \end{Bmatrix} = \begin{Bmatrix} \mathbf{g}^f \\ \mathbf{g}^c \\ \boldsymbol{\gamma} \end{Bmatrix} \tag{4.10}$$

where $\mathbf{D}$ is the Jacobian matrix of the constraints. In this equation the array $\mathbf{u}^c$ contains the deflection of all the nodes that are defined as contact nodes. It should be noted that not all of the contact nodes need to be constrained — only those that are in contact with the pulleys. As the string vibrates, we only need to adjust the entries of the Jacobian matrix to apply to those nodes that are actually in contact. A transformation from nodal to modal coordinates for the free nodes can be obtained again by substituting Eq. (4.8) in Eq. (4.10) and pre-multiplying the first row with the transpose of $\boldsymbol{\Psi}$:

$$\begin{bmatrix} \mathbf{I} & \boldsymbol{\Psi}^T \mathbf{M}^{ff} \boldsymbol{\Psi}_s & \mathbf{0} \\ \mathbf{0} & \mathbf{M}^{cc} & -\mathbf{D}^T \\ \mathbf{0} & \mathbf{D} & \mathbf{0} \end{bmatrix} \begin{Bmatrix} \mathbf{z} \\ \ddot{\mathbf{u}}^c \\ \boldsymbol{\lambda} \end{Bmatrix} = \begin{Bmatrix} \boldsymbol{\Psi}^T \mathbf{g}^f \\ \mathbf{g}^c \\ \boldsymbol{\gamma} \end{Bmatrix} \tag{4.11}$$

In this form the string model can be truncated by eliminating some columns of $\boldsymbol{\Psi}$. Note that with or without truncation, the contact conditions on the contact nodes are always fully enforced.

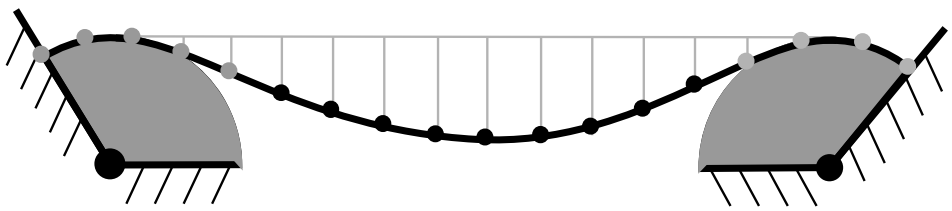

Figure 4-4: A string wrapped around pulleys at both ends.

4.2 A fast rotating belt drive model

The primary discussion represents the belt as a string or a beam that focus only on the transversal vibrations between the pulleys. If the rotational speed of the belt is slow so that it does not affect the transversal vibration behavior of the belt, then the belt can be represented by a stationary (non-moving) string or beam. However, such models are not adequate for fast rotating belt drives, where the belt needs to be represented by a *traveling* string or beam. Such a model can be visualized by considering a thin string of infinite length, where guiding rollers are attached at two points along the string, as shown in Figure 4-5. The guiding rollers represent the boundaries (pulleys) of the string (belt). The string vibrates only between these two boundaries that are fixed in space. Furthermore, the string is being pulled from one end in horizontal direction. It may not be immediately obvious, but the behavior of this vibrating string can be significantly different from a non-traveling string, especially for high speeds.

Analytical models for traveling strings are already well known, but representing a traveling string through a finite element approach is fairly new. A finite element model allows us to handle different boundary conditions, as it is shown in Section 4.1. However, in the case of a traveling string, we are also confronted with two other issues. The first problem deals with the fact that an infinite long string cannot be represented as a FE model. Therefore, the string needs to be finite in its length. The second problem lies in the contact definition. Due to the horizontal motion of the string, the contact between the string and the rollers travels along the string, which causes some nodes to leave and others to enter the contact area, as shown in Figure 4-5. This problem could be addressed

by defining all of the nodes as possible contact nodes. Obviously, this approach is not practical since a very long string may contain hundreds of nodes. Instead, one can make a helpful observation in this example if the distance between the boundaries remains a constant and the tension in the string do not change. In that case the stiffness and the total mass in the string between the boundaries remain constant, even if the string is pulled in one direction. When the nodes travel along the horizontal axis, and if we introduce a new set of nodes in the vacated spaces of the old nodes, the same mass and stiffness matrices can be used. Consequently, the same mode shapes can be applied to the new nodes. In other words, the mass and stiffness matrices, and the mode shapes can remain as a non-traveling frame, but the mass points *flow* through them. This idea solves both above mentioned problems. The string can be of infinite length again, since it is sufficient to mesh the string between the rollers only, and the nodes in contact remain in contact; i.e., free nodes never become in contact with the rollers and, hence, their modal coordinates can be truncated. This idea is referred to as the *flowing material*.

In the following sub-sections the concept of *flowing material* is shown on a traveling string with fixed boundaries. Additionally an analytical solution for the same traveling string model is given and compared to the numerical approach. It will be shown that both approaches provide the same results for the traveling string. Then the concept of *flowing material* is applied to a traveling string with resizable boundaries.

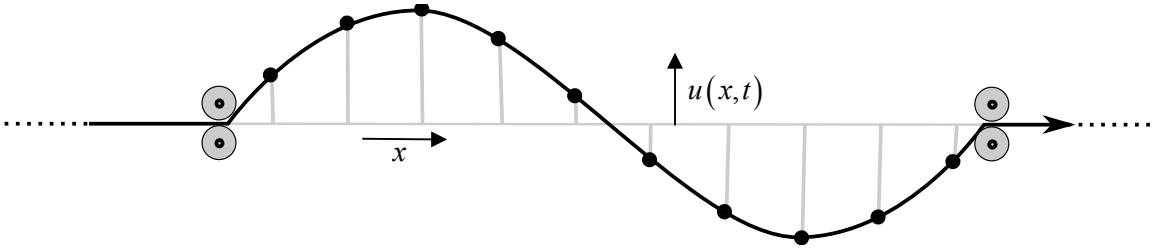

Figure 4-5: A traveling string with fixed boundaries.

4.2.1 Fixed boundaries

The equations of motions in nodal coordinates for a non-moving string with fixed ends are repeated here:

$$\mathbf{M}\ddot{\mathbf{u}} + \mathbf{K}\mathbf{u} = \mathbf{f} \tag{4.12}$$

where, for convenience, the superscript *f* is omitted. Since the string is pulled through the rollers, some kind of mass flow needs to be introduced in this equation. This mass flow can be implemented using the material derivative

$$\frac{d}{dt} = \frac{\partial}{\partial t} + \dot{x}\frac{\partial}{\partial x} \tag{4.13}$$

The left-hand side of Eq. (4.13) represents the total time derivative in the Lagrangian space. The first term on the right-hand side is the time derivative in the Eulerian space, x defines the position along the string, and $\dot{x}$ is the speed of the mass flow, or in this simple example the speed of the string. Applying Eq. (4.13) on $\mathbf{u}$ leads to

$$\dot{\mathbf{u}} = \frac{d\mathbf{u}}{dt} = \frac{\partial \mathbf{u}}{\partial t} + \dot{x}\frac{\partial \mathbf{u}}{\partial x} \tag{4.14}$$

Applying Eq. (4.13) to Eq. (4.14) gives the second derivative

$$\ddot{\mathbf{u}} = \frac{d^2\mathbf{u}}{dt^2} = \frac{\partial^2 \mathbf{u}}{\partial t^2} + \ddot{x}\frac{\partial \mathbf{u}}{\partial x} + \dot{x}\frac{\partial^2 \mathbf{u}}{\partial x \partial t} + \dot{x}\frac{\partial^2 \mathbf{u}}{\partial t \partial x} + \dot{x}^2\frac{\partial^2 \mathbf{u}}{\partial x^2} \tag{4.15}$$

with $\ddot{x}$ being the acceleration of the string. However, substituting Eq. (4.14) and (4.15) into Eq. (4.12) will not be very helpful, since the partial derivatives $\partial\mathbf{u}/\partial x$ and $\partial^2\mathbf{u}/\partial x^2$ need to be determined at each time step. Furthermore, this process can be cumbersome and time consuming, especially when the system includes large number of degrees-of-freedom. On the other hand, if the distance between the boundaries (rollers) stays constant and the tension in the string does not change, then the normal deformation mode shapes $\boldsymbol{\Psi}$ of the string would be independent of time and only a function of the position x. For that reason a nodal to modal coordinate transformation is preferred again:

$$\mathbf{u} = \boldsymbol{\Psi}\mathbf{z} \tag{4.16}$$

Here the amplifications $\mathbf{z}$ of the modes undoubtedly vary with time, but due to their physical meaning they are independent of any spatial direction. With that in mind, Eq. (4.13) can be applied on Eq. (4.16), which leads to the first derivative as

$$\dot{\mathbf{u}} = \frac{d\mathbf{u}}{dt} = \boldsymbol{\Psi}\dot{\mathbf{z}} + \dot{x}\boldsymbol{\Psi}_{,x}\mathbf{z} \tag{4.17}$$

Here, $\boldsymbol{\Psi}_{,x}$ includes the partial derivatives of the mode shapes with respect to x. Applying Eq. (4.13) on Eq. (4.17) gives the second derivative

$$\ddot{\mathbf{u}} = \frac{d^2\mathbf{u}}{dt^2} = \boldsymbol{\Psi}\ddot{\mathbf{z}} + \ddot{x}\boldsymbol{\Psi}_{,x}\mathbf{z} + 2\dot{x}\boldsymbol{\Psi}_{,x}\dot{\mathbf{z}} + \dot{x}^2\boldsymbol{\Psi}_{,xx}\mathbf{z} \tag{4.18}$$

with $\boldsymbol{\Psi}_{,xx}$ including the second partial derivative with respect to x. Substituting both equations in Eq. (4.12) reformulates the equation of motion of the string to

$$\mathbf{M}\boldsymbol{\Psi}\ddot{\mathbf{z}} + 2\dot{x}\mathbf{M}\boldsymbol{\Psi}_{,x}\dot{\mathbf{z}} + \left(\ddot{x}\mathbf{M}\boldsymbol{\Psi}_{,x} + \dot{x}^2\mathbf{M}\boldsymbol{\Psi}_{,xx} + \mathbf{K}\boldsymbol{\Psi}\right)\mathbf{z} = \mathbf{f} \tag{4.19}$$

In this equation $\boldsymbol{\Psi}_{,x}$ and $\boldsymbol{\Psi}_{,xx}$ are constant matrices and can be calculated ahead of time. Here, the integration variable is solely $\mathbf{z}$. An additional advantage can be obtained if Eq. (4.19) is pre-multiplied by the transpose of the mode shapes:

$$\boldsymbol{\Psi}^T\mathbf{M}\boldsymbol{\Psi}\ddot{\mathbf{z}} + 2\dot{x}\boldsymbol{\Psi}^T\mathbf{M}\boldsymbol{\Psi}_{,x}\dot{\mathbf{z}} + \left(\ddot{x}\boldsymbol{\Psi}^T\mathbf{M}\boldsymbol{\Psi}_{,x} + \dot{x}^2\boldsymbol{\Psi}^T\mathbf{M}\boldsymbol{\Psi}_{,xx} + \boldsymbol{\Psi}^T\mathbf{K}\boldsymbol{\Psi}\right)\mathbf{z} = \boldsymbol{\Psi}^T\mathbf{f} \tag{4.20}$$

with $\boldsymbol{\Psi}^T\mathbf{M}\boldsymbol{\Psi} = \mathbf{I}$ and $\boldsymbol{\Psi}^T\mathbf{K}\boldsymbol{\Psi} = \boldsymbol{\Lambda}$. By eliminating some columns of $\boldsymbol{\Psi}$, the system can be reduced in its size. Note that Eq. (4.20) is a set of dependent equations. Only for $\dot{x} = \ddot{x} = 0$ is the independency of the equations reestablished and Eq. (4.20) becomes identical to Eq.(4.7). Equation (4.20) represents the string model with the new concept of *flowing material*.

For the simple string example, $\boldsymbol{\Psi}_{,x}$ and $\boldsymbol{\Psi}_{,xx}$ can be obtained analytically. However, for complex systems with elements that include several degrees-of-freedom for each node, obtaining analytical solutions for the mode shape derivatives can be cumbersome or sometimes even impossible. For that reason numerical approaches, such as finite differences, can be used. A more detailed discussion on the mode shape derivatives is given in Appendix A.

It is worthwhile to mention that $\boldsymbol{\Psi}^T\mathbf{M}\boldsymbol{\Psi}\ddot{\mathbf{z}}$ is an inertial term that is purely in Eulerian space, $2\dot{x}\boldsymbol{\Psi}^T\mathbf{M}\boldsymbol{\Psi}_{,x}\dot{\mathbf{z}}$ represents Coriolis inertia forces, and $\dot{x}^2\boldsymbol{\Psi}^T\mathbf{M}\boldsymbol{\Psi}_{,xx}\mathbf{z}$ contains centrifugal forces. A good understanding of their effect on the overall system can be obtained by comparing them to the analytical solution of a moving string, which is done in the following sections. Here, it should be noted that for a certain axial velocity, the centrifugal forces may exceed the elastic forces, causing the equilibrium position to lose

stability; i.e., resulting in a pitchfork bifurcation. The pattern of equilibria compares to that of Euler column buckling [69].

4.2.2 Fixed boundaries (Analytical approach)

The equation of motion for the non-moving string, but as a continuous model, with fixed ends can be represented by the differential equation

$$\frac{\partial^2 u}{\partial t^2} - c^2 \frac{\partial^2 u}{\partial x^2} = 0 \tag{4.21}$$

where $c^2 = T_0 / (A_0 \rho_0)$. The boundary and initial conditions are

$$\begin{aligned} &\text{BC}: \quad u(0,t) = 0, \quad u(L,t) = 0 \\ &\text{IC}: \quad u(x,0) = f(x), \quad \frac{\partial u(x,0)}{\partial t} = g(x) \end{aligned} \tag{4.22}$$

where L is the length of the string between the boundaries. Equation (4.21) is the continuous representation of Eq. (4.12). If the string is considered to move axially with a constant speed v, as shown in Figure 4-5, then Eq. (4.21) extends to

$$\frac{\partial^2 u}{\partial t^2} + 2v \frac{\partial^2 u}{\partial x \partial t} + \left(v^2 - c^2\right) \frac{\partial^2 u}{\partial x^2} = 0 \tag{4.23}$$

with the same boundary and initial conditions as in Eq. (4.22). The method of eigenfunction expansion can be used to solve these equations:

$$u(x,t) = \sum_{n=1}^{\infty} a_n(t) \phi_n(x) \tag{4.24}$$

with $\phi_n(x) = \sin\left(n\pi x / L\right)$ being the eigenfunctions and L the constant distance between the boundaries. This expansion is analogous to Eq. (4.16). Since $u = u(x,t)$ solves the same

homogeneous boundary conditions as $\phi_n(x)$ does, the necessary term by term differentiation for Eq. (4.24) can be justified; i.e.,

$$\begin{aligned} u_{tt} &= \sum_{n=1}^{\infty} \ddot{a}_n(t)\phi_n(x) \qquad \text{a)} \\ u_{xt} &= \sum_{n=1}^{\infty} \dot{a}_n(t)\phi_n'(x) \qquad \text{b)} \\ u_{xx} &= \sum_{n=1}^{\infty} a_n(t)\phi_n''(x) \qquad \text{c)} \end{aligned} \tag{4.25}$$

Using Eq. (4.25) (a)-(c) in Eq. (4.23), multiplying with ϕ_m, and integrating over the domain gives the continuous representation of Eq. (4.20) with constant speed:

$$\sum_{n=1}^{\infty} \ddot{a}_n \int_0^L \phi_m \phi_n dx + 2v\dot{a}_n \int_0^L \phi_m \phi_n' dx + \left(v^2 - c^2\right) a_n \int_0^L \phi_m \phi_n'' dx = 0 \tag{4.26}$$

Or in matrix form we have

$$\ddot{\mathbf{a}}_n + \mathbf{A}\dot{\mathbf{a}}_n + \mathbf{B}\mathbf{a}_n = \mathbf{0} \tag{4.27}$$

with

$$\begin{aligned} \mathbf{A}_{mn} &= \begin{cases} \dfrac{2vn}{L}\left[\dfrac{1-\cos\left((m+n)\pi\right)}{(m+n)} + \dfrac{1-\cos\left((m-n)\pi\right)}{(m-n)}\right], & \text{for } m \neq n \\ 0, & \text{for } m = n \end{cases} \\ \mathbf{B}_{mn} &= \begin{cases} \left(c^2 - v^2\right)\left(\dfrac{\pi n}{L}\right)^2, & \text{for } m = n \\ 0, & \text{for } m \neq n \end{cases} \end{aligned} \tag{4.28}$$

4.2.3 Comparison between numerical and analytical approach

The equation of motion for an axially moving string; i.e., Eq. (4.27), can be transformed into state space form:

$$\mathbf{X}=\begin{bmatrix}\mathbf{0} & \mathbf{I}\\ -\mathbf{B} & -\mathbf{A}\end{bmatrix},\quad \mathbf{q}=\begin{Bmatrix}\mathbf{a}_n\\ \dot{\mathbf{a}}_n\end{Bmatrix} \tag{4.29}$$

Then the equations are solved to find

$$\dot{\mathbf{q}}(t)=\mathbf{L}e^{\mathbf{T}t}\mathbf{L}^{-1}\mathbf{q}(0) \tag{4.30}$$

where $\mathbf{L}$ and $\mathbf{T}$ are obtained from the eigenvalue problem $\mathbf{XL}=\mathbf{LT}$. Note that the diagonal terms of $\mathbf{B}$ provide the squares of the natural frequencies of the axially moving string, $\omega_n=\sqrt{\left(c^2-v^2\right)}\left(\frac{\pi n}{L}\right)$. The same natural frequencies can be found in the discrete model by evaluating $\mathbf{\Omega}_{discrete}=\left(\mathbf{\Psi}^T\mathbf{M}\mathbf{\Psi}\right)^{-1}\left(\dot{x}^2\mathbf{\Psi}^T\mathbf{M}\mathbf{\Psi}_{,xx}+\mathbf{\Psi}^T\mathbf{K}\mathbf{\Psi}\right)$, where $\mathbf{\Omega}_{discrete}$ is a diagonal matrix containing the squares of the system's natural frequencies. These frequencies show that the string vibrates slower with increasing axially motion. For $v > c$ the system expressed by Eq. (4.23) is unstable, and the eigenvalues ω_n become complex.

For $v > 0$, matrix $\mathbf{A}$ has an influence on the system's vibration as well. For that reason it is more useful to examine the systems eigenvalues by inspecting $\mathbf{T}$. For a string/wire with a length of $L=1m$, density of $\rho_0=7850kg/m^3$, cross-sectional area of $A_0=7.854e^{-5}m^2$, and a tension of $T_0=1000N$, Figure 4-6 (left) shows the first five eigenvalues of the system. The same frequencies can be detected in the discrete model by recording the transient response of each mode; i.e., $\mathbf{z}$, for an arbitrary initial deflection of the string and transform the response into Fourier space, as shown in Figure 4-6 (right). This diagram shows that each mode vibrates not only at one particular frequency, as we would observe in a fixed string, but rather at different specific frequencies, which is due to the coupling of the modes in the Coriolis term in Eq. (4.20).

i	τ_i
1	15.1710
2	30.3433
3	45.5188
4	60.7005
5	75.8885

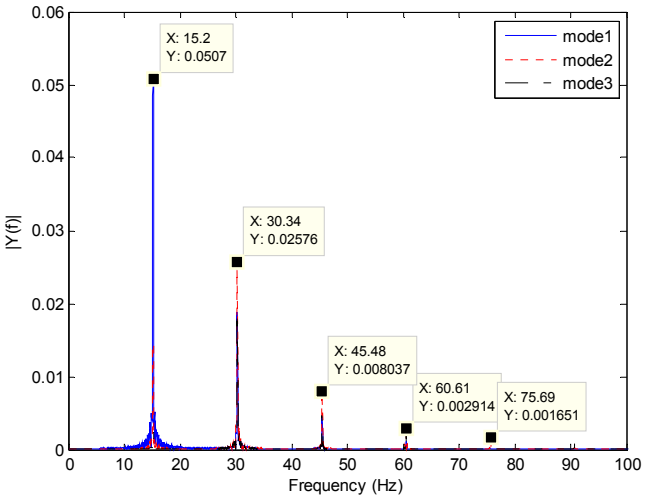

Figure 4-6: Frequency response of the individual modes.

4.2.4 Boundaries with variable size contact area

Consider the same string from section 5.2, but this time the string is partially wrapped over two pulleys, as shown in Figure 4-7. For convenience, the equations of motion for the non-traveling string with resizable contact area are repeated here:

$$\begin{bmatrix} \mathbf{M}^{ff} & \mathbf{0} & \mathbf{0} \\ \mathbf{0} & \mathbf{M}^{cc} & -\mathbf{D}^T \\ \mathbf{0} & \mathbf{D} & \mathbf{0} \end{bmatrix} \begin{Bmatrix} \ddot{\mathbf{u}}^f \\ \ddot{\mathbf{u}}^c \\ \boldsymbol{\lambda} \end{Bmatrix} = \begin{Bmatrix} \mathbf{g}^f \\ \mathbf{g}^c \\ \boldsymbol{\gamma} \end{Bmatrix} \tag{4.31}$$

In order to introduce the concept of *flowing material* on Eq. (4.31), modal transformation has to be performed first, i.e.

$$\begin{Bmatrix} \mathbf{u}^f \\ \mathbf{u}^c \end{Bmatrix} = \begin{bmatrix} \boldsymbol{\Psi} & \boldsymbol{\Psi}_s \\ \mathbf{0} & \mathbf{I} \end{bmatrix} \begin{Bmatrix} \mathbf{z} \\ \mathbf{u}^c \end{Bmatrix} \tag{4.32}$$

However, applying Eq. (4.13) on Eq. (4.32) will not be very helpful, since the contact nodes are still in nodal space. Therefore, a nodal to modal transformation for the contact

nodes needs to be performed as well. Modal transformation for the contact nodes is simply

$$\boldsymbol{\delta}^c = \boldsymbol{\Psi}^c \mathbf{z}^c \tag{4.33}$$

where $\boldsymbol{\Psi}^c$ is the matrix of normal deformation mode shapes for the *c*-nodes. Since these modes will not be truncated, static mode shapes are not required here. Combining Eq. (4.32) and Eq. (4.33) leads to

$$\begin{Bmatrix} \mathbf{u}^f \\ \mathbf{u}^c \end{Bmatrix} = \begin{bmatrix} \boldsymbol{\Psi}^f & \boldsymbol{\Psi}_s^c \\ \mathbf{0} & \boldsymbol{\Psi}^c \end{bmatrix} \begin{Bmatrix} \mathbf{z}^f \\ \mathbf{z}^c \end{Bmatrix} \tag{4.34}$$

where

$$\boldsymbol{\Psi}_s^c = \boldsymbol{\Psi}_s \boldsymbol{\Psi}^c \tag{4.35}$$

In these equations, the superscript *f* is included for the free nodes in order to differentiate them from the contact nodes. Applying Eq. (4.13) on Eq. (4.34) provides the velocity and acceleration transformations:

$$\begin{Bmatrix} \dot{\mathbf{u}}^f \\ \dot{\mathbf{u}}^c \end{Bmatrix} = \begin{bmatrix} \boldsymbol{\Psi}^f & \boldsymbol{\Psi}_s^c \\ \mathbf{0} & \boldsymbol{\Psi}^c \end{bmatrix} \begin{Bmatrix} \dot{\mathbf{z}}^f \\ \dot{\mathbf{z}}^c \end{Bmatrix} + \dot{x} \begin{Bmatrix} \mathbf{b}^f \\ \mathbf{b}^c \end{Bmatrix} \tag{4.36}$$

$$\begin{Bmatrix} \ddot{\mathbf{u}}^f \\ \ddot{\mathbf{u}}^c \end{Bmatrix} = \begin{bmatrix} \boldsymbol{\Psi}^f & \boldsymbol{\Psi}_s^c \\ \mathbf{0} & \boldsymbol{\Psi}^c \end{bmatrix} \begin{Bmatrix} \ddot{\mathbf{z}}^f \\ \ddot{\mathbf{z}}^c \end{Bmatrix} + \ddot{x} \begin{Bmatrix} \mathbf{b}^f \\ \mathbf{b}^c \end{Bmatrix} + \begin{Bmatrix} \mathbf{c}^f \\ \mathbf{c}^c \end{Bmatrix} \tag{4.37}$$

where

$$\begin{Bmatrix} \mathbf{b}^f \\ \mathbf{b}^c \end{Bmatrix} = \begin{bmatrix} \boldsymbol{\Psi}^f & \boldsymbol{\Psi}_s^c \\ \mathbf{0} & \boldsymbol{\Psi}^c \end{bmatrix}_{,s} \begin{Bmatrix} \mathbf{z}^f \\ \mathbf{z}^c \end{Bmatrix} \tag{4.38}$$

$$\begin{Bmatrix} \mathbf{c}^f \\ \mathbf{c}^c \end{Bmatrix} = \left(\begin{bmatrix} \boldsymbol{\Psi}^f & \boldsymbol{\Psi}_s^c \\ \mathbf{0} & \boldsymbol{\Psi}^c \end{bmatrix}_{,ss} \begin{Bmatrix} \mathbf{z}^f \\ \mathbf{z}^c \end{Bmatrix} \dot{x} + 2 \begin{bmatrix} \boldsymbol{\Psi}^f & \boldsymbol{\Psi}_s^c \\ \mathbf{0} & \boldsymbol{\Psi}^c \end{bmatrix}_{,s} \begin{Bmatrix} \dot{\mathbf{z}}^f \\ \dot{\mathbf{z}}^c \end{Bmatrix} \right) \dot{x} \tag{4.39}$$

Substituting Eq. (4.37) in Eq. (4.31) and pre-multiplying the first row with the transpose of $\boldsymbol{\Psi}^f$ yields

$$\begin{bmatrix} \mathbf{I} & \boldsymbol{\Psi}^{fT}\mathbf{M}^{ff}\boldsymbol{\Psi}_s^c & \mathbf{0} \\ \mathbf{0} & \mathbf{M}^{cc}\boldsymbol{\Psi}^c & -\mathbf{D}^T \\ \mathbf{0} & \mathbf{D}\boldsymbol{\Psi}^c & \mathbf{0} \end{bmatrix} \begin{Bmatrix} \ddot{\mathbf{z}}^f \\ \ddot{\mathbf{z}}^c \\ \boldsymbol{\lambda} \end{Bmatrix} = \begin{Bmatrix} \boldsymbol{\Psi}^{fT}\mathbf{g}^f \\ \mathbf{g}^c \\ \boldsymbol{\gamma} \end{Bmatrix} - \ddot{x} \begin{Bmatrix} \boldsymbol{\Psi}^{fT}\mathbf{M}^{ff}\mathbf{b}^f \\ \mathbf{M}^{cc}\mathbf{b}^c \\ \mathbf{D}\mathbf{b}^c \end{Bmatrix} - \begin{Bmatrix} \boldsymbol{\Psi}^{fT}\mathbf{M}^{ff}\mathbf{c}^f \\ \mathbf{M}^{cc}\mathbf{c}^c \\ \mathbf{D}\mathbf{c}^c \end{Bmatrix} \tag{4.40}$$

Since the contact nodes are not truncated, there is no need to pre-multiply the second row by the transpose of $\boldsymbol{\Psi}^c$. By eliminating some columns of $\boldsymbol{\Psi}^f$, the system can be reduced in its total degrees-of-freedom.

It should be noted that, even though Eq. (4.40) is established for a traveling string with variable size contact area, this equation can fairly represents a section of a fast rotating belt drive. As a matter of fact, many analytical belt drive models that are used even today, can only represent a section of the belt, similar to the one shown in Figure 4-7. For these models the belt behavior on the remaining contact area is neglected.

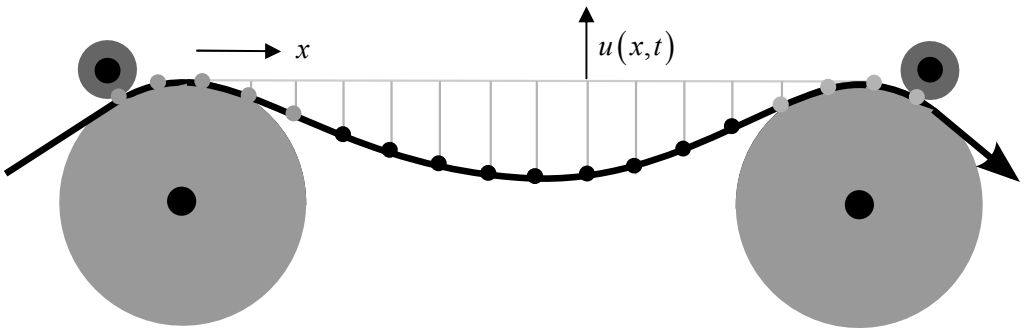

Figure 4-7: A traveling string wrapped around pulleys at both ends.

4.3 Discussion

This chapter focused on two types of boundary conditions: variable size contact area, and traveling contact area. As an application example, a string model is introduced

that represents the transversal vibration of a belt between two pulleys. The equations of motion for this model are derived and extended with the following four boundary conditions: fixed boundaries, moving boundaries, variable size boundaries, and traveling boundaries. The variable size boundaries allow the string model to represent a belt that can partially lift off the pulleys. Boundary conditions with variable size contact area are of major interest in deformable multibody dynamics, especially in conjunction with model truncation. Besides the belt drive, these types of boundary conditions can occur in more complex applications, as it will be shown in the coming chapters. The traveling boundaries become another difficulty if the deformable body needs to be condensed in its number of degrees-of-freedom. In order to resolve this issue, a new concept is introduced that takes advantage of an orientation invariant characteristic that may exist in some deformable bodies. This characteristic allows the mesh of the body to be decoupled from the motion of its mass points in a particular direction. If this direction coincides with the direction of travel of the contact area, then the contact area becomes stationary with respect to the mesh; i.e., only few nodes on the surface of the body are potential candidates for contact. This allows the deformable body to be condensed with the usual reduction techniques. The new concept is shown on a simple belt (string) model, but can also be applied to more complex systems, as it is shown in the following chapters.

5. POWER TRANSMISSION BELT

The previous chapter introduced a belt drive that was approximated through a string or beam model. While this model provides a good first insight into belt vibration, it is insufficient for complex drive-train analysis. The most significant drawback of this model is its inability to predict angular velocity losses between the driver and driven pulleys. In order to capture these losses, finite element based models of a complete belt drive have recently been developed that represent the pulleys as rigid bodies and the entire belt as a flexible body [51, 52]. In these models the belt rotates around the pulleys that cause the grid nodes of the belt to come into contact with the pulleys over and over again. This characteristic allows the newer models to represent stick-slip friction between the belt and the pulleys. However, the same characteristic prevents the newer models being reduced in their total degrees-of-freedom that leads consequently to higher computational requirements.

This chapter combines the findings from Chapter 4 and applies them to a FE model of a complete belt. In doing so, a new belt drive model is developed that allows modal truncation without violating the contact conditions. With few modifications to the material properties and contact definition, the same model can also represent a chain drive as a first approximation. The power transmission belt and chain are similar in their application; both transmit torque from one axle to another axle via a flexible connection (belt/chain). This chapter reviews previously developed belt and chain drive models first.

Then it derives the equations of motion for the proposed belt drive model in both nodal and modal space.

5.1 Previous belt/chain drive models

A detailed picture of knowledge on belt vibration, prior to 1991, is given in [44, 46, 47]. Since then more research has been conducted on belt vibration. Recently, the problem of axially moving beams has been studied in a more systematic way. Wickert [47] investigated the non-linear vibration and bifurcations of moving beams in sub- and super-critical speed ranges performing a local analysis for non-linear oscillations. Pellicano and Vestroni [48] summarized more work that had been conducted in this field. Moon and Wickert [49] as well as Pellicano et al. [50] extended the study of non-linear moving beams to complete power transmission belt systems and validated their analytical results against experimental data. Here, Laser Doppler Vibrometer or Laser Telemeter is used to measure the response of the moving belt. The experimental results confirm the hardening character of the analytical models for a non-linear moving beam. Although analytical models are helpful in the general understanding of belt vibration, their applications are limited and their solutions can be quite complicated. For that reason pure numerical models of different grade of complexity have been developed. Some models incorporate some sort of FE approach [51, 52], that can also capture the sliding wear of the belt that is caused by the creep between the pulley and the belt. This wear deteriorates the surface of the belt and changes the friction characteristic between the belt and the pulleys, which in turn causes loss in tension and noisy operation. Leamy and

Wasfy [51] used truss elements to describe the belt, where only Cartesian coordinates of the nodes were used as DoFs. These DoFs are defined in a global inertial frame. Contact is applied at the nodes that also include a detailed belt-pulley friction model. Kerkkanen et al. [52] used modified two-dimensional shear deformable beam elements where an absolute nodal coordinate formulation was used instead. This leads to an exact description of an arbitrary rigid body motion, a constant mass matrix and the capability of modeling nonlinear deformations. While the FE based models can provide a good approximation of the total power transmission system, it should be emphasized that these models may contain many DoFs and, hence, require long computing times.

Besides the investigations of belt vibration, several studies have been conducted on the vibration of chain drives as well, especially with a focus on the phenomenon of polygonal action and chain-sprocket impact. An insight into the state-of-the-art until 1990 is provided by Wang and Liu [53]. The dynamical behavior of chain drives have been studied only in the last decades due to their dynamic complexity. General analytical approaches cannot capture the whole problem thoroughly [53]. Turnbull and Fawcett [54] as well as Chew [55] investigate the influence of impulsive forces that act on the chain segments and sprockets at the moment of their engagement, which results in a discontinuity of the rollers velocity. A discrete model that includes the polygonal effect is proposed by Veikos and Freudenstein [56]. Here, the driving span of the chain is modeled by lumped masses that are connected through linear springs. This model considers the moving boundaries as well as vibration in longitudinal and transversal direction. However, angular speed fluctuations of the driving sprocket are not considered.

Chew [55] proposes a more complex model that can describe the dynamics of the chain drive system more in detail. It includes chain guides as well as moving sprockets. The contact between chain-sprocket and chain-chain guides are treated as unilateral constraints. More recent work has been done by Fritz and Pfeiffer [57] as well as Troedson and Vedmar [58, 59], who present models that includes standard geometry of the sprockets. The contact is defined by an iterative force equilibrium method. Pedersen [60] includes chain guides and a detailed geometry of the sprocket as well, and contact is defined by a continuous contact force method based on Hertzian contact force equilibrium. Most of these recent models represent each chain element as a rigid body that is connected to its neighboring elements through springs and dampers. It should be noted that the high stiffness characteristic of the spring elements can induce a high numerical stiffness in the chain system, if damping is not considered appropriately. This in turn can lead to long computing times, especially for long chain systems that include many chain elements.

5.2 The new belt drive model

The preceding literature review shows that many high fidelity numerical models have been created for power transmission belts and chains. However, as for now, most of these models lack the ability to be reduced in the number of degrees-of-freedom to achieve computational efficiency. This chapter introduces a new belt drive model that overcomes this disadvantage. Here, we consider a two-dimensional finite element model of a power transmission belt, where the belt moves over two pulleys forming a closed

loop, as shown in Figure 5-1. The belt can be modeled as a collection of beam or truss elements (or any other suitable elements), where at any given instant some nodes are free and some are in contact with the pulleys.

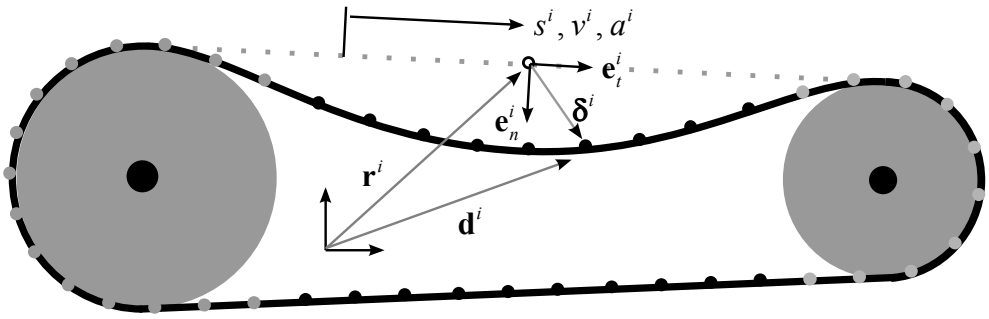

Figure 5-1: Power transmission belt with free (black) and contact nodes (gray).

Similar to the string problem in Section 4.1.2 and Section 4.2.4, the belt can partially lift off the pulley due to vibration, as shown in Figure 5-2. This in turn results into varying number of nodes in free and constrained portions. To address this issue, the nodes of the FE grid are partitioned again into two groups: those that are free, designated as *f*-nodes (colored in black in Figure 5-1 and Figure 5-2); and those that might come in contact with the pulleys, designated as *c*-nodes (colored in gray). However, when the belt rotates, free nodes will become into contact with the pulleys after a period of time, which requires the nodes to be repartitioned. In order to avoid this, the idea of *flowing material* can be applied to the equations of motion of the belt. This consequently leads to a stationary grid; i.e., the FE mesh will not rotate with the belt and the designated sets of free and contact nodes remain the same.

In the upcoming equations the idea of *flowing material* is applied to the equations of motion of a two dimensional power transmission belt. These equations can easily be

extended to a three dimensional belt model. Even though the upcoming equations refer to a belt drive, they can be used for a first approximation of a chain drive as well.

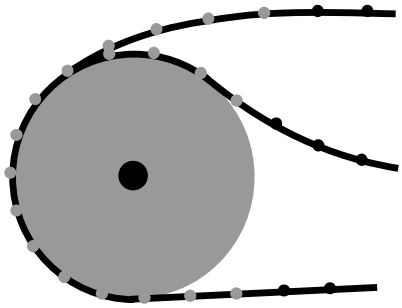

Figure 5-2: Vibrating belt/chain with varying contact area.

5.3 Equations of motion in nodal space

Consider a two-dimensional finite element model of a power transmission belt, as shown in Figure 5-1. When the belt rotates about the pulleys, but does not vibrate, the traveling path of each node is known. At a given instant node i is at position s^i, measured from a fixed reference point. For convenience, the motion of each node can be described using normal and tangential coordinate axes. Here each node has its own reference frame. The origin of each frame is fixed to the corresponding node. The axis tangent to the path, $\mathbf{e}_t^i$, is positive in the direction of increasing s^i. A unique choice for the normal axis can be made by noting that geometrically the path is constructed from a series of differential arc segments ds. Each segment is formed from the arc of an associated circle having a radius of curvature ρ and center of curvature O'. Note that for the straight sections of the belt the radius of curvature is infinity. The normal axis $\mathbf{e}_n^i$ is positive when directed toward the center of curvature.

When the belt vibrates as it rotates, the undeflected position of the node i is superimposed by a deflection $\boldsymbol{\delta}^i$. The position of node i with respect to an inertial frame is

$$\mathbf{d}^i = \mathbf{r}^i + \boldsymbol{\delta}^i \tag{5.1}$$

The respective velocity and acceleration of that note are defined as

$$\dot{\mathbf{d}}^i = v^i \mathbf{e}_t^i + \dot{\boldsymbol{\delta}}^i \tag{5.2}$$

$$\ddot{\mathbf{d}}^i = a^i \mathbf{e}_t^i + \frac{v^{i^2}}{\rho^i} \mathbf{e}_n^i + \ddot{\boldsymbol{\delta}}^i \tag{5.3}$$

with $v^i = ds^i/dt$ and $a^i = dv^i/dt$, both having a direction that is always tangent to the path. Since the distance between the nodes in their undeflected state is always constant, $a^i = a$ and $v^i = v$ are the same for all the nodes. Hence the total acceleration for all the nodes can be written as

$$\ddot{\mathbf{d}} = \begin{bmatrix} \mathbf{e}_t & \bar{\mathbf{I}} \end{bmatrix} \begin{Bmatrix} a \\ \ddot{\boldsymbol{\delta}} \end{Bmatrix} + v^2 \boldsymbol{\varepsilon}_n \tag{5.4}$$

where $\bar{\mathbf{I}}$ is an identity matrix and $\boldsymbol{\varepsilon}_n = \begin{bmatrix} \mathbf{e}_n^{1T}/\rho_1 & \cdots & \mathbf{e}_n^{mT}/\rho_m \end{bmatrix}^T$.

The equation of motion for the belt in term of absolute nodal accelerations can be written as

$$\mathbf{M}\ddot{\mathbf{d}} = \mathbf{f} - \mathbf{K}\boldsymbol{\delta} - \mathbf{C}\dot{\boldsymbol{\delta}} \tag{5.5}$$

with $\mathbf{f}$ containing external forces. Here the mass matrix $\mathbf{M}$ and the stiffness matrix $\mathbf{K}$ are constructed for the belt in its equilibrium state but without any boundary condition, therefore $\mathbf{K}$ has a rank deficiency of three (the rigid body degrees-of-freedom). Substituting Eq. (5.4) into (5.5) and pre-multiplying it by $\begin{bmatrix} \mathbf{e}_t & \bar{\mathbf{I}} \end{bmatrix}^T$ yields

$$\begin{bmatrix} \mathbf{e}_t^T\mathbf{M}\mathbf{e}_t & \mathbf{e}_t^T\mathbf{M} \\ \mathbf{M}\mathbf{e}_t & \mathbf{M} \end{bmatrix} \begin{Bmatrix} a \\ \ddot{\boldsymbol{\delta}} \end{Bmatrix} = \begin{Bmatrix} \mathbf{e}_t^T\mathbf{g} \\ \mathbf{g} - v^2\mathbf{M}\boldsymbol{\varepsilon}_n \end{Bmatrix} \tag{5.6}$$

where $\mathbf{g} = \mathbf{f} - \mathbf{K}\boldsymbol{\delta} - \mathbf{C}\dot{\boldsymbol{\delta}}$. Note that $\mathbf{e}_t^T\mathbf{M}\mathbf{e}_t = m$ represents the mass of the belt, and $\mathbf{e}_t^T\mathbf{M}\boldsymbol{\varepsilon}_n = \mathbf{0}$, since $\mathbf{e}_t$ and $\boldsymbol{\varepsilon}_n$ are orthogonal to each other even in respect to $\mathbf{M}$. Equation (5.6) cannot be solved for the unknown accelerations, since the matrix on the left side has a rank deficiency of one. This problem is similar to the rank deficiency that occurs in the floating frame of reference formulation, as explained in Chapter 2. A reference condition needs to be introduced into the formulation in order to eliminate the extra degree-of-freedom. This can be done by constraining only one node in the tangential direction of its reference frame.

At this point the nodes are split into the free and contact nodes, and contact constraints between the *c*-nodes are included through the use of Lagrange multipliers:

$$\begin{bmatrix} m & \mathbf{e}_t^{fT}\mathbf{M}^{ff} & \mathbf{e}_t^{cT}\mathbf{M}^{cc} & \mathbf{0} \\ \mathbf{M}^{ff}\mathbf{e}_t^f & \mathbf{M}^{ff} & \mathbf{0} & \mathbf{0} \\ \mathbf{M}^{cc}\mathbf{e}_t^c & \mathbf{0} & \mathbf{M}^{cc} & -\mathbf{D}^T \\ \mathbf{0} & \mathbf{0} & \mathbf{D} & \mathbf{0} \end{bmatrix} \begin{Bmatrix} a \\ \ddot{\boldsymbol{\delta}}^f \\ \ddot{\boldsymbol{\delta}}^c \\ \boldsymbol{\lambda} \end{Bmatrix} = \begin{Bmatrix} \mathbf{e}_t^{fT}\mathbf{g}^f + \mathbf{e}_t^{cT}\mathbf{g}^c \\ \mathbf{g}^f - v^2\mathbf{M}^{ff}\boldsymbol{\varepsilon}_n^f \\ \mathbf{g}^c - v^2\mathbf{M}^{cc}\boldsymbol{\varepsilon}_n^c \\ -\dot{\mathbf{D}}\dot{\boldsymbol{\delta}}^c \end{Bmatrix} \tag{5.7}$$

where $\mathbf{D}$ is the Jacobian matrix of the constraints, and

$$\begin{Bmatrix} \mathbf{g}^f \\ \mathbf{g}^c \end{Bmatrix} = \begin{Bmatrix} \mathbf{f}^f \\ \mathbf{f}^c \end{Bmatrix} - \begin{bmatrix} \mathbf{K}^{ff} & \mathbf{K}^{fc} \\ \mathbf{K}^{cf} & \mathbf{K}^{cc} \end{bmatrix} \begin{Bmatrix} \boldsymbol{\delta}^f \\ \boldsymbol{\delta}^c \end{Bmatrix} \tag{5.8}$$

It should be noted again that not all of the *c*-nodes need to be constrained — only those that are in contact with the pulley. Some *c*-nodes may come in contact with the pulley only due to the vibration of the belt.

Equation (5.7) represents the equations of motion for the belt, where the FE mesh rotates with the belt. In the following section the method of *flowing material* will be introduced into this equation in order for the mesh to remain stationary.

5.4 Equations of motion in modal space

The nodal to modal transformations for the free nodes are expressed as

$$\begin{Bmatrix} \boldsymbol{\delta}^f \\ \boldsymbol{\delta}^c \end{Bmatrix} = \begin{bmatrix} \boldsymbol{\Psi}^f & \boldsymbol{\Psi}_s^c \\ \mathbf{0} & \boldsymbol{\Psi}^c \end{bmatrix} \begin{Bmatrix} \mathbf{z}^f \\ \mathbf{z}^c \end{Bmatrix} \tag{5.9}$$

where $\boldsymbol{\Psi}^f$ and $\boldsymbol{\Psi}^c$ are the matrices of normal deformation mode shapes and for the free and contact nodes, respectively. Furthermore, $\boldsymbol{\Psi}_s^c = \boldsymbol{\Psi}_s \boldsymbol{\Psi}^c$ with $\boldsymbol{\Psi}_s = -\mathbf{K}^{ff^{-1}} \mathbf{K}^{fc}$ representing the static mode shapes. Applying Eq. (4.13) to Eq. (5.9) provides the velocity and acceleration transformations:

$$\begin{Bmatrix} \dot{\boldsymbol{\delta}}^f \\ \dot{\boldsymbol{\delta}}^c \end{Bmatrix} = \begin{bmatrix} \boldsymbol{\Psi}^f & \boldsymbol{\Psi}_s^c \\ \mathbf{0} & \boldsymbol{\Psi}^c \end{bmatrix} \begin{Bmatrix} \dot{\mathbf{z}}^f \\ \dot{\mathbf{z}}^c \end{Bmatrix} + v \begin{Bmatrix} \mathbf{b}^f \\ \mathbf{b}^c \end{Bmatrix} \tag{5.10}$$

$$\begin{Bmatrix} \ddot{\boldsymbol{\delta}}^f \\ \ddot{\boldsymbol{\delta}}^c \end{Bmatrix} = \begin{bmatrix} \boldsymbol{\Psi}^f & \boldsymbol{\Psi}_s^c \\ \mathbf{0} & \boldsymbol{\Psi}^c \end{bmatrix} \begin{Bmatrix} \ddot{\mathbf{z}}^f \\ \ddot{\mathbf{z}}^c \end{Bmatrix} + a \begin{Bmatrix} \mathbf{b}^f \\ \mathbf{b}^c \end{Bmatrix} + \begin{Bmatrix} \mathbf{c}^f \\ \mathbf{c}^c \end{Bmatrix} \tag{5.11}$$

where

$$\begin{Bmatrix} \mathbf{b}^f \\ \mathbf{b}^c \end{Bmatrix} = \begin{bmatrix} \boldsymbol{\Psi}^f & \boldsymbol{\Psi}_s^c \\ \mathbf{0} & \boldsymbol{\Psi}^c \end{bmatrix}_{,s} \begin{Bmatrix} \mathbf{z}^f \\ \mathbf{z}^c \end{Bmatrix} \tag{5.12}$$

$$\begin{Bmatrix} \mathbf{c}^f \\ \mathbf{c}^c \end{Bmatrix} = \left(\begin{bmatrix} \boldsymbol{\Psi}^f & \boldsymbol{\Psi}_s^c \\ \mathbf{0} & \boldsymbol{\Psi}^c \end{bmatrix}_{,ss} \begin{Bmatrix} \mathbf{z}^f \\ \mathbf{z}^c \end{Bmatrix} v + 2 \begin{bmatrix} \boldsymbol{\Psi}^f & \boldsymbol{\Psi}_s^c \\ \mathbf{0} & \boldsymbol{\Psi}^c \end{bmatrix}_{,s} \begin{Bmatrix} \dot{\mathbf{z}}^f \\ \dot{\mathbf{z}}^c \end{Bmatrix} \right) v \tag{5.13}$$

Here, v and a are the velocity and acceleration of the belt in rolling direction, as shown in Figure 5-1. The modes in the transformation matrix of Eq. (5.9) are split into its

coordinates; e.g., $x(s)$, $y(s)$, and $\theta(s)$ for beam elements. Then the partial derivatives of the modes are obtained through the method of finite differences.

Substituting Eq. (5.11) into Eq. (5.7) and pre-multiplying the second row by $\boldsymbol{\Psi}^{fT}$ provide the equation of motions for the rolling belt as

$$\begin{bmatrix} m+\mathbf{e}_t^{fT}\mathbf{M}^{ff}\mathbf{b}^f+\mathbf{e}_t^{cT}\mathbf{M}^{cc}\mathbf{b}^c & \mathbf{e}_t^{fT}\mathbf{M}^{ff}\boldsymbol{\Psi}^f & \mathbf{e}_t^{fT}\mathbf{M}^{ff}\boldsymbol{\Psi}_s^c+\mathbf{e}_t^{cT}\mathbf{M}^{cc}\boldsymbol{\Psi}^c & \mathbf{0} \\ \boldsymbol{\Psi}^{fT}\mathbf{M}^{ff}\mathbf{e}_t^f+\boldsymbol{\Psi}^{fT}\mathbf{M}^{ff}\mathbf{b}^f & \boldsymbol{\Psi}^{fT}\mathbf{M}^{ff}\boldsymbol{\Psi}^f & \boldsymbol{\Psi}^{fT}\mathbf{M}^{ff}\boldsymbol{\Psi}_s^c & \mathbf{0} \\ \mathbf{M}^{cc}\mathbf{e}_t^c+\mathbf{M}^{cc}\mathbf{b}^c & \mathbf{0} & \mathbf{M}^{cc}\boldsymbol{\Psi}^c & -\mathbf{D}^T \\ \mathbf{D}\mathbf{b}^c & \mathbf{0} & \mathbf{D}\boldsymbol{\Psi}^c & \mathbf{0} \end{bmatrix} \begin{Bmatrix} a \\ \ddot{\mathbf{z}}^f \\ \ddot{\mathbf{z}}^c \\ \boldsymbol{\lambda} \end{Bmatrix} = \begin{Bmatrix} \mathbf{e}_t^{fT}\mathbf{g}^f+\mathbf{e}_t^{cT}\mathbf{g}^c \\ \boldsymbol{\Psi}^{fT}\mathbf{g}^f-v^2\boldsymbol{\Psi}^{fT}\mathbf{M}^{ff}\boldsymbol{\varepsilon}_n^f \\ \mathbf{g}^c-v^2\mathbf{M}^{cc}\boldsymbol{\varepsilon}_n^c \\ -\dot{\mathbf{D}}\dot{\boldsymbol{\delta}}^c \end{Bmatrix} - \begin{Bmatrix} \mathbf{e}_t^{fT}\mathbf{M}^{ff}\mathbf{c}^f+\mathbf{e}_t^{cT}\mathbf{M}^{cc}\mathbf{c}^c \\ \boldsymbol{\Psi}^{fT}\mathbf{M}^{ff}\mathbf{c}^f \\ \mathbf{M}^{cc}\mathbf{c}^c \\ \mathbf{D}\mathbf{c}^c \end{Bmatrix} \tag{5.14}$$

This equation is in a form where the mesh of the FE model does not rotate with the belt. This means that $\mathbf{M}$, $\mathbf{K}$, $\mathbf{C}$, $\boldsymbol{\Psi}$, e_t, e_n, and $\boldsymbol{\varepsilon}_n$ are constant matrices and arrays that can be calculated ahead of time. Furthermore, the modal coordinates associated with the *f*-nodes can be truncated in order to reduce the size of the problem.

5.5 Discussion

The review of previous belt/chain models introduces a set of high fidelity numerical models for power transmission belts and chains. However, all of these models lack the ability to be truncated for computational efficiency. The new belt drive model that is described by Eq. (5.14) is a high fidelity model as well, but also includes the capability of system reduction to increase computational performance. It is based on modal reduction; i.e., the system can be reduced in its total DoF without altering its dynamical behavior significantly.

Besides the advantage of system reduction, it is worthwhile to mention another feature of the new model. In previous developed belt models, the mesh rotates with the belt. If the belt is split into equally long beam elements, then an artificial periodic excitation can occur due to the discretization of the belt, since contact forces can only act on the grid nodes. This leads to a vibration behavior similar to a chain and its polygonal action (chord effect) and, if the excitation matches a natural frequency of the belt, to resonance. In order to avoid the periodic vibration, researchers change the length of the beam elements randomly [61], which also has an effect on the location of the contact points. This avoids eventually resonance, but does not avoid the artificial vibration in general. The belt drive model represented here does not have the effect of artificial vibration, since the mesh does not rotate with the belt.

6. NUMERICAL SIMULATION OF A POWER TRANSMISSION BELT

In the previous chapter a new power transmission belt model is introduced that includes the concept of *flowing material*. This model allows the finite element mesh of the belt to remain stationary while the belt rotates around the pulleys. The subsequent advantage lies in the capability of the belt drive model to be truncated in its total degrees-of-freedom. This chapter provides an example for using the new power transmission belt model where the focus is on angular speed loss and non-rotating FE mesh. The example is a two pulley-belt drive system. Numerical results are compared against experimental and analytical data that are provided by Čepon et. al. [61] and Bechtel et. al. [70].

6.1 Two pulley-belt drive system

For the experimental tests a V-ripped belt with five rips and a K-rip section (5PK) was used, as shown in Figure 6-1. Čepon et. al [62] performed detailed tests with this belt to obtain its parameters, such as stiffness and damping. They also obtained contact parameters for the pulley-belt contact [63]. In order to validate the new power transmission belt model, all these parameters were adopted and included in the new model.

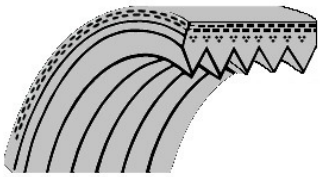

Figure 6-1: Cross-section of the V-ripped belt with five rips.

A graphical representation of the belt drive model is given in Figure 6-2, where the direction of motion for the belt is as indicated. The external moments that act on the pulleys are equal in magnitude, but opposite in direction. The belt is discretized non-uniformly with 56 beam elements. The length of the beam elements along the pulleys are kept short compared to the length on the straight section, in order to increase the fidelity at the belt-pulley contact area. Each element consists of two nodes, where each node has two translational and one rotational DoF. The belt is divided into two sets of nodes: the free nodes that are indicated by black circles, and the contact nodes that are represented by gray circles. The reader should bear in mind that only the contact nodes are candidates to come in contact with the pulley, since the finite element mesh does not rotate with the material of the belt. The parameterization of the belt drive system is summarized in Table 6-1.

New belt materials, such as plastic, metal or ceramic-reinforced composite materials, and polymer materials, usually exhibit viscoelastic behavior. In order to represent this viscoelasticity, damping needs to be considered as well. The new belt drive model includes Rayleigh damping, where the damping matrix is a linear combinations of a constant mass and constant stiffness matrix; i.e., $\mathbf{C} = \alpha\mathbf{M} + \beta\mathbf{K}$ with α and β being the Rayleigh parameters that are provided in [62].

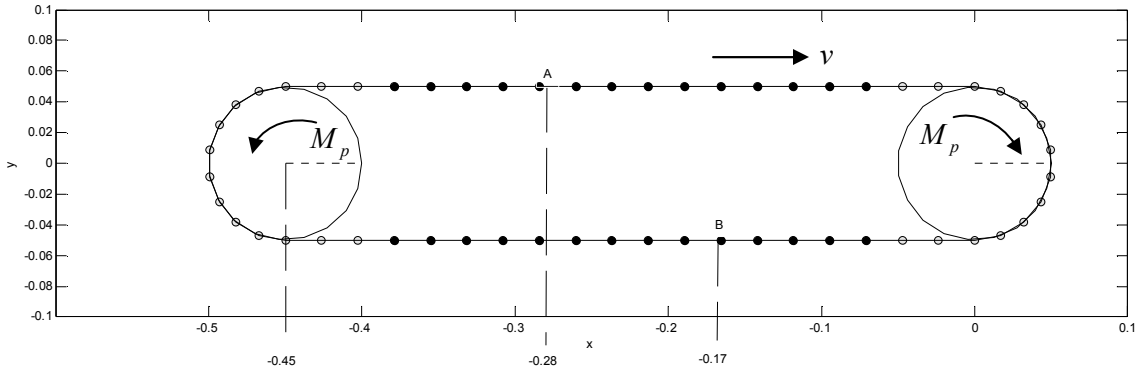

Figure 6-2: Belt drive system as a rigid-deformable multibody system.

Parameter	Value
Radius of both pulleys	$R = 0.05\ m$
Belt length	$L_{Belt} = 1.2\ m$
Mass moment of inertia of both pulleys	$J_{Pulley} = 0.013\ kg\ m^2$
Central distance between pulleys	$L_c = 0.45\ m$
Density of belt	$\rho = 0.096\ kg/m$
Axial stiffness of belt	$EA = 152000\ N$
Bending stiffness	$EI = 2.6e^{-2}\ Nm^2$
Rayleigh damping parameters	$\alpha = 2.8\ s^{-1};\quad \beta = 1.8e^{-3}\ s$
Kinematic friction coefficient for pulley-belt contact	$\mu_{kin} = 1.2$
Slip parameter for the Coloumb like friction model	$\kappa = 40$

Table 6-1: Parameters for the belt drive system.

6.2 Rotating vs. non-rotating belt

In this and the previous chapters, strong attention is paid to the FE mesh being independent of the rotation of the belt. In order to obtain a more visual picture about this characteristic, two fictitious and exaggerated simulations are provided here. In the first simulation it is assumed that the belt and the pulleys do not rotate. The belt is initially deflected on the upper half between the pulleys, as shown in Figure 6-3 (left column). In the second simulation, the belt has the same initial deflection, but the belt and the pulleys rotate with a constant speed, as shown in Figure 6-3 (right column). Both simulations show the vibration of the belt for a timeframe of a few milliseconds. It can be observed that the belt behaves differently in the two simulations. While in the non-rotating belt the initial deflection propagates symmetrically to both sides of the belt as a wave, in the rotating system it tends to move with the belt. This is expected due to the rotating mass. Also, the second simulation indicates that the frequency of the belt vibration changes inversely to the rotating speed; i.e., the faster the belt rotates the smaller is its vibration frequency. The influence of rotational speed on the vibration of the flexible body has already been observed in the string model (see 4.2).

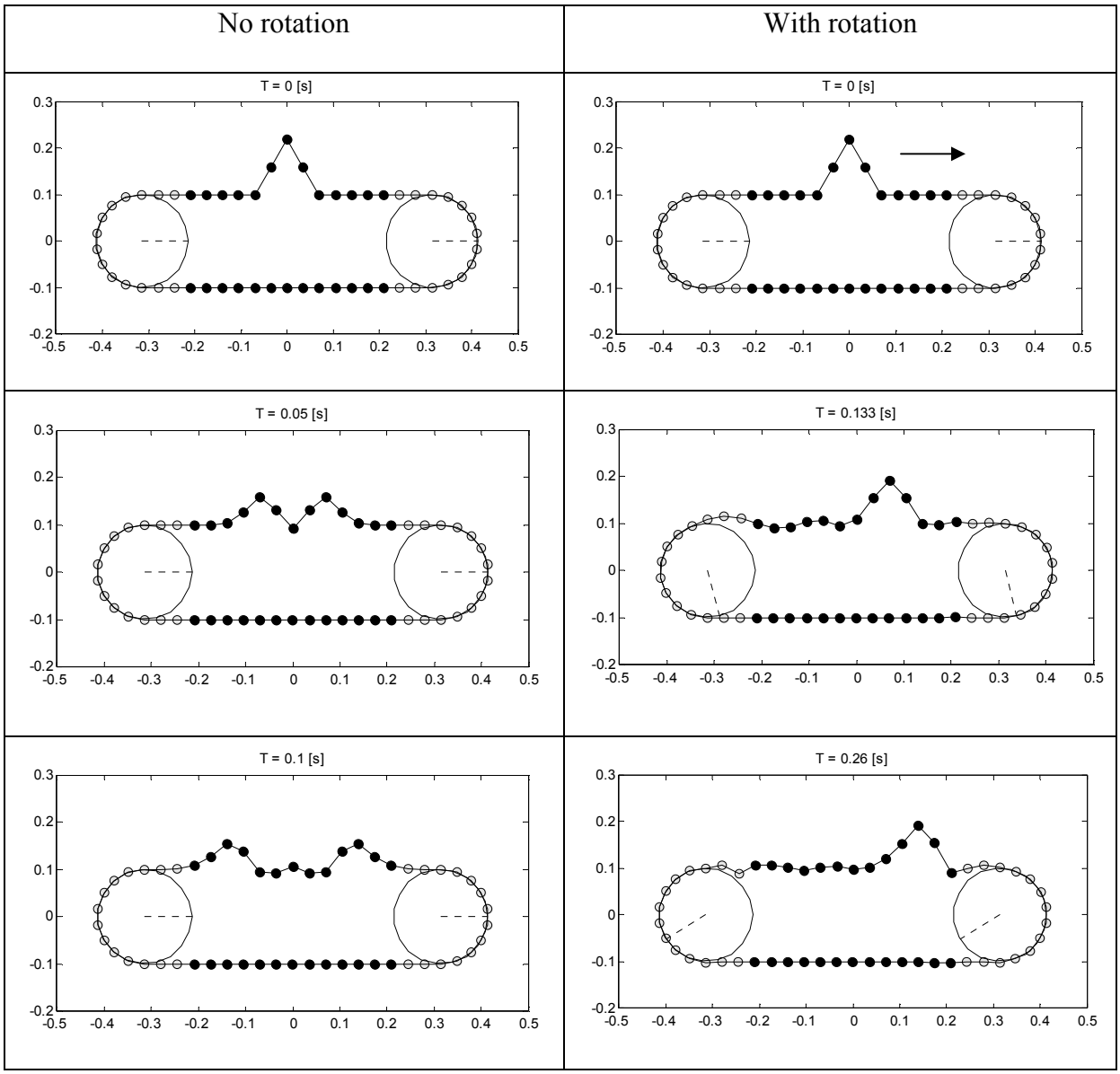

Figure 6-3: Simulation animation of a non-rotating (left column) and rotating belt (right column). Deflections are highly exaggerated.

6.3 Angular speed loss

The efficiency of a power transmission belt can be defined by the loss of angular speed between the driver and the driven pulley. Due to the opposite moments, the belt

has a *tight-side* with tension T_1 and a *slack-side* with tension T_2, where $T_1 > T_2$. Since the belt is of elastic nature, it stretches on the tight-side more than on the slack-side, which causes a difference in speed at both sides ($v_1 > v_2$), as shown in Figure 6-4(a). This difference results in an angular speed loss between the pulleys that can be explained through three phenomena [64]:

- Creep along contact area
- Shear deformation in the belt
- Radial compliance

The physical interpretation of creep is simple [65, 66]: There is a tight belt running onto the driver pulley and a slack belt running off – or the opposite for a driven pulley, as shown in Figure 6-4(a). An elastic belt has to change length while it is in contact with the pulley. This stretching or unstretching occurs near the departure from the pulley. At the driver pulley, the belt runs onto the pulley with a tight-side tension T_1 and velocity v_1. The velocity of the belt matches the speed of the pulley at its outer surface. At first, both speeds remain equal and constant while the belt rotates around the pulley. This portion of contact area is referred to as the *idle arc*. However, at a particular angle, the belt begins to creep against the pulley while its velocity continuously slows to v_2. The resulting sliding friction changes the tension in the belt. This part is referred to as the *effective arc*. Finally the belt leaves the pulley with its slack-side tension T_2 and velocity v_2. The opposite happens on the driven pulley. As load is increased, the point of creep begins to move around the pulley toward the entry side. At the point where the creep starts to occur very near the entry side, slip starts.

Shear deformation is another reason for the angular speed loss [67]. It occurs in the cross-section of the belt, while the belt rotates around the pulley. Consider one point of the belt that is in contact with the pulley. Due to static friction, this point and the pulley move at the same speed. If the speed of the belt changes, a state of shear strain occurs from the contact point through the belt to the cord layer, as shown in Figure 6-4(b). The shear strain causes shear stress, and if this stress exceeds static friction, the belt starts to slip on the pulley.

Radial compliance occurs on the pulley-belt contact area as well [61]. Since the belt experiences a difference in tension between the tight- and slack-side, the radial load on the belt changes along the contact. This again has an effect on the radial deformation of the rubber layer that causes a difference in the effective radius of the belt at the entry and exit of the pulley-belt contact, as shown in Figure 6-4(c).

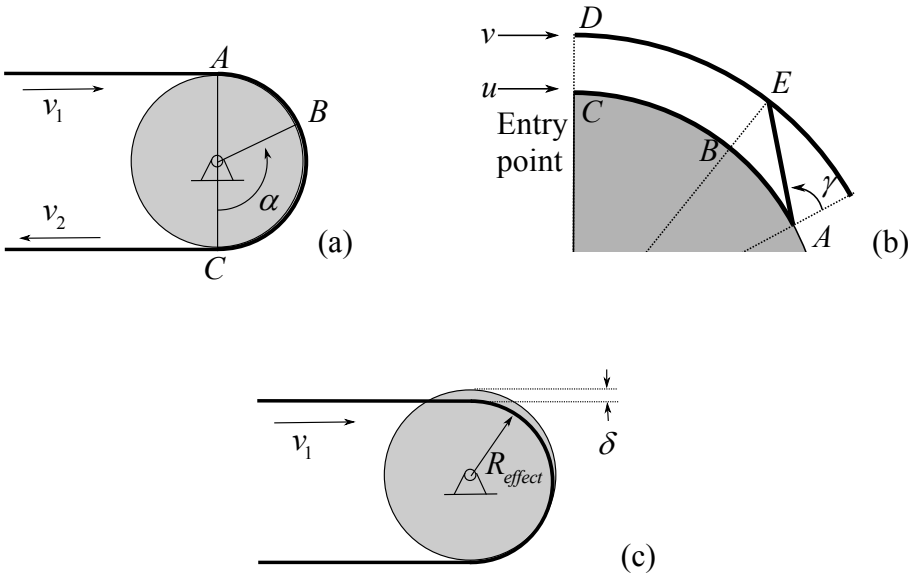

Figure 6-4: (a) Driving drum with AB being the idle arc and BC being the effective arc; (b) Belt shear at arc of adhesion [67]; (c) Radial compliance.

6.4 Implementation of creep and radial compliance

The previous section describes the angular speed loss as the effect of creep, shear deformation, and radial compliance. However, in the new belt drive model only creep and radial compliance is considered. Due to the characteristic of the beam elements used in this model, shear deformations cannot be represented. Shear deformations could be captured if the belt is modeled using other appropriate finite elements. Furthermore, the beam elements used in this model have a constant cross-sectional area that does not allow for representation of radial compliance. Nevertheless, radial compliance can be included in the model by representing the contact between the belt and the pulleys through a penalty approach instead of the method of Lagrange multipliers; i.e. the Lagrange multipliers in Eq. (6.14) are replaced by penal forces. The penal force on a contact node in normal direction is given by [63]:

$$F_N(\delta_N) = 3025.6e^8 L_{ele}\delta_N^2 + 6.5e^7 L_{ele}\delta_N \tag{6.1}$$

where L_{ele} is the length of the belt section represented by the contact node and δ_N is the penetration in normal contact direction, as shown in Figure 6-5. When contact is represented through a penalty approach, we allow creep between the belt and the pulleys to be represented through a Coulomb like friction model. The tangential friction force between the belt and the pulley is defined as:

$$F_T(v_{slip}) = \mu_{kin}\tanh(\kappa v_{slip})F_N \tag{6.2}$$

where v_{slip} is the relative velocity between the contact node and the pulley, μ_{kin} is the kinematic friction coefficient, and κ is a slip parameter. Representative values for κ

can be obtained from experimentally measured traction curves found in the literature. A similar friction model for pulley-belt contact was successfully implemented and validated by Leamy and Wasfy [68].

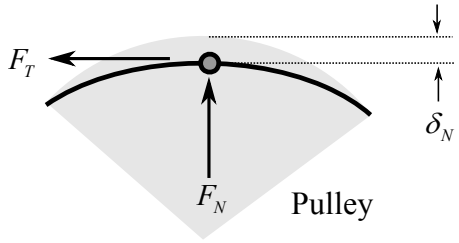

Figure 6-5: Pulley-belt contact and friction model.

6.5 Simulating angular speed loss

For many belt drive applications, engineers are mostly interested in the belt drive's efficiency and noise emission. Low efficiency can increase operational costs, maintenance costs, and noise emission. Since belt drive efficiency is mainly determined by the angular speed loss, the losses in the new belt drive model are compared against experimental, numerical, and analytical data given in [61] and [70] for two different speeds: $\omega_{driver} = \omega_{driven} = 62.8\ rad/s$, and $\omega_{driver} = \omega_{driven} = 22.6\ rad/s$. For that, the belt is tensioned initially by moving the pulleys slightly apart from each other until an initial tension of $T_0 = 310\ N$ is reached. Then the belt drive is accelerated until the pulleys reach an angular velocity $\omega_{driver} = \omega_{driven}$. For the remaining simulation, the angular speed of the driver pulley is kept constant while a torque is applied on the driven pulley. Due to the difference in tension between the tight- and slack-side of the belt, an angular speed loss between the driver and driven pulley occurs. This speed loss is measured as $\Delta\omega = \omega_{driver} - \omega_{driven}$ and plotted for various torques in Figure 6-6 and Figure 6-7.

The analytical angular speed loss in Figure 6-6 and Figure 6-7 is defined as [70]

$$\Delta\omega = \left(1 - \frac{2RT_0 - M_p + 2Rk}{2RT_0 + M_p + 2Rk}\right)\omega_{driver} \tag{6.3}$$

where k is the axial stiffness per unit lenght of the belt. It should be noted that the analytical solution neglects the shear deflection and radial compliance. The numerical data by Čepon et. al. [61] is obtained from a belt drive model where deformation of the belt is described using the absolute nodal coordinate formulation [18, 19]. Also in this model shear deflection is neglected.

Figure 6-6 and Figure 6-7 show clearly that the new belt drive model provides a better angular speed loss prediction than the numerical and analytical data found in the literature. However, a clear difference between the experimental data and the numerical results of the new model exists. This difference is mainly due to the tangential deformation of the belt-rubber layer, which is not accounted for in the new belt drive model. The difference becomes even greater at higher torque values. However, shear deformation can be included if the beam elements in the model are replaced by other more appropriate type of elements.

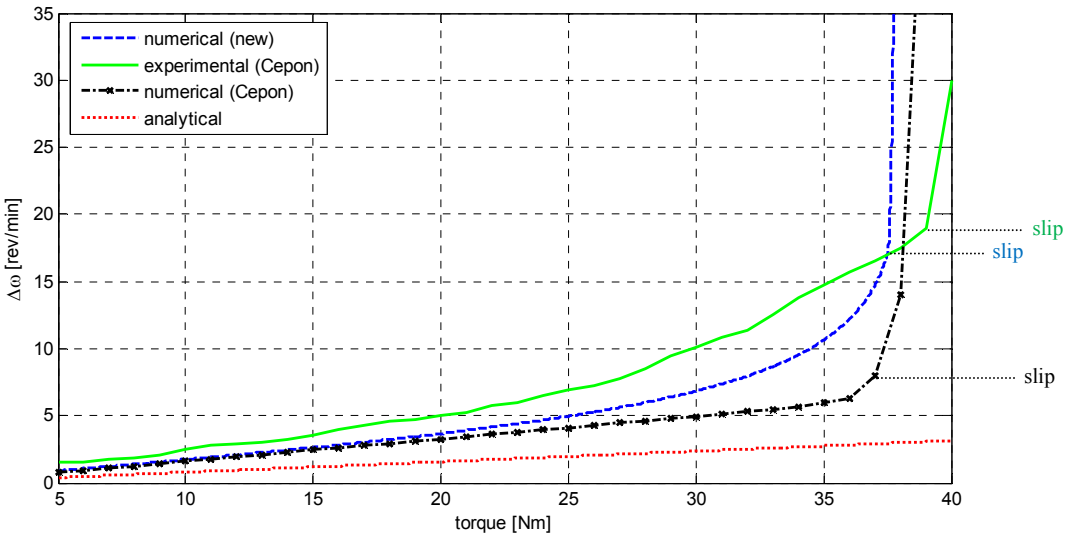

Figure 6-6: Angular speed loss between driver and driven pulley
($\omega_{driver} = 62.8\ rad/s, \quad T_0 = 310\ N$).

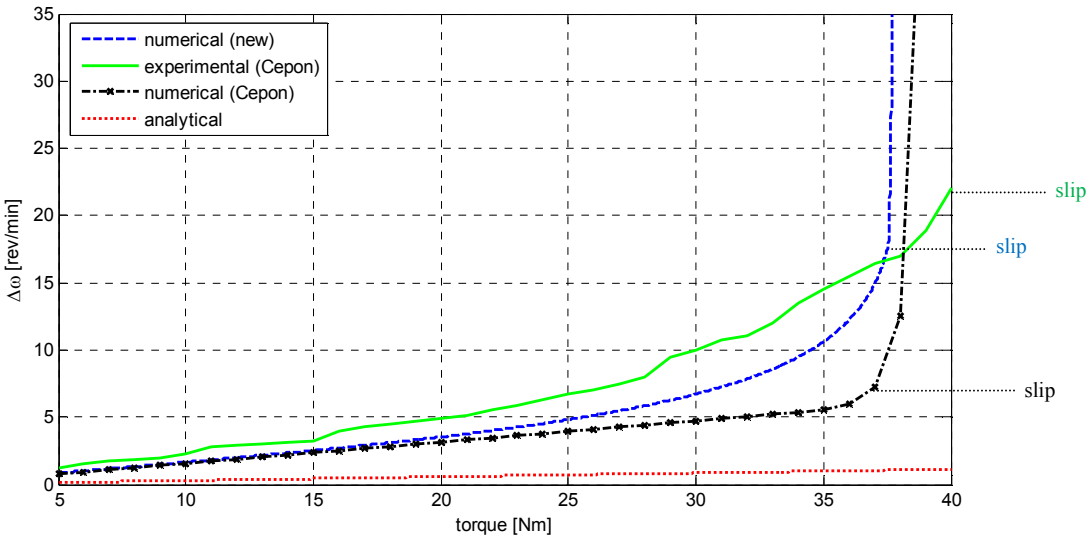

Figure 6-7: Angular speed loss between driver and driven pulley
($\omega_{driver} = 22.6\ rad/s, \quad T_0 = 310\ N$).

6.6 Discussion

This chapter shows the usefulness of the new power transmission belt concept on a two pulley-belt drive system. First, the characteristic of a stationary FE mesh in combination with a belt drive is visualized. Then, the capabilities of the new belt drive model to predict angular speed loss is presented. For validation, numerical results from the new model are compared against experimental, numerical, and analytical data that are provided in [61] and [70]. The validation showed that the new model, in combination with the given contact-friction model, can represent the angular speed loss between the driver and driven pulley relatively well.

For the sake of completeness, it should be mentioned that the new model lacks the capability of adjusting its stiffness to changing operational conditions. This inability results from the linear characteristic of the new belt drive model; i.e., mass and stiffness matrix are derived for a specific operational condition and remain constant during a simulation. Hence, an increasing torque does not change the stiffness of the belt and consequently its transversal vibration. The change in the stiffness can only be captured with a non-linear FE model. However, this research focuses only on deformable bodies whose underlying FE model is linear.

So far, the effective use of the *flowing material* concept has been shown only on a simple string model and a more complex belt drive model. However, the new concept is not limited to these examples and can be applied to even more complex systems, as it is shown in the next chapter.

7. PNEUMATIC TIRE

Many highly comprehensive linear and non-linear tire models have been developed for investigating handling, ride performance, and design. They range from analytical based tire models with few generalized coordinates to sophisticated finite element based models. While analytical tire models are used predominately in multibody simulations due to their computational efficiency, FE tire models are used for static, steady-state, or modal analysis. FE tire models are not suitable for multibody simulation purposes due to their large number of degrees-of-freedom. In order to make any multibody dynamic simulation possible, these tire models need to be reduced in their number of DoF. One approach are the component mode synthesis reduction methods, where the nodes of the tire are divided into free and contact nodes. The contact nodes are usually located at the patch and along the rim. By truncating the modes of the free nodes, the total DoF of the model can be reduced. However, due to the roll and varying applied loads, contact nodes may leave the contact area. This issue is similar to a moving string with varying boundaries or a power transmission belt rolling over pulleys, as presented in the previous chapters. Again, the problem can be resolved with the concept of *flowing material*. The implementation of the *flowing material* on a reduced FE tire is the main focus of this chapter.

This chapter starts with a literature review of previous tire models and then introduces the pneumatic tire as an FE model. After that, it describes the equations of motion of the tire model with absolute nodal acceleration, followed by nodal

accelerations relative to the tire fixed frame. Once these equations are established, they are extended with the *flowing material* concept.

7.1 Previous tire models

Studies of static and dynamic properties of tires date back almost a century [24]. Tires have been studied for their cornering characteristics and ride comfort, and more recently for their noise emission. Many tire models have been developed with the focus on these three particular characteristics. They differ in their approaches, level of complexity, and as a result, in computational effort. A good and short history on tire models until 1980 can be found in [25]. Since then many more tire models have been developed with different grades of complexity. They can be categorized into four groups based on their complexity, as shown in Figure 7-1.

The first group includes analytically based models that are aimed at computational efficiency. These models rely heavily on empirical data for the tire-road slip properties, thereby enabling accurate slip characteristics for a particular condition. On the other hand, the representation of the actual physical structure of a tire is very simplified. Examples of analytically based models are the HSRI by Dugoff and Segel [26], the U-of-A tire models by Gim and Nikravesh [25], and the Magic Formula by Bakker and Pacejka [27]. While analytical models are perfectly suited for steady-state (combined) slip simulation, their lack in representing the physical characteristics of a tire prevents them for use in applications that require higher frequency responses, such as

rolling over obstacles. Also, in situations where the tire may come to a full stop and reverse its direction, it can become difficult for some of these models to perform properly.

The second group includes models that are based on mechanical components. The complexity of these components can vary significantly, depending on the application. Most of the models consist of an elastic string, beam, or ring, which represents the tread, attached to an elastic foundation that is the sidewall. For example, Eichler [28] created a flexible I-ring belt model, where the belt is represented by mass points that are connected to each other and the rim through a collection of springs and dampers. Other models represent the belt as a rigid ring that is elastically suspended with respect to the rim for all six degrees-of-freedom. Furthermore they might include springs that connect the ring to the contact patch for a better representation of the total tire stiffness. For example, the rigid ring models by Bruni at el. [29], or by Allison and Sharp [30], or the more recently developed MF-SWIFT model by Pacejka et al. [31]. While the tire models belonging to this group can produce results quickly and computationally efficient, they need an extensive amount of experiments to obtain the properties of the mechanical components. The other drawback of these tire models is their accuracy when it comes to higher frequency response. This makes these tires only valid for a limited range of applications.

The third group consists of hybrid models that are basically a bridge between the mechanical component-based models and the FE tire models. Hybrid models are more physically based systems; i.e., their mechanical structure is closer to a real tire and, hence, includes more degrees-of-freedom, but avoids the high fidelity of FE models. Rolling over short wavelength obstacles, such as a cleat, can be captured with these models. An

example of such tire models is the FTire by Gipser [32]. The model can be separated into two parts: the flexible belt that describes tire's structural stiffness, damping, and inertia properties; and the tread model that represents the tire-road contact and computes the contact pressure distribution and friction forces. The belt consists of several segments that are mutually connected through springs. Friction functions are used to distinguish between sticking and sliding friction. Additionally a thermal and wear model is included. Another hybrid based tire model can be found in the RMOD-K system [33]. Here the belt structure is modeled with finite elements and is connected to the rim via a membrane. The membrane itself is a simplified sidewall model that considers inflation pressure. Road contact is realized through an additional sensor layer that envelops the belt structure. At the sensor points, the normal and frictional forces are calculated. Temperature and contact pressure dependent friction models are included that allow both adhesion and sliding of the sensor points.

The fourth and last group is comprised of FE based models with the highest grade of complexity. Unlike the previous models, the finite element tire models are capable of modeling the tire in much greater detail. Furthermore, geometric and material non-linearities can be captured. The first numerical simulations with FE based tire models date back as early as the 70's [34]. Today the tire industry uses FE models during development processes with focus on steady-state rolling and vibration analysis [35-37]. The use of explicit finite element programs, such as LS-DYNA3D, allows even performing transient dynamic analysis with full scale FE tire models [38], but at an

extreme computational expense. Acoustic analysis has become another application for these high-resolution models [39].

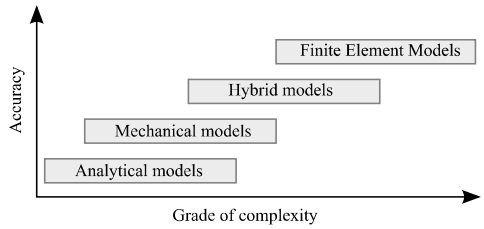

Figure 7-1: Accuracy vs. complexity for different tire model groups.

An overview of these models reveals that each group is equally important in the performance evaluation of a tire. While empirically based models are better suited to investigate the effect of changing performance parameters on out-of-plane cornering forces, slip angle changes, self-aligning torque, lateral deformations, and stiffness, the more complex and physically based models are better qualified to examine the effects of the change of physical parameters, such as material properties and cross section contour.

Looking from a different perspective, it is obvious that the analytical and mechanical based models are best suited for multibody simulation, due to their computational efficiency. Vehicle simulations can have a relative long simulation time span that can range from several seconds to few minutes. Also, these simulations have to be repeated several times; e.g., due to parameter identification of vehicle components. It is obvious that the calculation time of these simulations should be kept as short as possible, especially for hardware-in-the-loop test, where real time simulation is required. For that reason analytical and mechanical based tire models are often preferred in vehicle dynamics. However, with increasing demand on simulation details and advancements in computational performance, more accurate tire models, such as the hybrid models, find

their way into multibody simulation. An apparent question remains whether finite element based models could be adopted for multibody dynamic simulations as well. Although these models serve a valuable purpose in the design phase of a tire, they are not suitable for multibody simulation purposes in their current state. Their high-resolution leads to thousands of degrees-of-freedom, which make a multibody simulation almost impossible, even on today's high performance computers using several parallel processors. Only a reduction in their number of DoF would make a multibody simulation feasible. This chapter proofs that such a reduction is possible without restricting the model in its applications.

7.2 Finite element tire model

In most high-resolution wheel-tire models, the wheel is considered to be non-deformable (rigid body) and the tire deformable. A reference frame is attached to the wheel with its origin at the mass center of the assembly, as shown in Figure 7-2. In this figure only some typical nodes on the periphery are shown. We assume that the high-resolution FE wheel-tire model provides mass and stiffness matrices in the following form:

$$\mathbf{M}_{FE} = \left[\begin{array}{cc:c} \mathbf{M}^{rr} & \mathbf{0} & \mathbf{0} \\ \mathbf{0} & \mathbf{M}^{\theta\theta} & \mathbf{0} \\ \hdashline \mathbf{0} & \mathbf{0} & \mathbf{M} \end{array}\right], \quad \mathbf{K}_{FE} = \left[\begin{array}{cc:c} \mathbf{K}^{rr} & \mathbf{K}^{r\theta} & \mathbf{K}^{r} \\ \mathbf{K}^{r\theta^{\mathrm{T}}} & \mathbf{K}^{\theta\theta} & \mathbf{K}^{\theta} \\ \hdashline \mathbf{K}^{r^{\mathrm{T}}} & \mathbf{K}^{\theta^{\mathrm{T}}} & \mathbf{K} \end{array}\right] \tag{7.1}$$

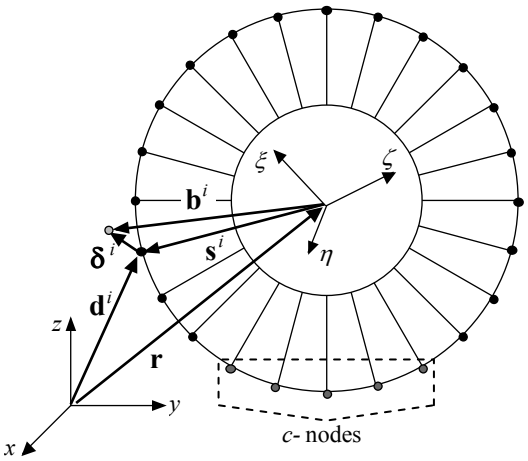

Figure 7-2: A conceptual FE wheel-tire model.

where the superscripts r and θ refer to three translational and three rotational coordinates of the wheel. The sub-matrices $\mathbf{M}^{rr} = m\mathbf{I}$ and $\mathbf{M}^{\theta\theta}$ represent the mass and rotational inertia matrices of the wheel. It is further assumed that the tire is attached to the wheel along the bead, and the mass matrix is diagonal. For reasons of clarity and readability, damping terms are excluded from the equations—such terms could simply be included in any of the equations.

For an array of deflections, $\boldsymbol{\delta}$, the stiffness matrix provides a force array as

$$\begin{Bmatrix} \mathbf{f}_K^r \\ \mathbf{n}_K^\theta \\ \mathbf{f}_K \end{Bmatrix} = \begin{Bmatrix} \mathbf{K}^r\boldsymbol{\delta} \\ \mathbf{K}^\theta\boldsymbol{\delta} \\ \mathbf{K}\boldsymbol{\delta} \end{Bmatrix} \tag{7.2}$$

where **f** represents a force (or a force array), and **n** represents a moment. Note that there is no deformation associated with the six degrees-of-freedom of the wheel with respect to the wheel-fixed frame.

The equations of motion for a wheel-tire can be expressed as

$$\left[\begin{array}{cc:c} \mathbf{M}^{rr} & \mathbf{0} & \mathbf{0} \\ \mathbf{0} & \mathbf{M}^{\theta\theta} & \mathbf{0} \\ \hdashline \mathbf{0} & \mathbf{0} & \mathbf{M} \end{array}\right]\left\{\begin{array}{c} \ddot{\mathbf{r}} \\ \dot{\boldsymbol{\omega}} \\ \ddot{\mathbf{d}} \end{array}\right\}=\left\{\begin{array}{c} \mathbf{f}^{r}-\mathbf{f}_{K}^{r} \\ \mathbf{n}^{\theta}-\tilde{\boldsymbol{\omega}}\mathbf{M}^{\theta\theta}\boldsymbol{\omega}-\mathbf{n}_{K}^{\theta} \\ \mathbf{f}-\mathbf{f}_{K} \end{array}\right\} \tag{7.3}$$

In this equation $\ddot{\mathbf{r}}$ and $\dot{\boldsymbol{\omega}}$ denote the translational and rotational accelerations of the wheel, $\ddot{\mathbf{d}}$ is the array of absolute accelerations of the nodes, $\boldsymbol{\omega}$ is the angular velocity of the wheel, $\mathbf{f}^{r}$, $\mathbf{n}^{\theta}$, and $\mathbf{f}$ denote external forces and moments that may act on the wheel and the nodes.

7.3 Tire-ground contact

In any tire-ground contact scenario, some of the nodes would be in contact with the ground. Ground contact can be incorporated via the method of Lagrange multipliers; i.e., nodes on the ground are constrained in vertical direction so that they cannot penetrate the ground. If we consider a non-rotating tire whose load is changing over time, then some nodes from the contact patch leave the ground and some other nodes enter the contact area. Three possible contact scenarios are illustrated in Figure 7-3. Modeling the transition of some nodes into and out of the contact patch requires the boundary conditions, or the constraints, in the equations of motion to be adjusted accordingly. In order to handle this issue, the nodes are divided into two groups: those that may come in contact with the ground, designated again as *c*- or contact nodes; and those that are free, designated as *f*-nodes. The number of *c*-nodes depends on the simulation scenario. The contact nodes need to cover the largest possible size for the contact patch when the tire is under a possible maximum load. Note again that a *c*-node is only a candidate to come in contact with the ground.

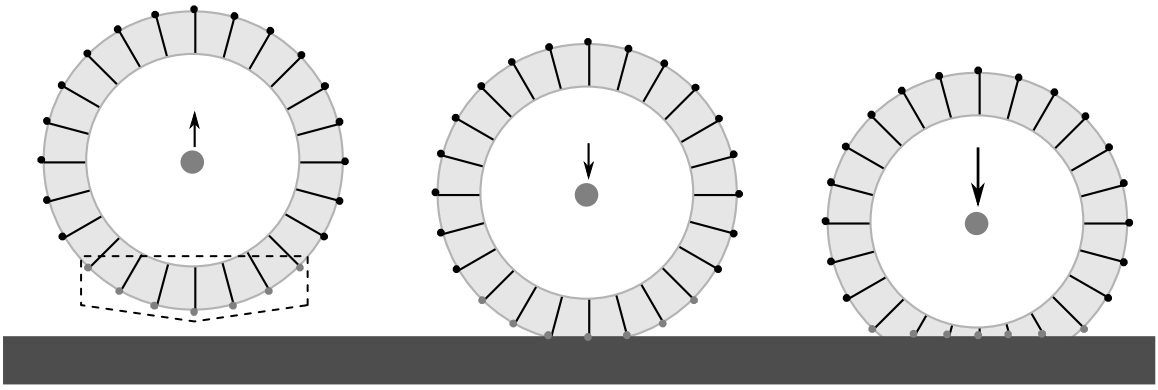

Figure 7-3: Three possible scenarios for the contact nodes and the ground.

In a next step, let us consider the tire to roll over the ground as well. In a rolling scenario, *c*-nodes will leave the contact patch and *f*-nodes will become into contact with the ground after a certain period of time. However, this would violate the boundary condition requirements; i.e., only *c*-nodes are allowed to be in contact with the ground. In order to avoid this issue, a solution can be found by realizing that the tire has an orientation invariant characteristic, which is due to its symmetric structure about the wheel axis. The orientation invariant characteristic defines the mass and stiffness matrices of a tire not to be affected by any rotational transformation about the wheel axis. When the nodes rotate about the wheel axis, and if we introduce a new set of nodes in the vacated spaces of the old nodes, as shown in Figure 7-4, the same mass and stiffness matrices can be used. Consequently, the same mode shapes can be applied to the new nodes. In other words, the mass and stiffness matrices, and the mode shapes can remain with a non-rotating frame, but the mass points "flow" through them. This idea is

equivalent to the concept of *flowing material* that has been introduced in the string and belt drive model before.

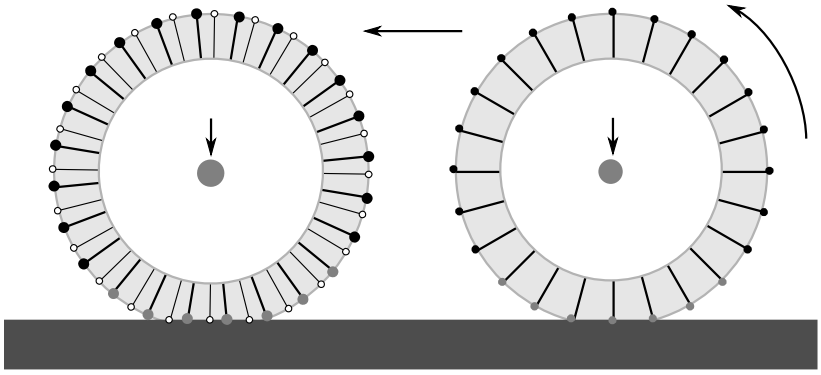

Figure 7-4: Rolling tire with new set of nodes (white) in the vacated space of the old nodes.

In the following sections the governing equations of motion for the finite element tire are represented in three different forms. In the first form the equations are represented in terms of the absolute nodal accelerations. In the second form these equations are shown with accelerations that are relative to the body-fixed frame. The third form introduces the equations of motions with modal accelerations and the concept of *flowing material*.

7.4 Absolute nodal accelerations

With the partitioning of the nodes into *c*- and *f*-sets, the mass and stiffness sub-matrices are accordingly partitioned:

$$\mathbf{M} = \begin{bmatrix} \mathbf{M}^{ff} & \mathbf{0} \\ \mathbf{0} & \mathbf{M}^{cc} \end{bmatrix}, \quad \mathbf{K} = \begin{bmatrix} \mathbf{K}^{ff} & \mathbf{K}^{fc} \\ \mathbf{K}^{cf} & \mathbf{K}^{cc} \end{bmatrix} \tag{7.4}$$

Then, the equations of motion are expressed as:

$$\left[\begin{array}{ccc:cc:c} \mathbf{M}^{rr} & \mathbf{0} & \mathbf{0} & \mathbf{0} & \mathbf{0} \\ \mathbf{0} & \mathbf{M}^{\theta\theta} & \mathbf{0} & \mathbf{0} & \mathbf{0} \\ \hdashline \mathbf{0} & \mathbf{0} & \mathbf{M}^{ff} & \mathbf{0} & \mathbf{0} \\ \mathbf{0} & \mathbf{0} & \mathbf{0} & \mathbf{M}^{cc} & -\mathbf{D}^{\mathrm{T}} \\ \hdashline \mathbf{0} & \mathbf{0} & \mathbf{0} & \mathbf{D} & \mathbf{0} \end{array}\right] \left\{\begin{array}{c} \ddot{\mathbf{r}} \\ \dot{\boldsymbol{\omega}} \\ \hdashline \ddot{\mathbf{d}}^{f} \\ \ddot{\mathbf{d}}^{c} \\ \hdashline \boldsymbol{\lambda} \end{array}\right\} = \left\{\begin{array}{c} \mathbf{f}^{r} - \mathbf{f}_{K}^{r} \\ \hdashline \mathbf{n}^{\theta} - \tilde{\boldsymbol{\omega}}\mathbf{M}^{\theta\theta}\boldsymbol{\omega} - \mathbf{n}_{K}^{\theta} \\ \hdashline \mathbf{f}^{f} - \mathbf{f}_{K}^{f} \\ \mathbf{f}^{c} - \mathbf{f}_{K}^{c} \\ \hdashline \boldsymbol{\gamma} \end{array}\right\} \tag{7.5}$$

The constraints on the contact nodes are included in these equations of motion through the use of Lagrange multipliers, where $\mathbf{D}$ is the Jacobian matrix of the constraints and $\boldsymbol{\gamma}$ is the array of quadratic velocity terms in the acceleration constraints. Note that not all of the *c*-nodes are constrained—only those that are in contact with the ground. In most cases, for simple contact with the ground, the Jacobian is an identity matrix and $\boldsymbol{\gamma}$ is a zero array.

In order to simplify the notation in the upcoming equations, the nodal mass matrices are moved from the coefficient matrix to the force array as:

$$\left[\begin{array}{ccc:cc:c} \mathbf{M}^{rr} & \mathbf{0} & \mathbf{0} & \mathbf{0} & \mathbf{0} \\ \mathbf{0} & \mathbf{M}^{\theta\theta} & \mathbf{0} & \mathbf{0} & \mathbf{0} \\ \hdashline \mathbf{0} & \mathbf{0} & \bar{\mathbf{I}} & \mathbf{0} & \mathbf{0} \\ \mathbf{0} & \mathbf{0} & \mathbf{0} & \bar{\mathbf{I}} & -\mathbf{D}^{\mathrm{T}} \\ \hdashline \mathbf{0} & \mathbf{0} & \mathbf{0} & \mathbf{D} & \mathbf{0} \end{array}\right] \left\{\begin{array}{c} \ddot{\mathbf{r}} \\ \dot{\boldsymbol{\omega}} \\ \hdashline \ddot{\mathbf{d}}^{f} \\ \ddot{\mathbf{d}}^{c} \\ \hdashline \boldsymbol{\lambda} \end{array}\right\} = \left\{\begin{array}{c} \mathbf{f}^{r} - \mathbf{f}_{K}^{r} \\ \hdashline \mathbf{n}^{\theta} - \tilde{\boldsymbol{\omega}}\mathbf{M}^{\theta\theta}\boldsymbol{\omega} - \mathbf{n}_{K}^{\theta} \\ \hdashline \mathbf{M}^{ff^{-1}}(\mathbf{f}^{f} - \mathbf{f}_{K}^{f}) \\ \mathbf{M}^{cc^{-1}}(\mathbf{f}^{c} - \mathbf{f}_{K}^{c}) \\ \hdashline \boldsymbol{\gamma} \end{array}\right\} \tag{7.6}$$

There is no need to replace $-\mathbf{D}^{\mathrm{T}}$ with $-\mathbf{M}^{bb^{-1}}\mathbf{D}^{\mathrm{T}}$ because the Lagrange multipliers will adjust their values to compensate for the difference.

7.5 Relative nodal acceleration

The absolute position of a typical node can be expressed in term of its deflection as

$$\mathbf{d}^{i} = \mathbf{r} + \mathbf{s}^{i} + \boldsymbol{\delta}^{i} \tag{7.7}$$

where $\mathbf{s}^i$ represent the nodal position vectors with respect to the wheel mass center in the undeformed states. The time derivatives of Eq. (7.7) is written as

$$\begin{aligned}\dot{\mathbf{d}}^i &= \dot{\mathbf{r}} - \tilde{\mathbf{s}}^i\boldsymbol{\omega} + \dot{\boldsymbol{\delta}}^i \\ \ddot{\mathbf{d}}^i &= \ddot{\mathbf{r}} - \tilde{\mathbf{s}}^i\dot{\boldsymbol{\omega}} + \ddot{\boldsymbol{\delta}}^i + \tilde{\boldsymbol{\omega}}\tilde{\boldsymbol{\omega}}\mathbf{s}^i\end{aligned} \tag{7.8}$$

For all of the nodes, the acceleration equations can be assembled as

$$\ddot{\mathbf{d}} = \begin{bmatrix}\hat{\mathbf{I}} & -\hat{\tilde{\mathbf{s}}} & \bar{\mathbf{I}}\end{bmatrix}\begin{Bmatrix}\ddot{\mathbf{r}} \\ \dot{\boldsymbol{\omega}} \\ \ddot{\boldsymbol{\delta}}\end{Bmatrix} + \mathbf{w} \tag{7.9}$$

where $\mathbf{w} = \bar{\tilde{\boldsymbol{\omega}}}\bar{\tilde{\boldsymbol{\omega}}}\mathbf{s}$. The equations of motion in Eq. (7.5) can be transformed using Eq. (7.9):

$$\left[\begin{array}{cc|c|c|c} \mathbf{M}^{rr} & \mathbf{0} & \mathbf{0} & \mathbf{0} & \mathbf{0} \\ \mathbf{0} & \mathbf{M}^{\theta\theta} & \mathbf{0} & \mathbf{0} & \mathbf{0} \\ \hline \hat{\mathbf{I}} & -\hat{\tilde{\mathbf{s}}}^f & \bar{\mathbf{I}} & \mathbf{0} & \mathbf{0} \\ \hat{\mathbf{I}} & -\hat{\tilde{\mathbf{s}}}^c & \mathbf{0} & \bar{\mathbf{I}} & -\mathbf{D}^{\mathrm{T}} \\ \hline \mathbf{D}\hat{\mathbf{I}} & -\mathbf{D}\hat{\tilde{\mathbf{s}}}^c & \mathbf{0} & \mathbf{D} & \mathbf{0} \end{array}\right]\left\{\begin{array}{c}\ddot{\mathbf{r}} \\ \dot{\boldsymbol{\omega}} \\ \hline \bar{\ddot{\boldsymbol{\delta}}}^f \\ \ddot{\boldsymbol{\delta}}^c \\ \hline \boldsymbol{\lambda}\end{array}\right\} = \left\{\begin{array}{c}\mathbf{f}^r - \mathbf{f}_K^r \\ \mathbf{n}^\theta - \tilde{\boldsymbol{\omega}}\mathbf{M}^{\theta\theta}\boldsymbol{\omega} - \mathbf{n}_K^\theta \\ \hline \mathbf{M}^{ff^{-1}}(\mathbf{f}^f - \mathbf{f}_K^f) - \mathbf{w}^f \\ \mathbf{M}^{cc^{-1}}(\mathbf{f}^c - \mathbf{f}_K^c) - \mathbf{w}^c \\ \hline \boldsymbol{\gamma} - \mathbf{D}\mathbf{w}^c \end{array}\right\} \tag{7.10}$$

7.6 Modal accelerations

The normal mode shapes of free and contact nodes are represented by matrix $\boldsymbol{\Psi}^f$ and $\boldsymbol{\Psi}^c$. With these mode shapes the transformation between the modal and nodal coordinates for both sets of nodes is expressed as

$$\begin{Bmatrix}\boldsymbol{\delta}^f \\ \boldsymbol{\delta}^c\end{Bmatrix} = \begin{bmatrix}\boldsymbol{\Psi}^f & \boldsymbol{\Psi}_s^c \\ \mathbf{0} & \boldsymbol{\Psi}^c\end{bmatrix}\begin{Bmatrix}\mathbf{z}^f \\ \mathbf{z}^c\end{Bmatrix} \tag{7.11}$$

where $\boldsymbol{\Psi}_s^c = \boldsymbol{\Psi}_s\boldsymbol{\Psi}^c$ and $\boldsymbol{\Psi}_s$ are the static mode shapes of the *f*-nodes. Note, that *c*-degrees-of-freedom will not be truncated since they could be constrained, and therefore,

there is no need for static modes for these nodes. Matrices $\boldsymbol{\Psi}^f$, $\boldsymbol{\Psi}^c$, and $\boldsymbol{\Psi}_s$ are obtained as it was described in Section 3.2 and 3.3.

If we consider that the mode shapes do not rotate with the body-fixed frame, the time derivatives of Eq. (7.11) can be obtained by using the material derivative

$$\frac{d}{dt} = \frac{\partial}{\partial t} + \dot{\theta}\frac{\partial}{\partial \theta} \tag{7.12}$$

where θ is the rotational coordinate about the wheel axis and $\dot{\theta}$ is the rotational speed. Also, if we assume that the wheel axis coincides with the η-axis of the wheel-fixed frame, we have $\dot{\theta} = \boldsymbol{\eta}^{\mathrm{T}}\boldsymbol{\omega}$ and $\ddot{\theta} = \boldsymbol{\eta}^{\mathrm{T}}\dot{\boldsymbol{\omega}}$. The first and second time derivative of Eq. (7.11) can then be expressed as

$$\begin{Bmatrix} \dot{\boldsymbol{\delta}}^f \\ \dot{\boldsymbol{\delta}}^c \end{Bmatrix} = \begin{bmatrix} \boldsymbol{\Psi}^f & \boldsymbol{\Psi}_s^c \\ \mathbf{0} & \boldsymbol{\Psi}^c \end{bmatrix} \begin{Bmatrix} \dot{\mathbf{z}}^f \\ \dot{\mathbf{z}}^c \end{Bmatrix} + \begin{bmatrix} \mathbf{B}^f \\ \mathbf{B}^c \end{bmatrix} \boldsymbol{\omega} \tag{7.13}$$

$$\begin{Bmatrix} \ddot{\boldsymbol{\delta}}^f \\ \ddot{\boldsymbol{\delta}}^c \end{Bmatrix} = \begin{bmatrix} \boldsymbol{\Psi}^f & \boldsymbol{\Psi}_s^c \\ \mathbf{0} & \boldsymbol{\Psi}^c \end{bmatrix} \begin{Bmatrix} \ddot{\mathbf{z}}^f \\ \ddot{\mathbf{z}}^c \end{Bmatrix} + \begin{bmatrix} \mathbf{B}^f \\ \mathbf{B}^c \end{bmatrix} \dot{\boldsymbol{\omega}} + \begin{Bmatrix} \mathbf{c}^f \\ \mathbf{c}^c \end{Bmatrix} \tag{7.14}$$

where

$$\begin{bmatrix} \mathbf{B}^f \\ \mathbf{B}^c \end{bmatrix} = \begin{bmatrix} \boldsymbol{\Psi}^f & \boldsymbol{\Psi}_s^c \\ \mathbf{0} & \boldsymbol{\Psi}^c \end{bmatrix}_{,\theta} \begin{Bmatrix} \mathbf{z}^f \\ \mathbf{z}^c \end{Bmatrix} \boldsymbol{\eta}^{\mathrm{T}} \tag{7.15}$$

$$\begin{Bmatrix} \mathbf{c}^f \\ \mathbf{c}^c \end{Bmatrix} = \left(\begin{bmatrix} \boldsymbol{\Psi}^f & \boldsymbol{\Psi}_s^c \\ \mathbf{0} & \boldsymbol{\Psi}^c \end{bmatrix}_{,\theta\theta} \begin{Bmatrix} \mathbf{z}^f \\ \mathbf{z}^c \end{Bmatrix} \dot{\theta} + 2 \begin{bmatrix} \boldsymbol{\Psi}^f & \boldsymbol{\Psi}_s^c \\ \mathbf{0} & \boldsymbol{\Psi}^c \end{bmatrix}_{,\theta} \begin{Bmatrix} \dot{\mathbf{z}}^f \\ \dot{\mathbf{z}}^c \end{Bmatrix} \right) \dot{\theta} \tag{7.16}$$

In this equation $[\cdot]_{,\theta}$ and $[\cdot]_{,\theta\theta}$ represent the first and second partial derivative of the mode shapes with respect to the rotational coordinate θ about the wheel axis.

We substitute the transformations from Eqs. (7.14)-(7.16) into this Eq. (7.10), and pre-multiply the third row by $\boldsymbol{\Psi}^{f^{\mathrm{T}}}$ to obtain the equations of motion with modal accelerations:

$$\left[\begin{array}{cc|cc|c} \mathbf{M}^{rr} & \mathbf{0} & \mathbf{0} & \mathbf{0} & \mathbf{0} \\ \mathbf{0} & \mathbf{M}^{\theta\theta} & \mathbf{0} & \mathbf{0} & \mathbf{0} \\ \hline \boldsymbol{\Psi}^{f^{\mathrm{T}}}\hat{\mathbf{I}} & \boldsymbol{\Psi}^{f^{\mathrm{T}}}(\mathbf{B}^{f}-\hat{\tilde{\mathbf{s}}}^{f}) & \boldsymbol{\Psi}^{f^{\mathrm{T}}}\boldsymbol{\Psi}^{f} & \boldsymbol{\Psi}^{f^{\mathrm{T}}}\boldsymbol{\Psi}_{s}^{c} & \mathbf{0} \\ \hat{\mathbf{I}} & (\mathbf{B}^{c}-\hat{\tilde{\mathbf{s}}}^{c}) & \mathbf{0} & \boldsymbol{\Psi}^{c} & -\mathbf{D}^{\mathrm{T}} \\ \hline \mathbf{D}\hat{\mathbf{I}} & -\mathbf{D}\hat{\tilde{\mathbf{s}}}^{c} & \mathbf{0} & \mathbf{D}\boldsymbol{\Psi}^{c} & \mathbf{0} \end{array}\right] \left\{\begin{array}{c} \ddot{\mathbf{r}} \\ \dot{\boldsymbol{\omega}} \\ \hline \ddot{\mathbf{z}}^{f} \\ \ddot{\mathbf{z}}^{c} \\ \hline \boldsymbol{\lambda} \end{array}\right\} = \left\{\begin{array}{c} \mathbf{f}^{r}-\mathbf{f}_{K}^{r} \\ \mathbf{n}^{\theta}-\tilde{\boldsymbol{\omega}}\mathbf{M}^{\theta\theta}\boldsymbol{\omega}-\mathbf{n}_{K}^{\theta} \\ \hline \boldsymbol{\Psi}^{f^{\mathrm{T}}}\left(\mathbf{M}^{ff^{-1}}(\mathbf{f}^{f}-\mathbf{f}_{K}^{f})-(\mathbf{w}^{f}+\mathbf{c}^{f})\right) \\ \left(\mathbf{M}^{cc^{-1}}(\mathbf{f}^{c}-\mathbf{f}_{K}^{c})-(\mathbf{w}^{c}+\mathbf{c}^{c})\right) \\ \hline \boldsymbol{\gamma}-\mathbf{D}\mathbf{w}^{c} \end{array}\right\} \tag{7.17}$$

Now the equation is in a form that the modal coordinates associated with the *f*-nodes can be truncated in order to reduce the size of the problem. Note, that the fourth row does not need to be pre-multiplied with $\boldsymbol{\Psi}^{c^{T}}$, since $\boldsymbol{\Psi}^{c}$ is full rank.

7.7 Discussion

This chapter represents the concept of *flowing material* applied on a FE tire. In doing so, the mesh of the FE tire becomes independent of the roll about the wheel axis. Consequently, nodes that will never get into contact with the ground can be transferred into modal space. By reducing the set of normal mode shapes, the overall degrees-of-freedom of the FE tire can be reduced significantly. In the end, the FE tire becomes practical for multibody simulation purposes.

While the presented reduced FE tire is primarily useful for ride comfort analysis, it can also be beneficial for handling analysis if it is truncated appropriately. In handling analysis a full vehicle is represented as a multibody system that drives over a virtual predefined track. The simulated time span can range from several seconds to few minutes. In order to have feasible computational time, handling analysis require tire models to include only few DoF.

8. NUMERICAL SIMULATION OF A TIRE MODEL

The previous chapter introduced a new tire model for ride comfort analysis that is based on a truncated finite element model. Unlike other FE tire models, this model is suitable for multibody simulation purposes. Just as the moving string and the power transmission belt models, this new tire model includes the concept of *flowing material*. The concept of *flowing material* allows the FE mesh of the tire to remain stationary, or to translate without rotation, while the tire material rolls. Subsequently, nodes that never get into contact with the ground can be truncated, which significantly reduces the total number of degrees-of-freedom of the FE tire.

This chapter provides a cleat test simulation with the new tire model. The results of the cleat test are compared against experimental data that is provided by "Hankook Tire" [72]. In the following sections the purpose of a cleat test are described first. Then, the properties of the truncated FE tire are defined. Afterwards the results of the cleat test simulation are presented, followed by a discussion.

8.1 Cleat test

The ride comfort of a tire depends on its vibration characteristic. Hence, vibration tests of newly designed tires are a common practice in tire manufacturing. The cleat test is one useful mechanical test that can reveal vibration properties of a tire. In this test a tire is mounted on a free rotating spindle. The spindle is moved hydraulically towards a drum, which presses the tire onto the drum with a desired load, as shown in Figure 8-1. The drum itself is usually 2-3 times greater in diameter than that of the tire. The drum is

driven by an electric motor. Ideally, the tire rolls over the drum in the same way as it would roll on the road in a straight-headed vehicle. A cleat is mounted transversally on the drum that excites the tire every time it passes over. The resulting vibrations in the tire are measured through multi-axial force transducers in the spindle. Usually, vertical and longitudinal forces in the spindle are recorded that give insight to the vibrational behavior of a tire, and hence, yield information about its ride comfort.

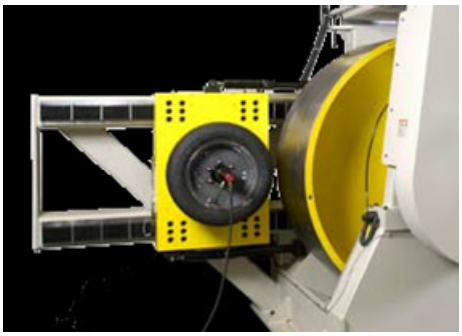

Figure 8-1: MTS Tire Rolling Resistance Measurement System [71].

8.2 Truncated finite element tire model

A new three-dimensional tire model for ride comfort has been developed based on Eq. (8.17). Here, the tire model will be referred to as *UAH-tire* (University of Arizona & Hankook - tire). The new model is based on a truck tire from the tire manufacturer "Hankook Tire" [72]. The FE truck tire is initially obtained as a high-resolution 3D ABAQUS model that consists of more than 20,000 nodes, whereby each node includes three translational DoF (over 60,000 DoF in total). Mass and stiffness matrices are extracted from the ABAQUS model under a specified load and inflation; i.e., the static nonlinearities due to the load and inflation are included in the generated matrices. Out of these matrices the necessary normal and static mode shapes and their spatial derivatives

are calculated using MATLAB. For the FE truck tire, out of the 20,000 plus nodes, 95 nodes at the contact patch area are selected as contact nodes, as shown in Figure 8-2. Then, by keeping these 95 nodes and the nodes at the rim being fixed, the normal mode shapes for the free nodes are obtained. Although this step provides thousands of modes that cover a wide frequency range, only the first 50 modes are kept — these 50 modes should represent the vibration of the tire for a frequency range from 0 to 240 Hz. In a similar way, the normal mode shapes for the contact nodes are obtained by constraining the free nodes. Here, all of the modes are kept, which cover a frequency range from 0 to 8.35 kHz. The static modes shapes are obtained by reducing the entire FE model to the set of 95 contact nodes through static condensation. With these mode shapes and their derivatives, the mass and stiffness matrices are then truncated in such a way that they conform to Eq. (8.17). As a result, a truncated FE truck tire model is obtained that contains 341 DoF in total: 6 rigid-body DoF; 3 *x* 95 DoF representing the deformation of the contact nodes; and 50 DoF representing the deformation of the free nodes. The degree-of-truncation is chosen based on the test rig data and computational requirements. Without a doubt, more modes would cover a larger frequency range and, hence, provide better results. However, the computational requirements would increase rapidly as well.

Due to reasons of confidentiality from Hankook Tire Co., geometric and material properties of the truck tire cannot be published in this work. Nevertheless, the validity of the *UAH-tire* does not change because of this, since the methodology can be used for any type of tires.

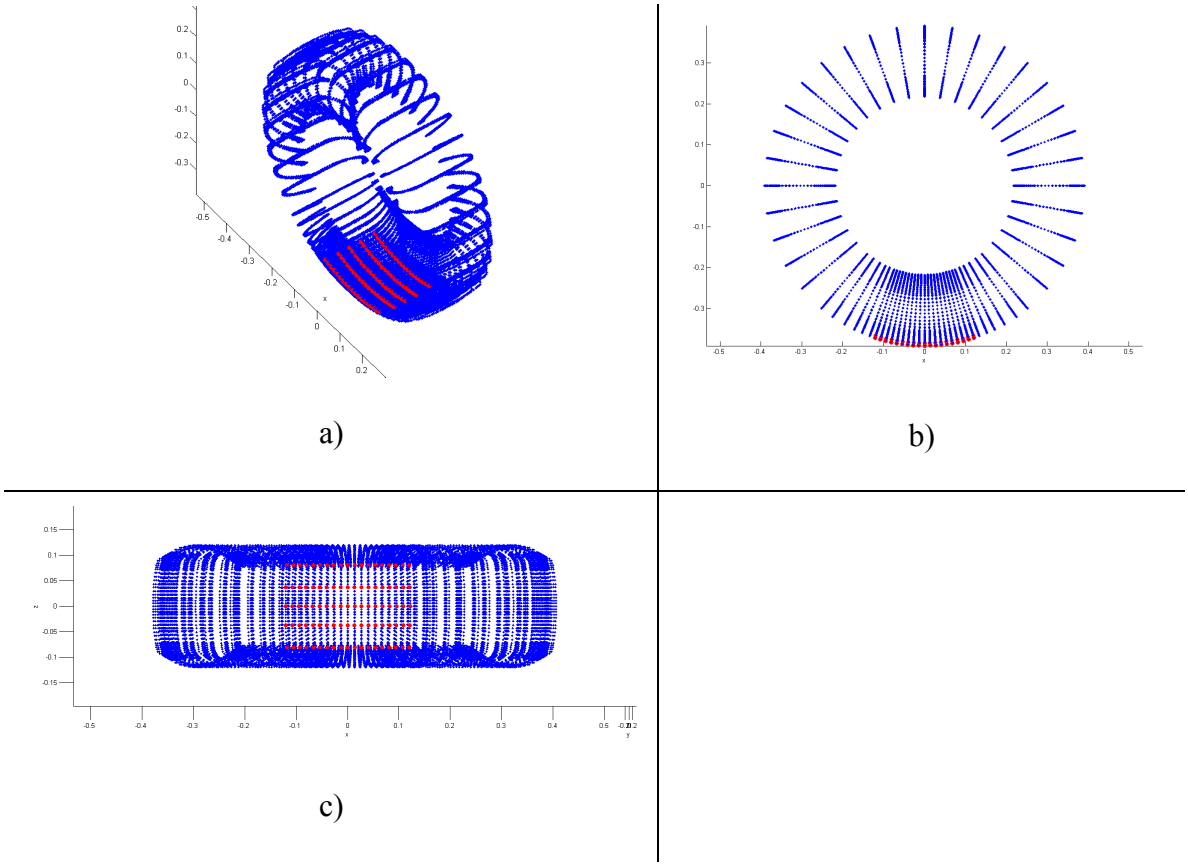

Figure 8-2: Arrangement of free (blue) and contact (red) nodes in the FE model: a) 3D-View, b) side-view, and c) bottom view.

8.3 Simulation of a cleat test

In order to validate the *UAH-tire*, a cleat test is simulated and compared to experimental test data. The test data belongs to the same type of truck tire that is used for the simulation. The cleat test simulation setup is kept close to a real cleat test installation as shown in Figure 8-3. In the setup, the tire is inflated with a pressure of 38 psi and loaded to the drum with 1,000 lb. Furthermore, a semi-circular cleat of 10 mm radius is mounted onto the drum. After preloading, the tire is accelerated until it reaches a desired speed. Once the desired speed is achieved, the vertical F_y and longitudinal F_x reaction

forces in the spindle are recorded. This test is repeated for the speeds of 20 to 100 km/h in increments of 10 km/h.

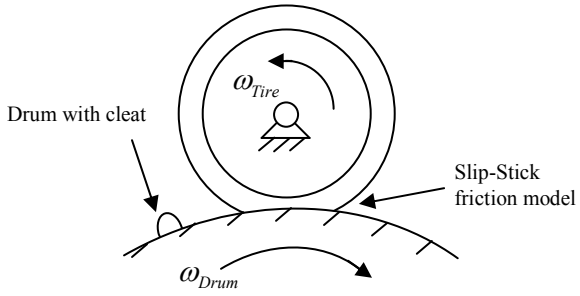

Figure 8-3: Simulation setup of the cleat test on drum.

8.3.1 Results in the time-domain

The reaction forces at the spindle from both rig testing and simulation are compared in the time-domain first. Figure 8-4 shows the vertical (F_y) and longitudinal (F_x) reaction forces at the spindle for a speed range of 20 - 100 km/h in increments of 10 km/h. Inspecting the results in the time domain reveals good agreement between the simulation and the test rig data. However, the sets of data do not match completely. Strong deviations can be observed in the longitudinal reaction forces for higher speeds. A discussion on the possible cause of these deviations is given in Section 8.4.

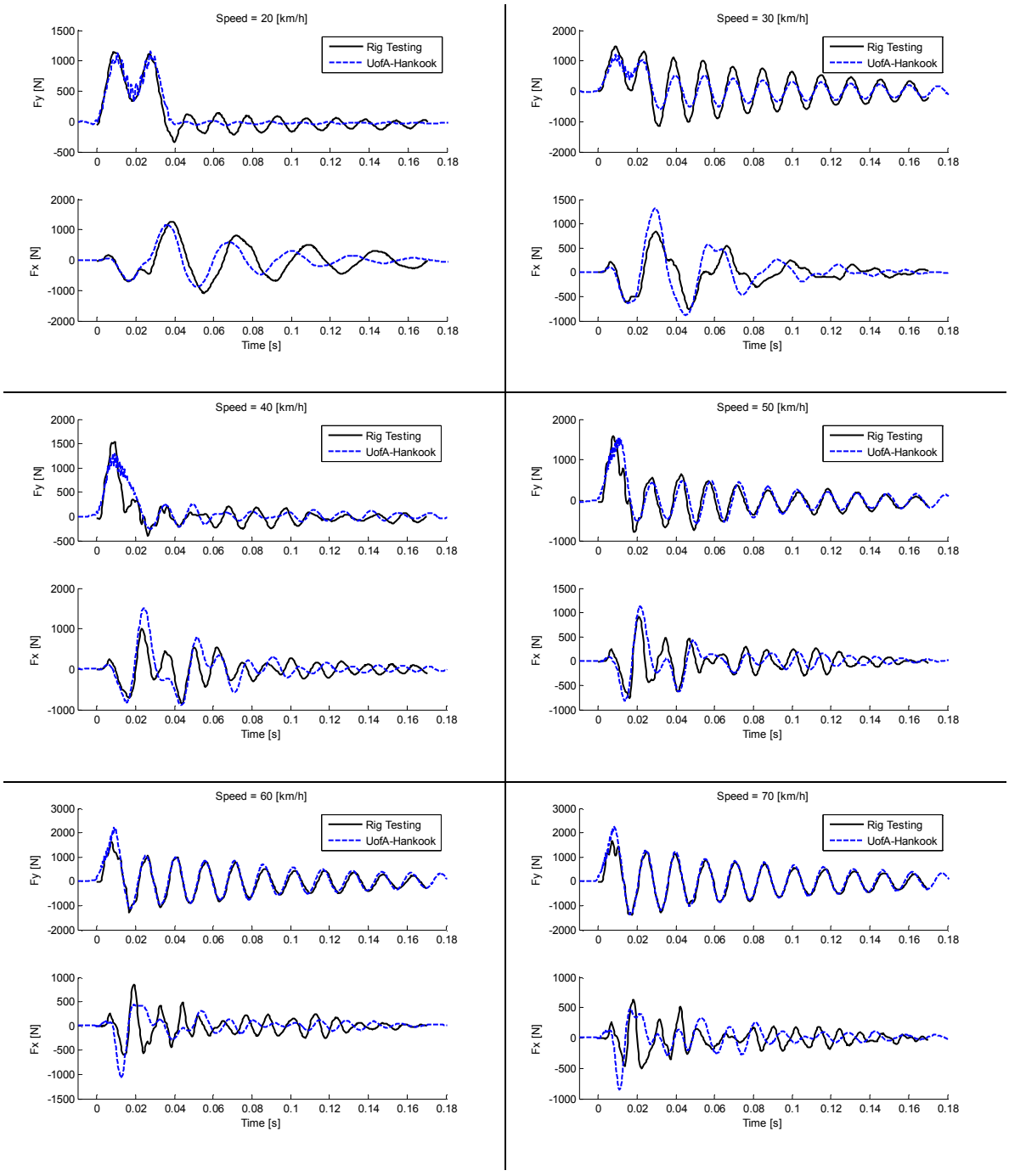

Figure 8-4: Vertical (F_y) and longitudinal (F_x) reaction forces at the spindle for various speeds in time domain.

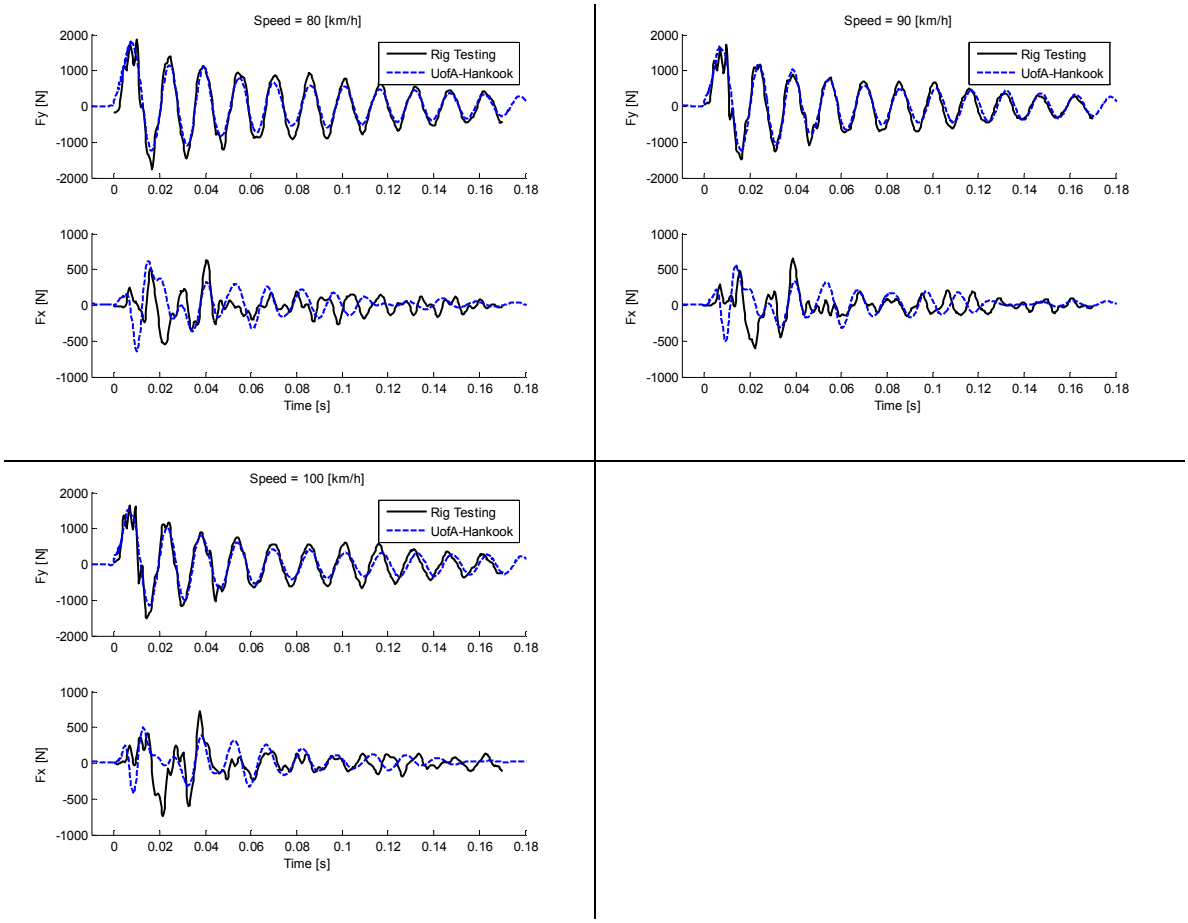

Figure 8-4 (cont.): Vertical (F_y) and longitudinal (F_x) reaction forces at the spindle for various speeds in time domain.

8.3.2 Results in the frequency-domain

To reaffirm the validity of the *UAH-tire,* the reaction forces at the spindle from both rig testing and simulation are compared in the frequency-domain as well. Figure 8-5 shows the vertical (F_y) and longitudinal (F_x) reaction forces at the spindle in the frequency domain for a speed range for 20 - 100 km/h in increments of 10 km/h. The results show that the same frequency of 64Hz in vertical direction is excited in the experimental test and in the simulation. Comparing this frequency to the mode shapes of the tire reveals that during the cleat test the 5th mode is excited the most (see Figure 8-6).

While the data of the simulation matches in general with the experimental data, some deviations in the amplitudes of the vibrations in vertical direction can be observed. Furthermore, the longitudinal forces (F_x) match at low speeds, but diverge at higher speed.

Figure 8-7 and Figure 8-8 represent the vertical (F_y) and longitudinal (F_x) reaction forces for various speeds as a contour plot. This perspective reveals a better insight into the progression of the vibration amplitude over speed. Intuitively, we would assume that the vibration amplitude increases proportional to the speed; i.e., the faster the tire rolls over the cleat, the greater would be the vibration within the tire. Instead, Figure 8-7 and Figure 8-8 indicate that vibration does not increase proportional with speed. Moreover, Figure 8-7 shows that a significant drop of vibration occurs in the tire at a speed range of 40 – 50 km/h. This drop in the vibration amplitude is represented by the simulation and the rig test at the same speed range.

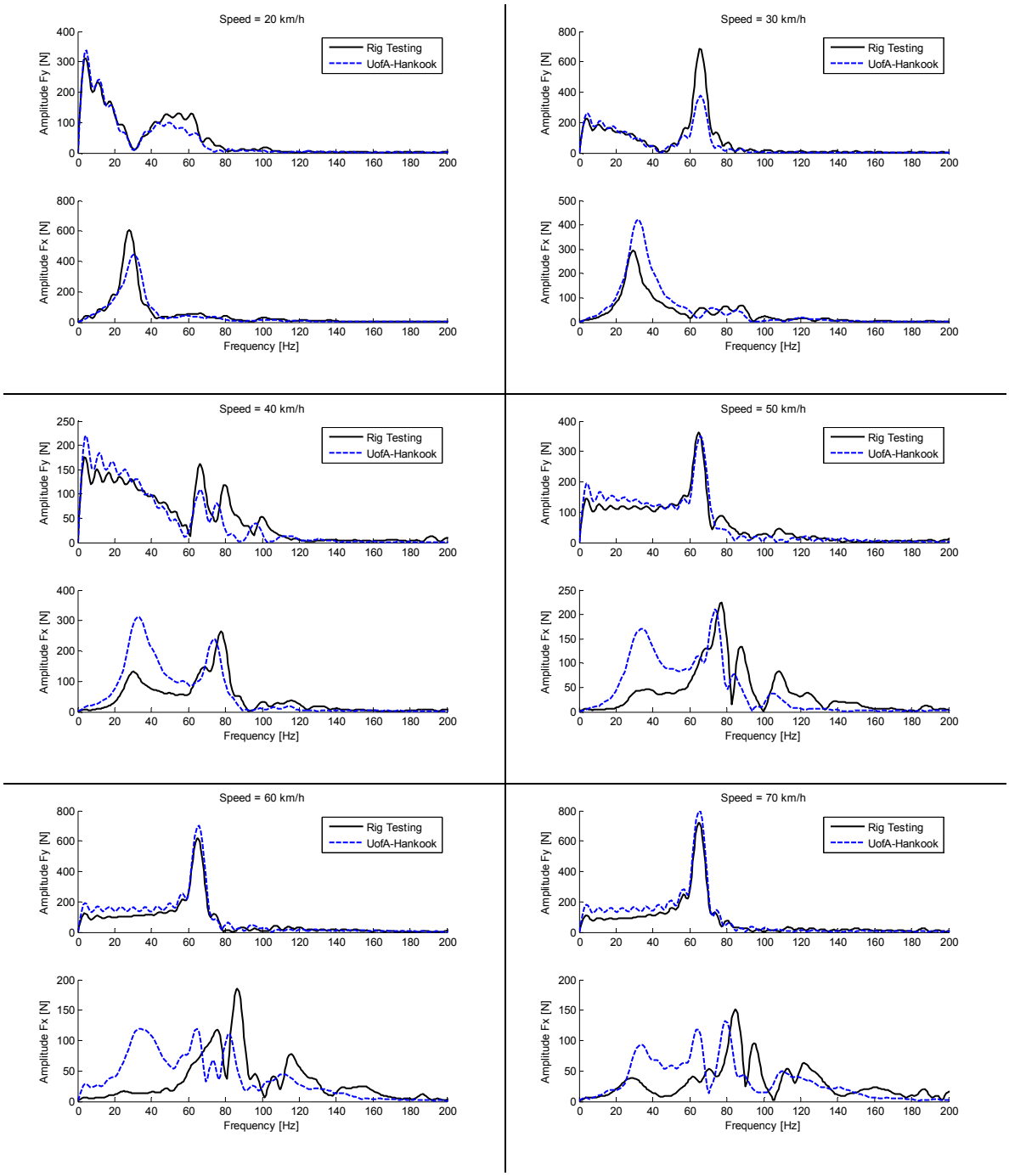

Figure 8-5: Vertical (F_y) and longitudinal (F_x) reaction forces at the spindle for various speeds in frequency domain.

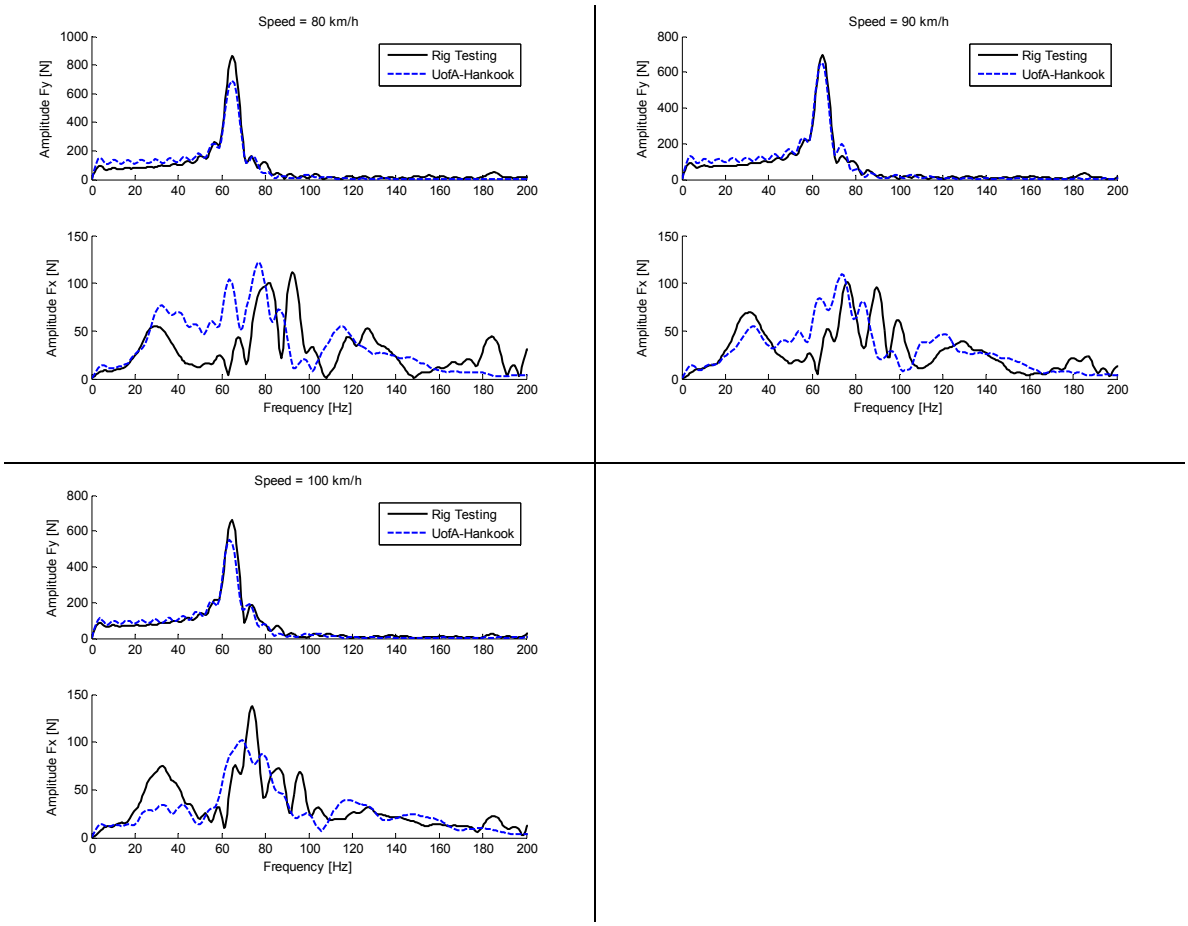

Figure 8-5 (cont.): Vertical (F_y) and longitudinal (F_x) reaction forces at the spindle for various speeds in frequency domain.

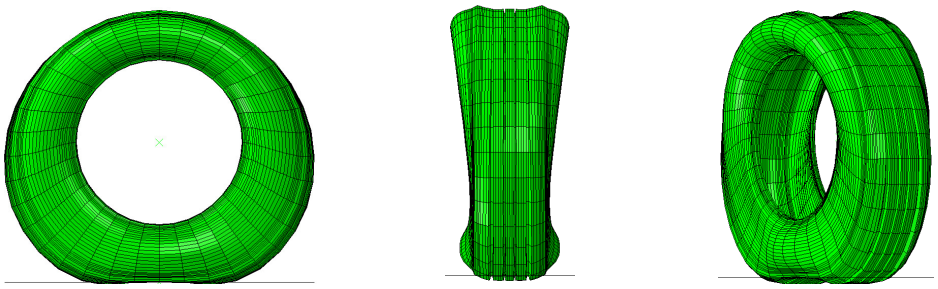

Figure 8-6: 5th vibrational mode of the truck tire in a side-view (left), front-view (middle), and 3D view (right).

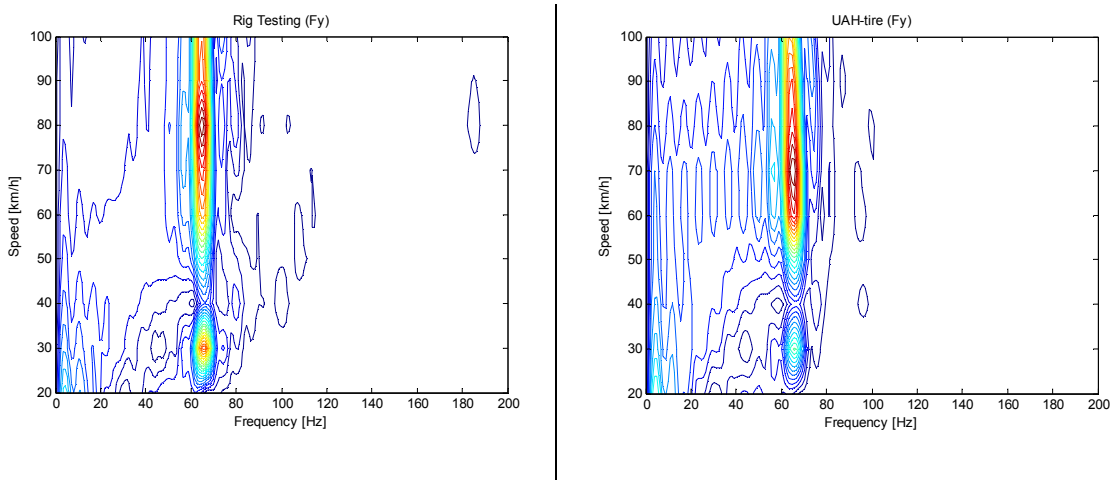

Figure 8-7: Vertical (F_y) reaction forces at the spindle for various speeds in frequency domain as a contour plot.

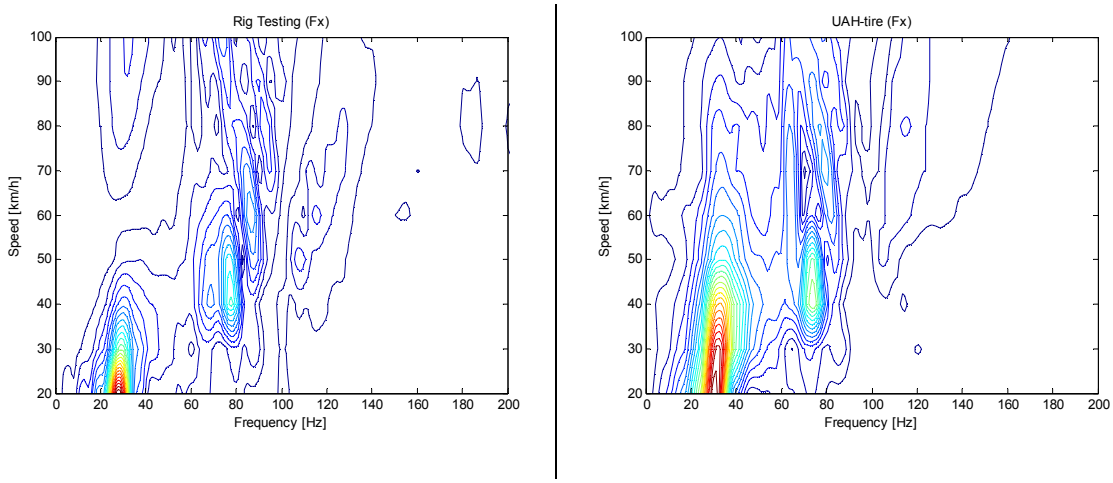

Figure 8-8: Horizontal (F_x) reaction forces at the spindle for various speeds in frequency domain as a contour plot.

8.4 Simulation sensitivity

The accuracy of the tire simulation depends on two factors: numerical integration properties, and modeling approximations. Numerical integration is influenced by the type of integrator such as one-step (Runge-Kutta) and multi-step methods (Adams), and integration tolerances such as relative and absolute tolerance. On the other hand modeling approximation defines how well a numerical model can represent a physical

system. In this section focus is paid on the approximation of the *UAH-tire* model. While the *UAH-tire* model provides reasonable simulation results overall, as shown in Section 8.3, some divergence between the simulation results and the rig testing results can be observed. The author believes that these divergences are mainly due to three approximations in the *UAH-tire* model, which are discussed in this section. The three approximations are damping and stiffness matrix, patch discretization, and friction model.

8.4.1 Influence of damping and stiffness

Rubber is a viscoelastic material; i.e., it exhibits viscous and elastic characteristics if it undergoes deformation. In viscoelastic materials the relationship between stress and strain is time dependent. In the case of a tire, the viscosity contributes to rolling resistance and the decay of the tire's vibration. This characteristic can be included in *UAH-tire* through a damping matrix. However, modeling of a proper damping matrix **C** is complex and still not fully understood. While the effects of damping are clear, the characterization of damping is a challenge. A correct representation of damping is important if a model is used to predict a transient response correctly. One of the simplest methods to synthesize a damping matrix is the Rayleigh damping, which is used for the cleat test simulation. Here, the damping matrix is assumed to be proportional to the mass and stiffness matrices as $\mathbf{C} = a_0\mathbf{M} + a_1\mathbf{K}$, where a_0 and a_1 can be set in such a way that two modal damping ratios are satisfied. However, this method causes the other damping ratios to vary with natural frequencies. This is not consistent with experimental data that indicate that the damping ratios are roughly the same for several vibration modes of the

tire. Clearly, this has an effect on the cleat test simulation and, hence, more work needs to be dedicated to this matter. Figure 8-9 shows the effect of damping on the results of the cleat test at 60 km/h.

The viscoelastic characteristic of the rubber also has an effect on the tire's stiffness. The stiffness of a physical tire is higher in an oscillatory loading condition than in a static loading condition. The *UAH-tire* is a linear model where the stiffness remains constant during any dynamic motion. Choosing the right stiffness matrix for a particular scenario is therefore crucial. For that reason the stiffness contribution from viscoelasticity is taken into account for the above mentioned cleat test.

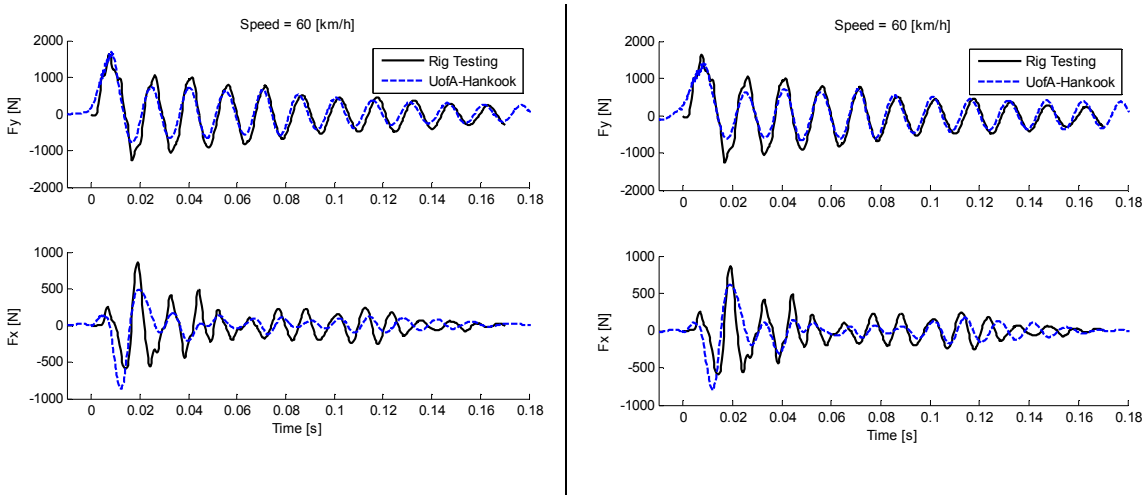

Figure 8-9: a_0 and a_1 are adjusted to provide a damping ratio for the 5th and 12th mode around: 3% (left); and 1% (right).

8.4.2 Influence of patch discretization

The discretization of the patch is another important factor. The FE model is constructed through several cross-sections. The discretization on the patch depends on the distance between some of these cross-sections as well as on the number of contact nodes that are selected on each cross-section. A finer mesh detects a cleat much better,

which again influences the results of the test. However, with each additional contact node the total DoF of the system increases by three, which further slows down the computation performance. The results of the UAH-tire can be improved by approximating the physical tire with a non-uniform finite element tire model that has smaller distances between the cross-sections at the patch area than the finite element model used for the cleat test.

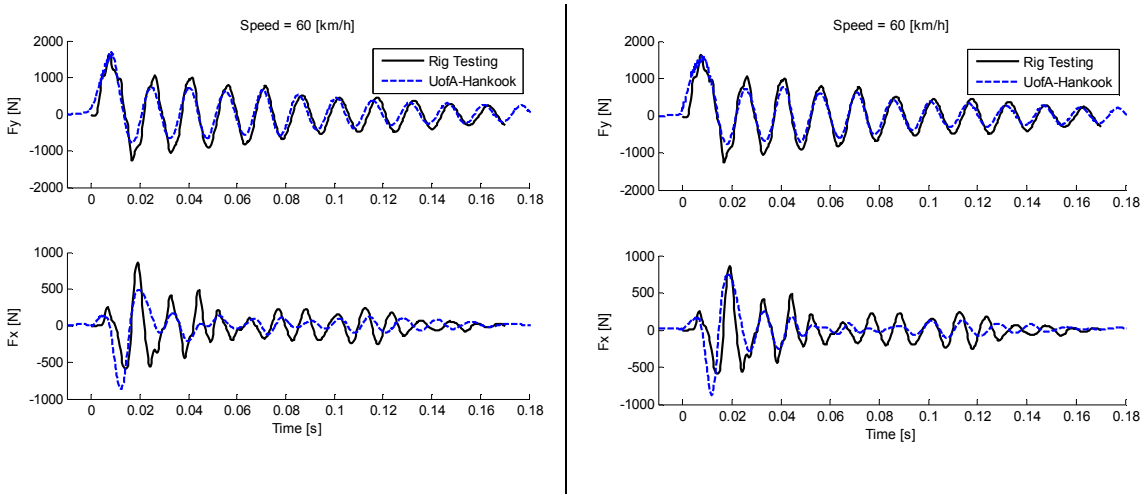

Figure 8-10: *UAH-tire* with: 50 modes and 95 contact nodes (left); 50 modes and 252 contact nodes (right).

8.4.3 Influence of friction model

The friction model has an impact on the cleat test results as well, especially in the reaction forces at the spindle in longitudinal direction, as shown in Figure 8-11. Friction in the tire is mainly described by the static, μ_s, and kinetic, μ_k, friction coefficients of rubber on asphalt. However, these coefficients are not constant and they change with temperature, tread wear, inflation pressure, loading, etc. Also small deformations that occur in the tread elements during rolling and cornering have a significant influence on

the friction property of a tire. Defining a proper friction model is therefore crucial and not an easy task.

The current *UAH-tire* model uses a simple Coulomb friction model for each contact node. If a contact node starts to slip over the ground, it will experience a resisting force opposite to its direction of motion. A Coulomb friction model is simple and easy to implement in a tire model. However, it has the disadvantage that it creates friction only if a contact node slides over the ground. A Coulomb friction model cannot represent static friction (stick). Due to the lack of representing sticking, some vibration frequencies of the tire model are lower than they are supposed to be, especially in torsional direction around the axis of rotation. Improving or replacing the current friction model in *UAH-tire* will improve the simulation results of the tire model significantly, especially in the longitudinal direction.

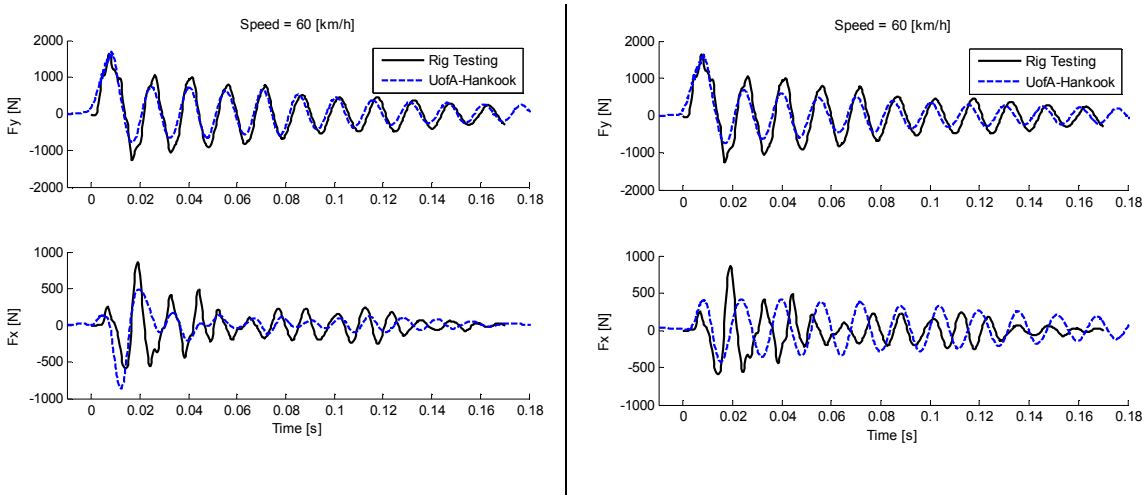

Figure 8-11: Cleat test with slip friction model ($\mu_s = \mu_k = 0.85$; left) and pure slip ($\mu_s = \mu_k = 0$; right).

8.5 Cleat test simulation on flat surface

A cleat test is usually performed on a drum rather than on a flat road, due to test rig costs. The data obtained from the drum cleat test is used to predict a tire's noise, vibration, and harshness in an 'on road' scenario. However, it can be shown that vibrations in a rolling tire differ on a drum or on a flat surface, which is due to different pressure distributions on the patch as well as the patch size. To indicate the difference, a *UAH-tire* with a high fidelity patch is pressed on a drum (radius = 1.25 m) and on a flat smooth surface. The pressure distributions on both surfaces are shown in Figure 8-12. In both cases the tire's loading pressure is 1000 lb (4448 N).

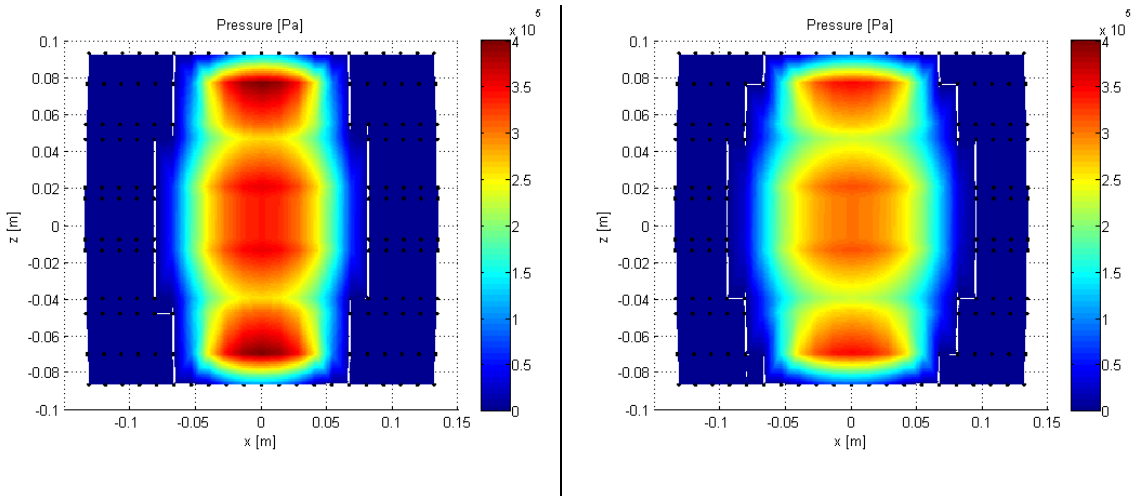

Figure 8-12: Pressure distribution on a drum (left) and on a flat smooth surface (right). Black points represent contact nodes. Not all contact nodes are in contact with the drum/ground.

The previous cleat test simulation is performed on a drum, which provides data that closely matches the rig testing results. In this section, the same cleat test is repeated on a flat surface, where the tire is rolled over the ground, as shown in Figure 8-13. All other initial conditions, such as loading, speed, size of the cleat, etc., are kept the same as in the drum scenario. For readability, the results are given in frequency-domain in Figure

8- as a contour plot only. A comparison between the contour plots shows clearly a shift in the vibration amplitudes. While in the drum cleat test a significant vibrational drop can be observed in the speed range of 40-50 km/h, in the cleat test on a flat surface this vibrational drop shifted to a speed range of 45-55 km/h. This change in the tire's vibrational behavior should not come with a surprise, since the boundary conditions (patch size and pressure distribution) for the tire have changed. This comparison concludes that a cleat test on a drum might not be sufficient in a design phase of a new tire, since it does not reveal the true vibration of a tire in an on road scenario.

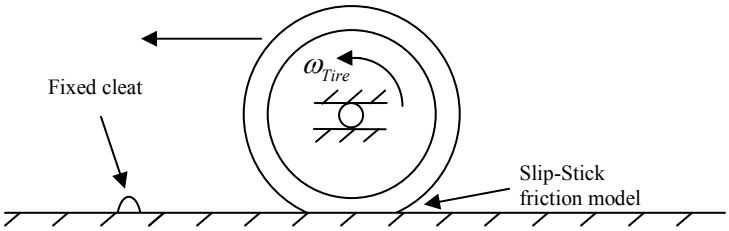

Figure 8-13: Simulation setup of the cleat test on flat surface.

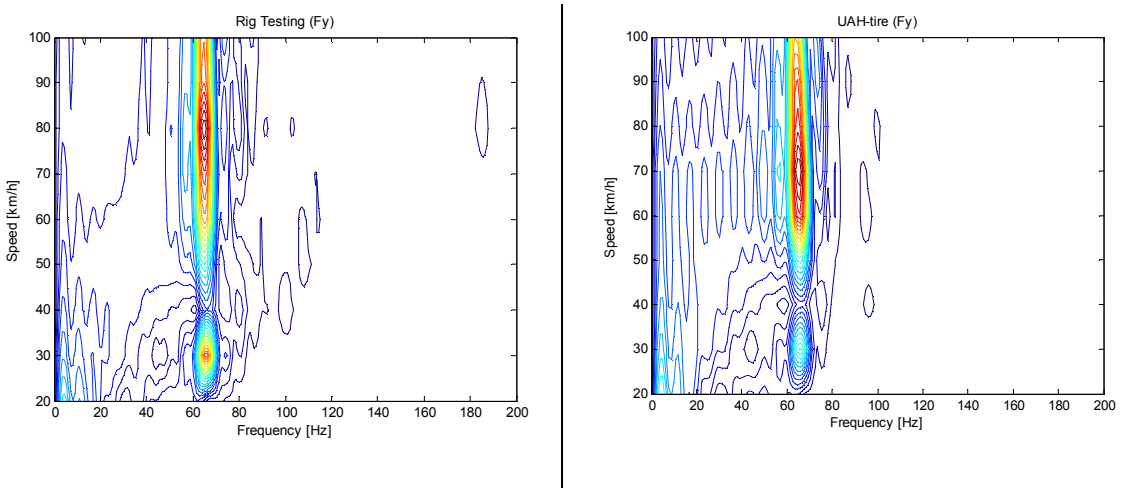

Figure 8-14: Vertical (Fy) reaction forces as a contour plot. Rig testing (upper left), simulation on a drum (upper right), and simulation on a flat smooth surface.

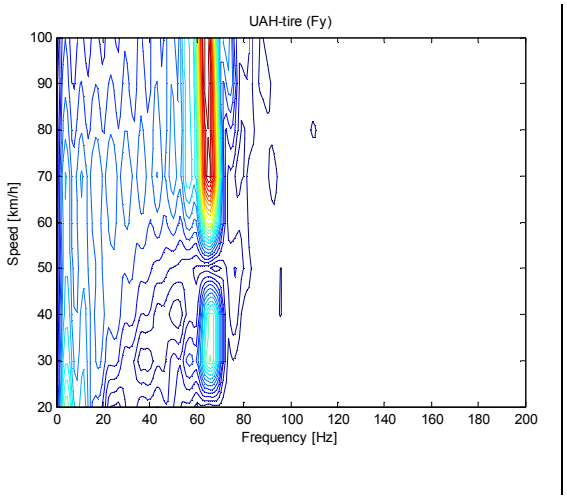

Figure 8-14 (cont.): Vertical (F_y) reaction forces as a contour plot. Rig testing (upper left), simulation on a drum (upper right), and simulation on a flat smooth surface.

8.6 Discussion

This chapter provided a cleat test simulation that is conducted with the new tire model called *UAH-tire*. The results of the cleat test were compared to experimental data that is provided by "Hankook Tire" [72]. The results were compared in the time- and frequency-domains. While few deviations between the simulation and the test rig data exist, the overall results from the UAH-tire are promising. In addition to the analysis of the results, a discussion is given that identifies factors that can influence the simulation results significantly, if they are not handled properly. In this context the author believes that the friction model is shown to have the most important influence on the simulation accuracy. An inaccurate friction model between the tire and the ground influences the most the reaction forces at the spindle in the longitudinal direction. It can be concluded that if the current friction model in *UAH*-tire is replaced by a more advanced friction model, then an overall improvement in the *UAH-tire* performance should be expected.

9. SUMMARY, CONCLUSION, AND FUTURE WORK

In the early stages of multibody system (MBS) analysis, bodies were considered as rigid (non-deformable). However, soon after the introduction of multibody dynamics (MBD) into the broader engineering community, engineers realized that the rigid-body assumption was not sufficient for every application. This led to the demand for including flexible bodies in a MBS. Nowadays, most deformable bodies are included in MBS as finite element (FE) models. The FE technique was initially used in structural analysis only, but was extended later to satisfy the needs of MBS simulations. Unfortunately, high-resolution FE models require long computational time in MBS simulations due to their large number of degrees-of-freedom (DoF). While some deformable bodies can be described by few finite elements, most deformable bodies contain many elements that lead to hundreds or thousands of DoF. Due to the large number of DoF of these bodies the computational time for a MBS simulation become impractical. Therefore, FE models need to be truncated in the number of DoF by some kind of reduction technique before they are included into a MBS.

The use of modal data in representing a deformable body is well understood in the multibody community. By truncating modes associated with higher frequencies, the dynamic eigen-properties of the body can be preserved. Also, the finite element model may be in contact with other rigid or deformable bodies, the reduction technique needs to address the issue of moving boundary conditions. Any of the reduction techniques from the family of component mode synthesis methods, that originated from sub-structuring, address the issue of moving boundary conditions and eigen-property preservation. They

perform well over a broad range of MBS applications, as long as the contact (boundary) nodes remain contact nodes throughout the entire period of simulation. However, this may not be the case for all MBS applications. In this dissertation, two examples are provided where the premise of non-changing contact nodes is not preserved: a belt that rotates about two pulleys; and a tire that rolls over the ground. In both applications, as soon as the system starts rotating, the initially declared contact nodes leave the contact area and some other nodes that were initially free become new contact nodes. The existing methodologies in multibody modeling of a deformable body with modal data, prior to the research presented in this dissertation, have not addressed the issue of changing contact nodes.

This dissertation is dedicated to MBS applications that include deformable bodies based on truncated modal data and changing contact nodes. This research demonstrates that the FE model of some deformable bodies with changing contact nodes also contain a certain orientation invariant characteristic. This characteristic is present in the rolling tire and the rotating belt drive examples. When a tire rolls over the ground, the mass and stiffness distributions do not change with respect to the rotating axis. The same counts for a power transmission belt. From the perspective of an outside observer, it becomes irrelevant how much the belt moves along the pulley, because the mass and stiffness distribution of the belt never changes. This orientation invariance allows the mass and stiffness for these bodies to be considered independent from the DoF about the corresponding rotational axis. The research documented in this dissertation shows how the orientation invariant characteristic can be used to develop a new methodology that

addresses the issue of changing contact nodes and modal data. The developed concept is referred to as the *flowing material*, where it defines the orientation invariant DoF of the reduced FE model in Eulerian space, while the remaining DoF are defined in Lagrangian space. The combination of Eulerian and Lagrangian formulation, within the framework of component mode synthesis, is a new concept in deformable MBD.

While the dissertation presents the concept of *flowing material* only on three different examples (string, belt drive, and tire), many other examples can be found that could take advantage of this new concept. The reason for focusing on these three examples is due to their different degree-of-complexity. The traveling string is the simplest example with the smallest number of DoF. It serves mostly as an introduction to the new concept, but has no significant value to the engineering community. On the other hand, the power transmission belt/chain is a more complex system that is of more interest to an engineer. Applying the concept of *flowing material* to the power transmission belt allows the modes of the free vibrating part of the belt to be truncated in order to improve computational efficiency. Furthermore, due to the concept of *flowing material*, the mesh of the belt becomes stationary that avoids the introduction of an artificial periodic excitation in the response. The most evident use of the new concept can be seen on a rolling FE tire model. Since, full FE tire models include thousands of DoF, a MBD analysis with these models is not feasible. With the use of the *flowing material* concept these models can be truncated significantly. The research presented in this dissertation shows that a strongly truncated FE tire model that incorporates the new concept can still accurately represent complex simulations such as a cleat test.

Although the concept of *flowing material* is a great accomplishment in handling deformable bodies with modal data and changing contact nodes, it should be emphasized that this concept is based on the idea that the vibration mode shapes of the deformable body remain constant; i.e., the underlying FE model must be linear. Here, linear refers to constant stiffness and mass matrices. Geometric and material non-linearities cannot be captured with a linear FE model. Non-linearities play a significant role if, for example, a body undergoes large deformations or experiences excessive heat. In the case of a tire, these non-linearities can occur if a tire rolls with a high velocity and sudden braking, which causes the patch of the tire to deform strongly and to create excessive heat due to sliding friction. The heat and the deformation will change the eigen-properties of the tire, which may only be captured with a non-linear FE model. Many other interesting examples can be found that require non-linearities. For that reason a future work should extend the concept of *flowing material* for deformable bodies that are described by non-linear FE models. The combination of changing mode shapes with the idea of *flowing material* will be a challenging and interesting task.

The initial purpose of the concept of *flowing material* has been to resolve the problem of changing contact nodes for deformable body models using modal data. However, it turns out that this concept can also provide researchers and engineers a new perspective on the dependencies between the body's natural frequencies and its traveling speed. For example, the numerical and analytical solution of the string model shows that the string vibrates slower with increasing travel speed; i.e., the natural frequencies of the string are shifting to lower values when the traveling speed increases. The same drop in

the natural frequencies can also be observed in a power transmission belt. Since this shift of natural frequencies is intrinsic in the equations of motion of the string and can also be observed in the rotating belt, we could contemplate that any deformable body with an orientation invariant characteristic would exhibit this phenomenon. This means that a rolling tire should experience a shift in its natural frequencies as well. In a matter of fact, cleat tests show that pneumatic tires experience a change in their eigen-properties with increasing rolling speed, even though this change is insignificant for normal driving speeds. However, the relationship between the eigen-frequencies and the rolling speed of a tire is not yet fully understood.

Another phenomenon that engineers have observed in a pneumatic tire is the occurrence of a standing wave. In this phenomenon the rolling resistance increases significantly near a velocity called the critical rolling velocity. Near and above that critical speed, a wave develops in that portion of the tire that has just left contact with the road. From a still standing observer, looking at the rolling tire, this wave seems to be stationary, which gives the phenomenon the name "standing-wave". Standing-wave is a major cause for a drastic increase in rolling resistance and tire temperature. Because the large strains associated with the standing-waves inevitably lead to significant working of the tire material, rolling at or above the critical speed for a long period of time can lead to tire failure. Therefore, the critical speed represents a serious performance limitation for high-speed tires. The author believes that this phenomenon is caused by a severe shift in the natural frequencies of the tire, which is similar to the shift that occurs in the string and belt drive models. Once a natural frequency of the tire drops to zero Hertz, its

corresponding mode shape will magnify in amplitude and stop vibrating, hence, forming a “standing-wave”.

The occurrence of a shift in the natural frequency can analytically be proven in the simple string model. Here, the phenomenon of standing-wave exists as well. The respective critical speed that causes the standing wave formation in the string can easily be calculated. However, determining the critical speed in a tire is not that simple. As a future work, the relationship between standing-waves and the shift in the natural frequencies should be investigated in more detail, especially with a focus on tires. This work would be of high relevance to the tire and automobile industry and should give the industry a new insight in tire behavior and safety issues. Many improvements in tires can be gained through this research.

APPENDIX A. MODE SHAPE DERIVATIVES

The concept of *flowing material* allows a FE mesh to be independent of a specific rotational DoF; e.g., in a FE tire model, the mesh can translate with the rolling tire, but does not need to roll with it. This independency (stationary character) can be achieved by introducing mode shape derivatives into the equations of motion of the FE model, as shown for example in Eq.(4.20). For very simple examples, such as the string, these derivatives can be obtained analytically. However, for more complex systems, such as the power transmission belt and the rolling tire, the derivatives can be obtained only numerically. This appendix will introduce three numerical methods that can be used to calculate the required mode shape derivatives:

- Finite Differences Method
- Collocation Method using polynomials
- Fast Fourier Transformation

All three numerical methods are already well known for approximating the solutions to differential equations. However, they have not been used in the context of mode shape derivatives until now.

A.1 Discrete mode shapes

In a vibrating flexible body, a normal mode shape is a pattern of motion where any part of the body move sinusoidally with the same frequency and in phase. The frequencies of the normal mode shapes are referred to as natural frequencies. A body

with a finite, but continuous volume has infinite many mode shapes. However, if the body is approximated by a discrete model, such as a FE model, then the number of mode shapes is finite. The mode shapes of a undamped FE model are obtained by solving the generalized eigenvalue problem $\mathbf{K\Psi} = \mathbf{M\Psi\Lambda}$, where **M** and **K** are mass and stiffness matrix of the free vibrating model. If the body is constrained at some of its nodes, then the respective DoF need to be eliminated in **M** and **K**. If the FE model has *n* degrees-of-freedom in total, then $\mathbf{\Psi} = [\boldsymbol{\varphi}_1 \quad \boldsymbol{\varphi}_2 \quad \cdot \quad \boldsymbol{\varphi}_n]$ contains *n* eigen-modes when all modes are kept. Each eigen-mode $\boldsymbol{\varphi}_i = \left[\varphi_i^1 \quad \varphi_i^2 \quad \cdot \quad \varphi_i^n\right]^T$ is an array of length *n* again.

A.2 Mode shape derivatives using finite differences

One way, and maybe the easiest one, to obtain spatial derivatives of the mode shapes is by using the method of finite differences. The implementation will be shown on the simple string model, as shown in Chapter 4-5. In this model each node has only one DoF (vertical deflection) and the derivative should be taken with respect to the horizontal elongation *x*. The distances between the nodes should be denoted by h_j and h_{j+1}, as shown in Figure A-1. The derivative of mode *i* can be obtained by calculating the central difference at each node:

$$\left(\varphi_i^j\right)_{,x} = \frac{\left(\varphi_i^{j+1} - \varphi_i^{j-1}\right)}{\left(h_{i+1} + h_i\right)} \tag{A.1}$$

Note, in order to calculate the derivatives at the first or the last node, other finite difference methods need to be considered. Fortunately, in some applications, such as the

string model, the deflections at the boundaries are equal to zero, which allows us to use central differences at the first and last node as well

$$\left(\varphi_i^1\right)_{,x} = \frac{\left(\varphi_i^2 - 0\right)}{\left(h_{i+1} + h_i\right)}, \quad \left(\varphi_i^n\right)_{,x} = \frac{\left(0 - \varphi_i^{n-1}\right)}{\left(h_{i+1} + h_i\right)} \tag{A.2}$$

The array of the first mode shape derivative is written as

$$\left(\boldsymbol{\varphi}_i\right)_{,x} = \left[\left(\varphi_i^1\right)_{,x} \quad \left(\varphi_i^2\right)_{,x} \quad \cdot \quad \left(\varphi_i^n\right)_{,x}\right]^T \tag{A.3}$$

and the complete set of first mode shape derivatives can be denoted by

$$\boldsymbol{\Psi}_{,x} = \left[\left(\boldsymbol{\varphi}_2\right)_{,x} \quad \left(\boldsymbol{\varphi}_2\right)_{,x} \quad \cdot \quad \left(\boldsymbol{\varphi}_n\right)_{,x}\right] \tag{A.4}$$

The second mode shape derivatives $\boldsymbol{\Psi}_{,xx}$ can be obtained by applying the finite difference method on $\boldsymbol{\Psi}_{,x}$.

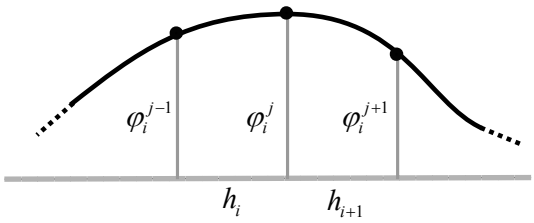

Figure A-1: Section of the string model for central difference approximation.

A.3 Mode shape derivatives using polynomials

Any mode shape can be approximated by a polynomial of a certain degree *m*. In the collocation method, a *m*-dimensional space of candidate solutions and *n* number of points in the domain (called collocation points) can be chosen, such that one solution can be found that overlaps the polynomial with the mode shape at the collocation points. Here, the collocation method will be shown using the Vandermonde matrix.

The columns of a Vandermonde matrix $\mathbf{V} = \mathbf{V}(\mathbf{x})$ are powers of the array $\mathbf{x} = [x_1 \quad x_2 \quad \cdot \quad x_n]^T$, that is,

$$\mathbf{V} = \begin{bmatrix} 1 & x_1 & (x_1)^2 & \cdot & (x_1)^m \\ 1 & x_2 & (x_2)^2 & \cdot & (x_2)^m \\ \cdot & \cdot & \cdot & \cdot & \cdot \\ 1 & x_n & (x_n)^2 & \cdot & (x_n)^m \end{bmatrix} \tag{A.5}$$

Each column of **V** represent a polynomial of degree one (simple polynomial). A linear combination of these simple polynomials can represent any polynomial of degree *m*. The array **x** includes the collocation points of the domain. In the case of the string model, the domain is the horizontal elongation of the string and the collocation points coincide with the string's grid points. The Vandermonde matrix contains *n* collocation points and *m* polynomials. The number of polynomials can be equal or less than the number of collocation points.

Once the Vandermonde matrix is created, the following relationship can be established

$$\mathbf{V}\mathbf{p}_i = \boldsymbol{\varphi}_i \tag{A.6}$$

where $\mathbf{p}_i$ is a column-array with the factors of the simple polynomials, and $\boldsymbol{\varphi}_i$ is the *i*'s eigen-mode. For all eigen-modes, Eq. (A.6) can be extended to

$$\mathbf{V}\mathbf{P} = \boldsymbol{\Psi} \tag{A.7}$$

such that $\mathbf{P} = [\mathbf{p}_1, \mathbf{p}_2, \ldots, \mathbf{p}_n]$. If *m*=*n*, than the factors can be calculated simply by

$$\mathbf{P} = \mathbf{V}^{-1}\boldsymbol{\Psi} \tag{A.8}$$

In some cases it is preferred to approximate the mode shapes with fewer simple polynomials in order to avoid high oscillations at the boundaries. Therefore, if $m<n$, than the factors can be calculated by solving a least square problem:

$$\mathbf{P} = \left(\mathbf{V}^T\mathbf{V}\right)^{-1}\mathbf{V}^T\mathbf{\Psi} \tag{A.9}$$

If a polynomial of order m represents a mode shape, then the derivative of this polynomial describes the spatial derivative of the mode shape. Once the factors of the polynomials are calculated, the spatial derivatives of the mode shapes can be obtained easily. But first, the first and second derivative of the Vandermonde matrix $\mathbf{V}$ with respect to the spatial derivative x need to be calculated:

$$\mathbf{V}_{,x} = \begin{bmatrix} 0 & 1 & 2x_1 & \cdot & m(x_1)^{m-1} \\ 0 & 1 & 2x_2 & \cdot & m(x_2)^{m-1} \\ \cdot & \cdot & \cdot & \cdot & \cdot \\ 0 & 1 & 2x_n & \cdot & m(x_n)^{m-1} \end{bmatrix}, \quad \mathbf{V}_{,xx} = \begin{bmatrix} 0 & 0 & 2 & \cdot & m(m-1)(x_1)^{m-2} \\ 0 & 0 & 2 & \cdot & m(m-1)(x_2)^{m-2} \\ \cdot & \cdot & \cdot & \cdot & \cdot \\ 0 & 0 & 2 & \cdot & m(m-1)(x_n)^{m-2} \end{bmatrix} \tag{A.10}$$

Then, the first and second derivative of the mode shapes can be simply obtained by

$$\mathbf{\Psi}_{,x} = \mathbf{V}_{,x}\mathbf{P}, \quad \mathbf{\Psi}_{,xx} = \mathbf{V}_{,xx}\mathbf{P} \tag{A.11}$$

The advantage of using polynomials to represent mode shapes lies in the simple calculation of the Vandermonde matrix and its derivatives. However, past experiences show that polynomials tend to oscillate significantly at the end of the domain. These can be corrected by shifting the collocation points further towards the boundaries of the domain. Unfortunately, in the case of mode shapes, the collocation points are already determined in advance by the FE grid; i.e., collocation points have to coincide with grid nodes.

In this section, the following simple polynomials were used: $f(x)=1$, $f(x)=x$, $f(x)=x^2$. There is no doubt that different sets of simple polynomials can provide different accurate results for different domains. It should be left to the experience of the engineer, which simple polynomials should be used in a specific application.

A.4 Mode Shape derivatives using fast Fourier transformation

Another idea that can be used for determining the derivatives is the fast Fourier transformation. A Fourier transformation transforms a function into frequency domain. The original function usually depends on time, and therefore is called the time domain representation of the function, whereas the Fourier transform depends on frequency and is called therefore the frequency domain representation of the function. However, the original function does not need to depend necessarily on time in order to be transformed into frequency domain; it can also depend on spatial variables, such as the Euclidian coordinates. The function is called to be the spatial domain representation. A transformation from spatial domain into frequency domain is subjected to the same laws and conditions as the transformation from the time domain to frequency domain, except that the meaning of the obtained frequencies differs. However, the meaning of the frequencies should be of no importance to the reader at this point.

The discrete Fourier transformation (DFT) is the discrete analogous to Fourier transformation. It requires an input function that is discrete and has a limited number of values. Such inputs are often obtained by sampling a continuous function. Here, our mode shape φ is such a discrete function. The reader is referred to [79] for the derivation

of DFT. A fast Fourier transform (FFT) on the other hand defines a set of efficient algorithms to compute the discrete Fourier transform (DFT) and its inverse. There are many distinct FFT algorithms which increases the computational efficiency of DFT significantly. However, it is not necessary at this point to understand their concept, it should just be noted that if DFT is used in a code to obtain the derivatives of the mode shapes, it is usually implemented as a FFT.

The mode shapes in the frequency domain can be written as

$$\boldsymbol{\Psi}^{+} = FFT(\boldsymbol{\Psi}) \tag{A.12}$$

where $FFT(\boldsymbol{\Psi})$ indicates a FFT of the mode shapes. This is valid for mode shapes whose boundaries are equal to zero, such as fixed normal mode shapes. Then, the first and second derivative of the mode shapes in the frequency domain is

$$\begin{aligned} \boldsymbol{\Psi}^{+}_{,x} &= \frac{-2\pi \mathrm{i}}{n}\mathbf{E}.\boldsymbol{\Psi}^{+} \\ \boldsymbol{\Psi}^{+}_{,xx} &= \left(\frac{-2\pi \mathrm{i}}{n}\right)^{2}\mathbf{R}.\boldsymbol{\Psi}^{+} \end{aligned} \tag{A.13}$$

where i represents the complex number, and

$$\mathbf{E} = \begin{bmatrix} 0 & 0 & . & 0 \\ 1 & 1 & . & 1 \\ . & . & . & . \\ n-1 & n-1 & . & n-1 \end{bmatrix}, \quad \mathbf{R} = \begin{bmatrix} 0^2 & 0^2 & . & 0^2 \\ 1^2 & 1^2 & . & 1^2 \\ . & . & . & . \\ (n-1)^2 & (n-1)^2 & . & (n-1)^2 \end{bmatrix} \tag{A.14}$$

are of size $n \, x \, m$. The dot in Eq. (A.13) and (A.14) indicates an element wise product between matrices. Then the first and second spatial derivative of the mode shapes in the spatial domain is

$$\begin{aligned} \Psi_{,x} &= real(IFFT(\Psi^{+}_{,x})) \\ \Psi_{,xx} &= real(IFFT(\Psi^{+}_{,xx})) \end{aligned} \tag{A.15}$$

where *IFFT()* is the inverse fast Fourier transform and *real()* indicates that only the real part of the matrix elements are considered.

Equation (A.12) to (A.15) show that with the Fourier transformation mode shape derivatives can be obtained quickly, since sophisticated FFT algorithms are already available to the broader public. However, a Fourier transformation of mode shapes that belong to a high-resolution FE model can lead to long computation time and high computer memory requirements.

A.5 Discussion

This chapter shows how to obtain the mode shape derivatives in three different ways: Finite differences method; Collocation Method using polynomials; and fast Fourier transformation. The efficiency and accuracy of each method depends on the model/application. Each method is represented on a simple one dimensional string model. However, they can be extended to two or three dimensional problems as well. In higher dimensions the mode shapes need to be split in its separate coordinates first, e.g. *x-y-z,* before the derivatives can be applied. Furthermore, in each application the elongation for the flowing material needs to be determined, such as x for the string, s for the belt, and ϕ for the tire. This elongation defines the basic domain for the mode shape derivatives. The mode shapes need to be derived in respect to this elongation. Finally, even though only three methods are introduced here, many other methods can be found in the

literature that can help to calculate mode shape derivatives. It is up to the engineer to determine which method is adequate for the application at hand.

APPENDIX B. LAGRANGIAN VS EULERIAN FORMULATION

There are two types of formulation that are commonly used in finite element theory. These are the Lagrangian and Eulerian description, also referred to as the material and spatial description, respectively. If the reader is already familiar with FEM, then he must have used either one, or both, formulation already. The Lagrangian formulation is mainly used in solid mechanics, where the position and physical properties of the particles in a body are described in terms of the material or referential coordinates and time. On the other hand, the Eulerian formulation mainly finds its applications in fluid dynamics, where motion is described by fixed spatial coordinates. In the following sections, both formulations will be introduced and their use in FEM described. The representation of the two formulations follows closely the one given by [80]. The reader is encouraged to read [80] for in detail explanations and examples of the Lagrangian and Eulerian description.

B.1 Configurations and deformation mapping

Consider a body B in three-dimensional Euclidean space, whose geometry and composition is known. If body B is exposed to loadings, then it will undergo deformations. If the applied loads are time dependent, then the geometry of body B will change continuously, whereby the deformation of the body is a function of time. The

body will go through a continuous sequence of geometrical regions. A region occupied by the deformed body at time *t* is called configuration and denoted by *K*.

At the initial configuration K_0, the particle X occupies the position $\mathbf{X} = (X_1, X_2, X_3)$. Here, X is the name of a particle on body *B*, **X** is the location of the particle X at the configuration K_0, and (X_1, X_2, X_3) are the material coordinates. After applying a load, body *B* changes its geometric shape and goes into a new configuration *K*, which is called the current or deformed configuration. At this configuration, X occupies the position $\mathbf{x} = (x_1, x_2, x_3)$. The mapping $\chi : B_{K_0} \rightarrow B_K$ is called the deformation mapping of body *B* from the configuration K_0 to *K*.

For both descriptions, Lagrangian and Eulerian, the same frame of reference is chosen that will describe the deformations. This frame is also used for all configurations. The components X_i and x_i of the vectors **X** and **x** are along the axis of this reference frame.

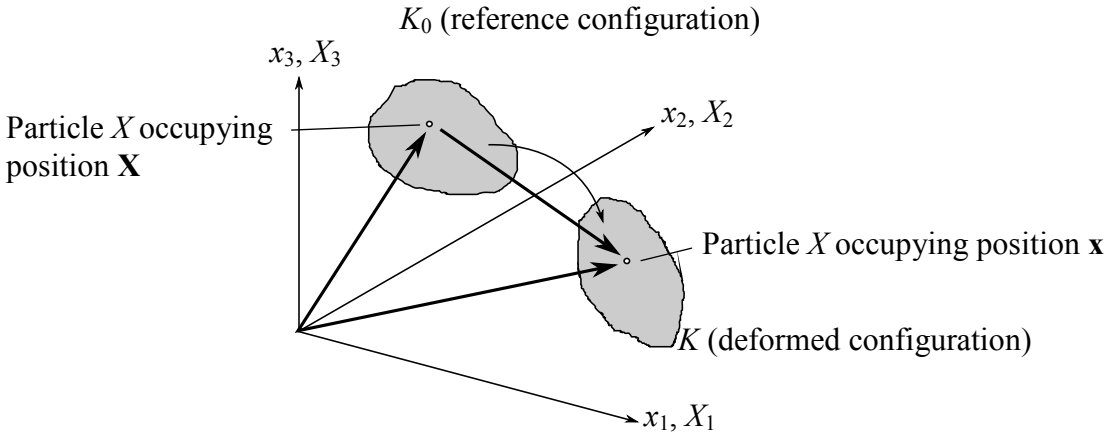

Figure B-2: Reference and deformed configuration of a body.

B.2 Lagrangian description

In the Lagrangian description, the deformations of body B are referred to a reference configuration, which is often chosen to be the undeformed configuration K_0. From this results that the current coordinates are expressed in terms of the reference coordinates

$$\mathbf{x} = \chi(\mathbf{X}, t), \quad \mathbf{X} = \chi(\mathbf{X}, 0) \tag{B.1}$$

Equation (B.1) implies that the particle X occupies the position $\mathbf{X}$ at initial time (t = 0), but as time changes the same particle moves to the current position $\mathbf{x}$, as shown in Figure B-2. In another words, the attention is focused on the material particle X. Hence, a body property ϕ is described with respect to the material coordinates $\mathbf{X}$ and time t:

$$\phi = \phi(\mathbf{X}, t) \tag{B.2}$$

Equation (B.2) gives the value ϕ at time t associated with the particle X. The material derivative of this value is simply the partial derivative with respect to time, since the material coordinate $\mathbf{X}$ does not change with time:

$$\frac{d}{dt}[\phi(\mathbf{X}, t)] = \frac{\partial}{\partial t}[\phi(\mathbf{X}, t)]\Big|_{\mathbf{X} \text{ fixed}} = \frac{\partial \phi}{\partial t} \tag{B.3}$$

B.3 Eulerian description

In the Eulerian description the deformation of body B is referred to the current configuration K, and ϕ is described with respect to the current position $\mathbf{x}$ in space:

$$\phi = \phi(\mathbf{x}, t), \quad \mathbf{X} = \mathbf{X}(\mathbf{x}, t) \tag{B.4}$$

Here, attention is given to what is occurring at a fixed point in space as time progresses, instead of giving attention to an individual particle, as shown in Figure B-3. In other words, at time t a particle X occupies the position $\mathbf{x}$. However, as time progresses particle X moves away and a new particle occupies the same position $\mathbf{x}$. Now attention will be paid to ϕ of the new particle. The material derivative of the value ϕ is given by

$$\frac{d}{dt}[\phi(\mathbf{x},t)] = \frac{\partial}{\partial t}\left[\phi(\mathbf{x},t)\right] + \frac{dx_i}{dt}\frac{\partial}{\partial x_i}\left[\phi(\mathbf{x},t)\right] = \frac{\partial \phi}{\partial t} + v_i \frac{\partial \phi}{\partial x_i} = \frac{\partial \phi}{\partial t} + \mathbf{v}\cdot\nabla\phi \qquad \text{(B.5)}$$

where $\mathbf{v}$ is the velocity, $\mathbf{v} = d\mathbf{x}/dt = \dot{\mathbf{x}}$.

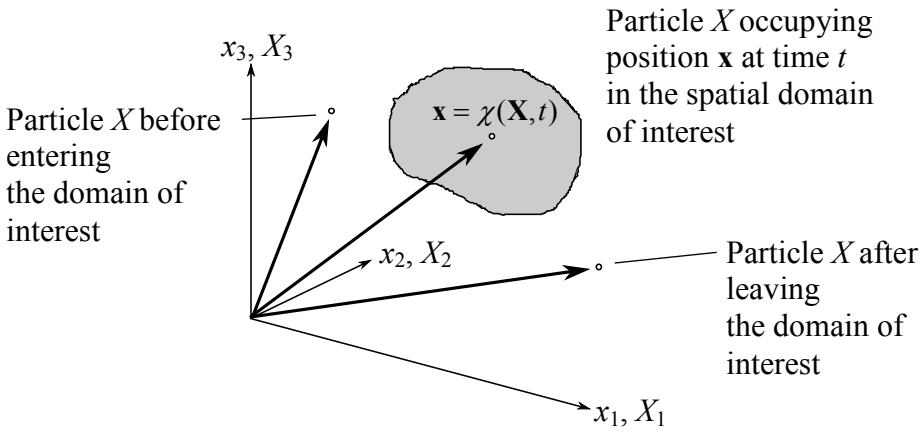

Figure B-3: Material points within and outside the spatial domain of interest in spatial description.

B.4 Lagrangian and Eulerian description in FEM

Both descriptions, Lagrangian and Eulerian, are used in the finite element method. Which formulation is preferred depends on the nature of the problem. If a solid mechanic problem is at hand, then the deformation and inner stresses of a body for a specific loading is usually of interest. For this set of problems the Lagrangian description is preferred. Here, the finite element mesh moves with the material particles. In other words, the same material particle is continuously at the same mesh point.

If, on the other hand, a fluid mechanic problem needs to be analyzed, then it is more of an interest how the properties of the fluid, such as pressure, heat, or velocity, changes at a specific point in space. Furthermore, considering the kinematics of the fluid, a fluid particle can undergo very large motions. In this case it is effective to use an Eulerian description. Using this formulation, the mesh covers the whole domain of interest and is stationary. The material particles move through the finite element mesh in whichever way the flow conditions govern such movements.

If a problem includes free surfaces and/or interactions between fluid flows and structures, than a more recent developed third formulation for the FEM is practical. It is often referred to the arbitrary-Lagrangian-Eulerian (ALE) description and it is a mixture of the two formulation mentioned above. Here, the mesh points move, but not necessarily with the material particles. Moreover, the mesh movement corresponds to the nature of the problem and is imposed by the solution algorithm itself. While ALE is similar in the idea to the concept *flowing material*, its derivation is completely different.

REFERENCES

[1] Shabana, A. A., "Flexible Multibody Dynamics: Review of Past and Recent Developments," Multibody System Dynamics, 1, pp. 189–222, 1997.

[2] Shabana, A.A., Dynamics of Multibody Systems, Wiley, New York, 1989.

[3] Nikravesh, P.E. and Lin, Y., 'Body reference frames in deformable multibody systems', International Journal of Multiscale Computational Engineering 1(2/3), 2003, 201–217.

[4] Guyan, R.J., "Reduction of Stiffness and Mass Matrices", AIAA Journal, VOL. 3, NO. 2, p. 380, 1965.

[5] Hurty, W. C., "Vibrations of Structural Systems by Component-Mode Synthesis," Journal of the Engineering Mechanics Division, ASCE, VOL. 86, EM (NO.) 5, pp. 51-69, 1960.

[6] Hurty, W. C., "Dynamic Analysis of Structural Systems Using Component Modes," AIAA Journal, VOL. 2, NO.4, pp. 678-685, 1965.

[7] Craig, R. Jr., Bampton, M. C., "Coupling of Substructures for Dynamic Analysis," AIAA Journal, VOL. 6, NO. 7, pp.1313-1319, 1968.

[8] Friberg, O., "A Method for Selecting Deformation Modes in Flexible Multibody Dynamics," International Journal for Numerical Methods in Engineering, VOL. 32, pp.1637-1655, 1991.

[9] http://basicmechanics.blogspot.com/2010_06_01_archive.html

[10] Bathe, K.J., Ekkehard, R., Wilson, E.L., "Finite Element Formulations for Large Deformation Dynamic Analysis", International Journal for Numerical Methods in Engineering, VOL. 9, pp.353-386, 1975

[11] Szabo, I., "Geschichte der mechanischen Prinzipien", Birkhaeuser, Basel, 1977

[12] Schiehlen, W., Eberhard, P., "Technische Dynamik: Modelle fuer Regelung und Simulation", Edition 2, Teubner, Wiesbaden, 2004

[13] Nikravesh, P.E., "Computer-Aided Analysis of Mechanical Systems", Prentice-Hall, Englewood Cliffs, New Jersey, 1988

[14] García de Jalón, J., Bayo, E., "Kinematic and Dynamic Simulation of Multibody Systems: The Real-Time Challenge", Springer-Verlag, New York, 1994

[15] García de Jalón, J., Serna, M.A., Avilés, R., "A Computer Method for Kinematic Analysis of Lower-Pair Mechanisms. Part I: Velocities and Accelerations and Part II: Position Problems", Mechanism and Machine Theory, Vol. 16, pp.543-566, 1981

[16] Serna, M.A., Avilés, R., García de Jalón, J., "Dynamic Analysis of Plane Mechanisms with Lower-Pairs in Basic Coordinates", Mechanism and Machine Theory, Vol. 17, pp.397-403, 1982

[17] García de Jalón, J., Unda, J., Avello, A., "Natural Coordinates for the Computer Analysis of Multibody Systems", Computer Methods in Applied Mechanics and Engineering, Vol.56, pp.309-327, 1986

[18] Shabana, A.A., "Finite element incremental approach and exact rigid body inertia", ASME Journal of Mechanical Design, VOL.118, Issue 2, pp.171–178, 1996

[19] Shabana, A.A., "An absolute nodal coordinate formulation for the large rotation and deformation analysis of flexible bodies", Technical Report No. MBS96-1-UIC, Department of Mechanical Engineering, University of Illinois at Chicago, 1996

[20] Hurty, W. C., Collins, J. D., Hart, G. C., "Dynamic Analysis of Large Structures by Model Synthesis Techniques," Computers & Structures, VOL. 1, pp. 535-563, 1971.

[21] Wickert, J.A., 'Non-linear vibration of a traveling tensioned beam', Int. J. Non-Linear Mechanics, Vol. 27, No. 3, pp. 503-517, 1992

[22] Pellicano, F., Vestroni, F., 'Nonlinear dynamics and bifurcations of an axially moving beam', Journal of Vibration and Acoustics, Vol. 122, No. 1, pp.21-22, 2000

[23] Koivurova, H., Salonen, E.-M., 'Comments on non-linear formulations for travelling string and beam problems', Journal of Sound and Vibration, Vol. 255, No. 5, pp.845-856, 1999

[24] Bradley, J., and Allen, R.F., "The behavior of rubber-tyred wheels", The Automotive Engineer, VOL.21, NO. 2777, 1931

[25] Gim, G., and Nikravesh, P.E., 'An Analytical Model of Pneumatic Tires for Vehicle Dynamic Simulation, (Part 1: Pure Slips; Part 2: Comprehensive Slips; Part 3: Validation)" *Int. J. for Vehicle Design*, (Vol. 11, No. 6, pp. 589-618; Vol. 12, No. 1, pp. 19-39; Vol. 12, No. 1, pp. 217-228) 1991.

[26] Dugoff, H., and Segel, L., 'An Analysis of Tire Traction Properties and Their Influence on Vehicle Dynamic Performance,' *SAE document 700377*, 1970.

[27] Bakker, E., and Pacejka, H.B., 'The Magic Formula for Tire Model,' *Vehicle System Dynamics*, Vol. 21, 1993.

[28] Eichler, M., 'A Ride Comfort Tyre for Vibrational Analysis in Full Vehicle Simulation,' *Proc. 2nd International Colloquium on Tyre Models for Vehicle Dynamic Analysis*, pp. 109-122, 1997.

[29] Bruni, S., Cheli, F. and Resta, F., 'On The Identificationin Time Domain of The Parameters of A Tyre Model for The Study of In-plane Dynamics,' *Proc. 2nd International Colloquium on Tyre Models for Vehicle Dynamic Analysis*, pp. 136-150, 1997.

[30] Allison, D.J. and Sharp, R.S., 'On The Low Frequency In-plane Forced Vibrations of Pneumatic Tyre/Wheel/Suspension Assemblies,' *Proc. 2nd International Colloquium on Tyre Models for Vehicle Dynamic Analysis*, pp. 151-162, 1997.

[31] Pacejka, H.B., *Tyre and Vehicle Dynamics; 2nd ed.*, Oxford: Butterworth-Heinemann, 2006.

[32] Gipser, M., 'FTire, A New Fast Tire Model for Ride Comfort Simulations,' *International ADAMS User Conference*, Berlin, 1999.

[33] Oertel, Ch., and Fandre, A., 'Ride Comfort Simulations and Steps Towards Life Time Calculations: RMOD-K and ADAMS,' International ADAMS User Conference, Berlin, 1999.

[34] Padovan, J., 'Numerical Simulation of Rolling Tires, Tire Rolling Losses and Fuel Economy,' An R&D Planning Workshop, October 19, 20, Series SAE conference proceeding, P-74, pp.103-109, 1977.

[35] Becker, A., Seifert, B., 'Simulation of Wear With A FE Tyre Model Using A Steady State Rolling Formulation,' Aliabadi M, SamartinA (eds) *Computational methods in contact mechanics III*, vol Computational Mechanics Publication, Boston, pp 119–128, 1997.

[36] Faria, L.O., Oden, J.T., Yavari, B., Tworzydlo, W.W., Bass, J.M., Becker, E.B., 'Tire Modeling by Finite Elements,' *Tire Sci Technol* 20 (1), p.33–56, 1992.

[37] Nackenhorst, U., 'On The Finite Element Analysis of Steady State Rolling Contact,' Aliabadi M, Brebbia, C. (eds) *Contact mechanics–computational techniques*, vol Computational Mechanics Publication, Boston, pp. 53–60, 1993.

[38] Kao, B.G., Muthukrishnan, M., 'Tire Transient Analysis With An Explicit Finite Element Program,' *Tire Science and Technology*, Vol. 25, No. 4, pp. 230-244, 1997.

[39] Brinkmeier, M., Nackenhorst, U., Volk, H., 'A Finite Element Approach to The Transient Dynamics of Rolling Tires With Emphasis on Rolling Noise Simulation,' *Tire Science and Technology*, Vol. 35, pp. 165-182, 2007.

[40] Nikravesh, P.E., "Model Reduction Techniques in Flexible Multibody Dynamics", W. Schiehlen and M. Valasek (eds.), Virtual Nonlinear Multibody Systems, Kluwer Academic Publishers, pp. 83-102, 2003.

[41] Hurty, W.C., "Dynamic Analysis of Structural Systems Using Component Modes", AIAA Journal, VOL. 2, NO. 4, pp. 678-685, 1965.

[42] Nikravesh, P.E. and Lin, Y.S., "Comparison of Reduction Methods for Deformable Multibody Dynamics", Proceedings of the ASME 2005 International Design Engineering Technical Conference, IDETC/CIE, Paper DETC2005-84820, Long Beach, California, 2005.

[43] www.emerson-ept.com/eptroot/public/schools/beltchan.pdf.

[44] Fawcett, J. N., 'Chain and Belt Drives – A Review', Shock and Vibration Digest, VOL. 13, NO. 5, pp. 5-12, 1981.

[45] Mahalingam, S., 'Polygonal Action in chain drives', Journal of the Franklin Institute, Vol. 265, No. 1, pp.23-28, 1958

[46] Abrate, A. S., 'Vibration of belts and belt drives', Mechanism and Machine Theory, VOL. 27, NO. 6, pp. 645–659, 1992.

[47] Wickert, J. A., 'Non-linear vibration of a traveling tensioned beam', Int. J. Non-Linear Mechanics, VOL. 27, NO. 3, pp. 503-517, 1992.

[48] Pellicano, F., Vestroni, F., 'Nonlinear dynamics and bifurcations of an axially moving beam', Journal of Vibration and Acoustics, VOL. 122, pp.21-30

[49] Moon, J., Wickert, J. A., 'Non-linear vibration of power transmission belts', Journal of Sounds and Vibration, VOL. 200, NO. 4, pp. 419-431, 1997.

[50] Pellicano, F., Fregolent, A., Bertuzzi, A., Vestroni, F., 'Primary and parametric non-linear resonances of a power transmission belt: Experimental and theoretical analysis', Journal of Sounds and Vibration, VOL. 244, NO. 4, pp. 669-684, 2001.

[51] Leamy, M. J., Wasfy, T. M., 'Transient and steady-state dynamic finite element modeling of belt-drives', Journal of Dynamic Systems, Measurement and Control, VOL. 124, pp. 575–581, 2002

[52] Kerkkanen, K. S., Garcia-Vallejo, D., Mikkola, A.M., 'Modeling of belt-drives using a large deformation finite element formulation', Nonlinear Dynamics, VOL. 43, pp. 239–256, 2006.

[53] Wang, K. W., Liu, S. P., 'On the noise and vibration of chain drive systems', The Shock and Vibration Digest, VOL. 23, NO. 4, pp. 8–13, 1991

[54] Turnbull, S., Fawcett, J., 'Dynamic behavior of roller chain drives', Mechanisms 1972, pp. 29–35, 1972

[55] Chew, M., 'Inertia effects of a roller-chain on impact intensity', Journal of Mechanisms, Transmissions, and Automation in Design, VOL. 107, pp. 123–130, 1985

[56] Veikos, N. and Freudenstein, F., 'On the dynamic analysis of roller chain drivers: Part i - theory', Mechanical Design and Synthesis, ASME, DE-VOL. 46, pp. 431–439, 1992

[57] Fritz, P. and Pfeiffer, F., 'Dynamics of high-speed roller-chain drives', Design Engineering Technical Conferences 3-Part A, pp. 573–584, 1995

[58] Troedson, I. and Vedmar, L., 'A dynamic analysis of the oscillations in a chain drive method to determine the static load distribution in a chain drive', Transactions of the ASME 121, pp. 402–408, 1999

[59] Troedson, I. and Vedmar, L., 'A dynamic analysis of the oscillations in a chain drive', Journal of Mechanical Design 123, pp. 395–401, 2001

[60] Pedersen, S. L., "Simulation and Analysis of Roller Chain Drive Systems," Ph.D. Dissertation, Department of Mechanical Engineering, Solid Mechanics, Technical University of Denmark, Lyngby, Denmark, 2004.

[61] Čepon, G., Manin, L., and Boltežar, M., "Validation of a Flexible Multibody Belt-Drive Model", Strojniški vestnik – Journal of Mechanical Engineering, VOL. 57, pp. 539-546, 2011.

[62] Čepon, G., Manin, L., Boltežar, M., "Introduction of damping into the flexible multibody belt-drive model: A numerical and experimental investigation", Journal of Sound and Vibration, VOL. 324, pp. 283-296, 2009.

[63] Čepon, G., Manin, L., Boltežar, M., "Experimental identification of the contact parameters between a V-ribbed belt and pulley", Mechanism and Machine Theory, VOL. 45, pp. 1424-1433, 2010.

[64] Gerbert, G., "Belt slip – a unified approach", Journal of Mechanical Design, VOL. 118, pp. 432-438, 1996.

[65] Reynolds, O., "Creep Theory of Belt Drive Mechanics", The Engineer, VOL. 38, NO. 396, 1847.

[66] Swift, H. W., "Power Transmission by Belts: An Investigation of Fundamentals", Proceedings of the Institute of Mechanical Engineers, VOL. 2, NO. 659, 1928.

[67] Firbank, T.C., “Mechanics of the Belt Drive”, International Journal of Mechanical Science, VOL. 12, NO. 12, 1970.

[68] Leamy, M.J., Wasfy, T.M., "Analysis of Belt-Drive Mechanics Using a Creep-Rate Dependent Friction Law", Journal of Applied Mechanics, VOL. 69, Issue 6, pp. 763-771, 2002

[69] Timoshenko, S., “Theory of elastic stability”, McGraw-Hill Book Company, New York, 1st Ed. 1936, 2nd Ed. 1961 (J. M. Gere, J.M.)

[70] Bechtel, S.E., Vohra, S., Jacob, K. I., Carlson, C. D., “The stretching and slipping of belts and fibers on pulleys,” Journal of Applied mechanics, Vol.67, pp.197-206, 2000.

[71] “MTS Systems Corporation” is a provider for industry testing and sensing solutions: http://www.mts.com/ucm/groups/public/documents/library/dev_002230.pdf

[72] “Hankook Tire Co., Ltd.” is a provider of radial tires for passenger cars, SUVs, light trucks, campers, trucks, buses and for automobile motorsport: http://www.hankooktireusa.com

[73] Copyright ©1994 - 2012 Christopher J. Longhurst. All Rights Reserved. http://www.carbibles.com

[74] Lin, Y.S., Nikravesh, P.E., “Deformable Body Model Reduction with Mean-Axes,” Mechanics Based Design of Structures and Machines, Vol. 34, No. 4, pp. 469-488, 2006.

[75] Nikravesh, P.E., Lin, Y.S., “Use of Principle Axes as the Floating Reference Frame for a Deformable Body,” Multibody System Dynamics, Vol. 13, No. 2, pp. 211-231, 2005.

[76] Agrawal, O.P., Shabana, A.A., “Application of Deformable-Body Mean Axis to Flexible Multibody System Dynamics,” Computer methods in Applied Mechanics and Engineering, Vol. 56, pp. 217-245, 1986.

[77] Nikravesh, P.E., “Planar Multibody Dynamics: Formulation, Programming, and Applications,” Taylor & Francis CRC Press, 2007.

[78] Bathe, K.J., “Finite Element Procedures”, Prentice-Hall, 1996.

[79] Ginsberg, J.H., “Mechanical and Structural Vibrations: Theory and Applications,” John Wiley & Sons, 2001.

[80] Reddy, J.N., “An introduction to continuum mechanics: with applications,” Cambridge University Press, 2008

[81] Nikravesh, P.E., Ribaric, A.P., Kazemi, O., "Challenges in Multibody Dynamic Analysis of Vehicles", 5th Asian Conference on Multibody Dynamics, Keynote Lecture, Japan, 2010.

[82] Lin, Y.S., "Model Reduction For a Restrained Deformable Body," Dissertation (PhD) – University of Arizona, Tucson, Arizona, 2005.